

ENHANCING THE RELIABILITY OF FUNCTIONAL MRI AND
MAGNETOENCEPHALOGRAPHY FOR PRESURGICAL
MAPPING

by

M. Tynan R. Stevens

Submitted in partial fulfillment of the
requirements for the degree of
Doctor of Philosophy

at

Dalhousie University
Halifax, Nova Scotia
July 2015

© Copyright by M. Tynan R. Stevens, 2015

Table of Contents

List of Tables	vi
List of Figures	vii
Abstract	ix
List of Abbreviations and Symbols Used	x
Acknowledgements	xii
Chapter 1 Introduction	1
1.1 Surgical Treatment of Brain Tumors	2
1.2 Pre-Surgical Mapping	3
1.3 Single-Subject Imaging	5
1.4 Research Objectives	7
Chapter 2 Theory	8
2.1 Functional MRI	8
2.1.1 Signal Generation	8
2.1.2 Image Formation	12
2.2 Magnetoencephalography	14
2.2.1 Signal Generation	14
2.2.2 Image Formation	16
2.3 Statistical Images and Thresholding	20
2.4 The ROC-r Framework	22
2.4.1 Motivation and Background	22
2.4.2 ROC-r Algorithm	23
2.4.3 Simulation	26
2.4.4 Repeatability, Reliability, and Accuracy	28
2.4.5 Summary	28
Chapter 3 Manuscript 1: Thresholds in fMRI Studies: Reliable for Single Subjects?	30
3.1 Motivation	30

3.2	Abstract	31
3.3	Introduction	31
3.3.1	Background	31
3.3.2	Classification Reliability	33
3.3.3	Research Objectives	35
3.4	Methods	35
3.4.1	Participants	35
3.4.2	MRI Acquisition Details	35
3.4.3	Functional Task	36
3.4.4	Functional MRI Analysis	36
3.4.5	Reliability Calculations	37
3.4.6	Threshold Optimization	39
3.5	Results	41
3.5.1	Group Analysis	41
3.5.2	Group Average Threshold-Reliability Dependence	41
3.5.3	Individual Variability	43
3.5.4	Analysis of Poor Datasets	52
3.6	Discussion	54
3.6.1	Group-level Reliability	54
3.6.2	Single-subject Reliability	54
3.6.3	Threshold Optimization	55
3.7	Conclusion	57
Chapter 4	Manuscript 2: Fully Automated Quality Assurance and Localization of Volumetric MEG for Potential use in Pre-Surgical Mapping	59
4.1	Motivation	59
4.2	Abstract	61
4.3	Introduction	61
4.4	Methods	63
4.4.1	Data Collection	63
4.4.2	MNS Paradigm	63
4.4.3	Data Pre-processing	64
4.4.4	Source Localization	64
4.4.5	Anatomical Template	65
4.4.6	Quality Assurance Analysis	65
4.4.7	ROC-r Thresholding	66

4.4.8	Localization Comparison	67
4.5	Results	67
4.5.1	Sensory Evoked Fields	67
4.5.2	Beamformer Reliability and Quality Assurance	67
4.5.3	Source Localization and Thresholding	71
4.6	Discussion	71
4.6.1	The MNS SEF	73
4.6.2	ROC-reliability for Quality Assurance	75
4.6.3	ROC-r Thresholding to Localize MEG Sources	76
4.6.4	Data Quality Influences Co-localization Accuracy	77
4.7	Conclusion	77
Chapter 5	Manuscript 3: Improving fMRI Reliability in Pre-surgical Mapping for Brain Tumors	78
5.1	Motivation	78
5.2	Abstract	80
5.3	Introduction	81
5.3.1	Pre-surgical Mapping Validity and Reliability	81
5.3.2	Thresholds for Pre-surgical Mapping	82
5.3.3	The ROC-reliability (ROC-r) Framework	83
5.4	Methods	83
5.4.1	Participants	83
5.4.2	MRI Acquisition Details	85
5.4.3	Functional MRI Analysis	85
5.4.4	ROC-reliability Analysis	87
5.4.5	Cortical Stimulation	88
5.4.6	Spatial Correspondence Measurements	88
5.5	Results	89
5.5.1	Reliability	89
5.5.2	Pipeline Optimization	89
5.5.3	Spatial Correspondence with CS	90
5.5.4	Automatic Thresholding	91
5.6	Discussion	95
5.6.1	Reliability of Pre-surgical fMRI	95
5.6.2	ROC-r Pre-processing Optimization	95
5.6.3	Clinical Utility of ROC-reliability Analysis	96
5.7	Conclusion	98

Chapter 6	Manuscript 4: A Unified Framework to Optimize fMRI and MEG Processing for Push-button Pre-surgical Mapping	99
6.1	Motivation	99
6.2	Abstract	100
6.3	Introduction	101
6.4	Methods	103
6.4.1	Processing Pipeline Optimization	103
6.4.2	Subjects	104
6.4.3	Stimulation Paradigm	105
6.4.4	MRI Acquisition	105
6.4.5	MRI Processing	105
6.4.6	MEG Recording	106
6.4.7	MEG Processing	106
6.4.8	Intraoperative Mapping	107
6.5	Results	108
6.5.1	Pre-processing Optimization	108
6.5.2	Automated Thresholding	110
6.5.3	Patient Case	110
6.6	Discussion	114
6.7	Conclusion	117
Chapter 7	Conclusions	118
7.1	Summary	118
7.2	Future Work	120
7.3	Conclusion	122
References		123

List of Tables

4.1	Correlation Between Goodness-of-fit and ROC-r Reliable Fraction	70
5.1	Patient characteristics	84
5.2	Functional Task Battery	86
5.3	ROC Contingency Table	89
5.4	Optimized Pre-processing Pipeline Frequencies	92

List of Figures

1.1	Functional MRI	4
1.2	Magnetoencephalography	4
2.1	MR Relaxation	9
2.2	Field Offsets Around a Blood Vessel	11
2.3	General Linear Model	13
2.4	MEG Evoked Response	14
2.5	MEG Signal	15
2.6	MEG Forward Solution	17
2.7	ROC Curve Calculation	23
2.8	ROC-r AUC Plot	25
2.9	Dependence of ROC-r Method on SNR and Activation Extent	27
3.1	Test-retest Overlap Schematic	38
3.2	ROC-r Calculation Schematic	40
3.3	Group fMRI Maps of Finger Tapping	41
3.4	Group Mean Test-retest Overlap	42
3.5	Variability of Single-subject ROC-r	43
3.6	Variability of Single-subject Overlap	45
3.7	Optimized Thresholding for Highly Reliable Data	47
3.8	Optimized Thresholding for Moderately Reliable Data	48
3.9	Optimized Thresholding for Unreliable Data: 1	49
3.10	Optimized Thresholding for Unreliable Data: 2	50
3.11	Group-level Overlap of Reliability Optimized Thresholded Maps	51
3.12	Subject-specific Pre-processing for Enhanced Reliability	53
4.1	ROC-r Output Schematic	66

4.2	Sensory Evoked Field Butterfly Plots and Sensor Topographies	68
4.3	MEG Dipole Goodness-of-fit Compared to ROC-reliability . . .	69
4.4	Example Co-localization of Dipole and Thresholded Beamformer	72
4.5	Co-localization Accuracy Histogram	73
4.6	Dependence of Co-localization Accuracy on Quality Metrics .	74
5.1	Patient vs. Controls Reliability Histograms	90
5.2	Patient Reliability With/Without Pipeline Optimization . . .	91
5.3	CS to fMRI Distance vs. Threshold	92
5.4	Co-localization of ROC-r Thresholded fMRI Maps and CS Results	93
5.5	Sensitivity and Specificity of ROC-r Localization	94
6.1	ROC-r Schematic	104
6.2	fMRI Reliability by Pipeline	109
6.3	MEG Reliability by Pipeline	111
6.4	Example ROC-r Localization for fMRI and MEG	112
6.5	ROC-r Group Overlap for fMRI and MEG	113
6.6	Patient Example of ROC-r Optimization for fMRI and MEG .	114

Abstract

Pre-surgical mapping has become a crucial tool in the preparation and planning for brain tumor resection since the development of widely available non-invasive imaging technologies like functional magnetic resonance imaging (fMRI) and magnetoencephalography (MEG). Strategies for dealing with single-subject analysis are key to overcome issues surrounding individual variability and inter-rater reliability. In this thesis, a receiver operating characteristic reliability (ROC-r) framework for evaluating and optimizing the reliability of pre-surgical mapping is developed and implemented in a variety of applications. ROC-r allows for fully automated, yet individualized processing of single-subject data, directly addressing both the issues of individual variability and inter-rater reliability for fMRI and MEG.

A series of four manuscripts form the foundation of this thesis. The first, “*Thresholds in fMRI studies: Reliable for single subjects?*”, shows the impact of individual variability on the reliability of fMRI activation maps, and demonstrates the use of ROC-r for evaluating reliability and selecting activation thresholds. The second paper, “*Fully automated quality assurance and localization of volumetric MEG for pre-surgical mapping*”, establishes the use of ROC-r for quality assurance and automated localization in MEG. The third study, “*Improving fMRI reliability in pre-surgical mapping for brain tumors*”, shows the primary clinical application of ROC-r in pre-surgical mapping. This paper demonstrates that although patient data are less reliable than controls, this can be compensated for by optimization of pre-processing pipelines. Furthermore, this manuscript compared the fMRI results to cortical stimulation mapping, showing that more reliable datasets were better at identifying critical eloquent brain regions. In the fourth and final manuscript, “*A unified framework to optimize fMRI and MEG processing for push-button pre-surgical mapping*”, we explicitly evaluate ROC-r as a unified framework for push-button individualized analysis of fMRI and MEG data.

Overall, this thesis demonstrates that ROC-r enhances the reliability of pre-surgical mapping by both fMRI and MEG, by providing quantitative measures for selecting reliable pre-processing pipelines, and determining data-driven thresholds for localizing reliable activation foci. The ROC-r method improves pre-surgical mapping capabilities by introducing clinically relevant quality assurance parameters and facilitating push-button production of reliable activation maps.

List of Abbreviations and Symbols Used

ACC	autocorrelation correction
AFNI	analysis of functional neuroimages
AUC	area under the curve
α	flip angle
BEM	boundary element method
BOLD	blood oxygen level dependent
CBF	cerebral blood flow
CBV	cerebral blood volume
CMRO ₂	cerebral metabolic rate of oxygen consumption
CS	cortical stimulation
ECD	equivalent current dipole
EOG	electro-oculargraphy
F_R	Reliable Fraction
fMRI	functional magnetic resonance imaging
FDR	false discovery rate
FN	false negatives
FOV	field of view
FP	false positives
FPR	false positive rate
FWHM	full width half maximum
GLM	general linear model
GoF	goodness-of-fit
GRF	gaussian random field
HRF	hemodynamic response function
ICA	independent component analysis
ICC	intraclass correlation
MEG	magnetoencephalography
MNI	montreal neurological institute
MNS	median nerve stimulation

MPR	motion parameter regression
MP-FLASH	magnetization prepared fast low angle shot
MRI	magnetic resonance imaging
NPAIRS	nonparametric prediction, activation, influence, and reproducibility resampling
R_J	Jaccard overlap
R_R	Rombouts overlap
ROC	receiver operator characteristic
ROC-r	receiver operator characteristic reliability
ROI	region of interest
SEF	sensory evoked fields
SNR	signal-to-noise ratio
SSS	signal space separation
TE	echo time
TI	inversion time
TN	true negatives
TP	true positives
TPR	true positive rate
TR	repetition time
tSSS	temporal signal space separation
WHO	world health organization

Acknowledgements

There are many people who I would like to thank for helping to make this work possible. My mentors Ryan D'Arcy, Steven Beyea, Gerhard Stroink, and David Clarke for giving me the opportunity to work in this fantastic field, and helping me complete the various works described in this thesis. Also a special thanks to Tim Bardouille, who provided invaluable feedback on my MEG manuscripts.

I want to acknowledge the support offered by my peers throughout my tenure at Dalhousie. Especially to Steve Patterson for many insightful conversations, and a memorable trip through Tasmania. To Eva Gunde for always lending a willing ear, and encouraging me to 'focus!'. Also to Josh Bray, Erin Mazerolle, Kim Brewer, and Jodie Gawryluk. These individuals were my early role models as graduate students, and their influence has not gone unappreciated.

There have been a host of supportive staff both at the lab and within the hospital that have been vital to conducting these research projects. Perhaps chief among them is Ron Hill, who provided endless assistance in working with the clinical facilities. Maggie Clarke for conducting my MEG scans, and both Dave McAllindon and Careesa Liu for running my fMRI experiments.

And last, but certainly not least to my family and friends for supporting me through all the hard work. Of course none more so than my loving wife Alice, for the many pots of tea, the early morning breakfasts, and shoveling snow when I was too busy writing. You have kept me focussed on my goals, and always weighed in when I was wrestling with words.

Chapter 1

Introduction

This thesis examines the challenges of pre-surgical functional mapping by functional MRI (fMRI) and magnetoencephalography (MEG), and in particular addresses the difficulties associated with single-subject analyses. Pre-surgical mapping is increasingly used to obtain patient-specific information on the location of critical functional zones, in order to provide insights into the risk/benefit tradeoffs of surgical intervention. The production of robust activation maps and the reduction of subjectivity in data processing are vital in order to consistently provide the best possible pre-surgical information. Three significant challenges in implementing a pre-surgical mapping program are:

- Identifying data quality issues
- Selecting data processing pipelines
- Setting activation thresholds

This thesis demonstrates a novel method of receiver operating characteristic reliability (ROC-r) analysis for robust and automated pre-surgical mapping for brain tumor surgery. The use of ROC-r addresses each of these three challenges by generating quantitative quality assurance parameters, optimizing the pre-processing steps used to produce functional maps, and providing data-driven thresholding of the resulting images. In order to understand the context of the capabilities of ROC-r, a brief introduction to pre-surgical mapping will be given, and motivation for the need for an automated yet individualized approach to image production will be presented. This will be followed in chapter 2 by a discussion of some of the key theoretical underpinnings of fMRI and MEG mapping, along with a detailed description of the ROC-r algorithm. Chapter 3 will demonstrate the application of ROC-r analysis to fMRI data, and a comparison to other overlap-based analyses. Chapter 4 outlines the application of ROC-r for MEG processing, with a comparison to equivalent current dipole

localization for validation. In chapter 5, a patient cohort is examined to demonstrate how reliability improvements translate into improved pre-surgical localization. Finally, chapter 6 explicitly shows that ROC-r can be used to optimize pre-processing pipelines and automatically select activation thresholds using a unified approach for fMRI and MEG.

1.1 Surgical Treatment of Brain Tumors

Surgical resection is one of the primary treatment options for brain tumors, along with radiation therapy and chemotherapy. Resection provides immediate benefits in terms of symptom control, especially in rapidly growing tumors, by reducing intracranial pressure through debulking [1, 2]. Surgical treatment also provides the opportunity for tumor biopsy, providing vital histological information. Additionally, tumors often contain hypoxic cells with inadequate vascular supply, which respond poorly to radiation and chemotherapy, and removal of bulk tumor can therefore increase the efficacy of other treatment options. Most importantly, complete surgical resection correlates with increased survival times compared to partial resection or biopsy alone [1–5].

Excision of brain tumors becomes more challenging when located in or next to eloquent cortex (i.e. critical functional zones), which may be the case for more than half of all tumors [6]. Surgeons must therefore balance the desire to achieve gross total resection with the need to respect critical cortical structures and avoid post-operative morbidity. The primary tool at a surgeon’s disposal in these cases is direct electrical stimulation of the cortex (i.e. cortical stimulation or CS). Popularized by Wilder Penfield and colleagues in the mid 20th century [7–9], cortical stimulation can be used to produce involuntary motor responses, elicit somatic sensations, or temporarily disrupt language functions. The intraoperative mapping of brain functions afforded by CS increases the ability to achieve gross total resection with minimal post-operative deficits [10, 11].

While cortical stimulation remains the gold standard for individualized functional mapping [3], there are several obvious drawbacks to this technique. Firstly, CS is unavailable until the time of surgery, rendering it unsuitable for pre-operative planning or post-operative assessment. CS is also clearly unethical for research studies in

healthy controls, restricting our knowledge of its effects in humans to diseased populations. Even in patients, CS requires highly cooperative individuals, may extend operating room times, and comes with a risk of inducing seizures [12]. Furthermore, it has recently been argued that the effects of CS are more complex than generally acknowledged, including current spread, potentially distant remote effects, and complex behavioural responses [13]. Moreover, large areas of the cerebrum can not be mapped by cortical stimulation, which is not typically able to map sites deep to the cortex, or areas not exposed by the craniotomy. Nonetheless, CS mapping is indispensable for avoiding post-operative morbidity in the context of significant individual variability of functional anatomy, especially in the presence of potential reorganization in response to pathology [11, 13, 14].

1.2 Pre-Surgical Mapping

In the last few decades, potential non-invasive alternatives to CS have arisen in the form of functional magnetic resonance imaging (fMRI) and magnetoencephalography (MEG). Functional MRI was first demonstrated by Ogawa *et al.* (Figure 1.1) [15], and has generated an incredible level of interest both from the neuroscience and clinical communities, due to its ability to generate high resolution images of brain function [16]. Modern MEG scanners, with large arrays of sensors that provide whole-brain coverage and millisecond temporal resolution, appeared around the same time as the first fMRI experiments (Figure 1.2) [17]. Other functional mapping techniques like electroencephalography (EEG) or positron emission tomography (PET) are also available, but are outside the scope of this thesis.

The advent of non-invasive functional imaging has revolutionized the practice of pre-surgical mapping. While both MEG and fMRI have been demonstrated extensively for pre-surgical mapping, MEG has not achieved the same popularity as fMRI for pre-surgical mapping. This is likely due to the lesser availability of MEG scanners as compared to MRI machines, as MRI scanners are ubiquitous due to their anatomical imaging capabilities. In any case, both fMRI and MEG offer non-invasive means to perform whole-brain functional mapping. This confers the advantages of being safe, repeatable, and acceptable for use in research studies on healthy controls.

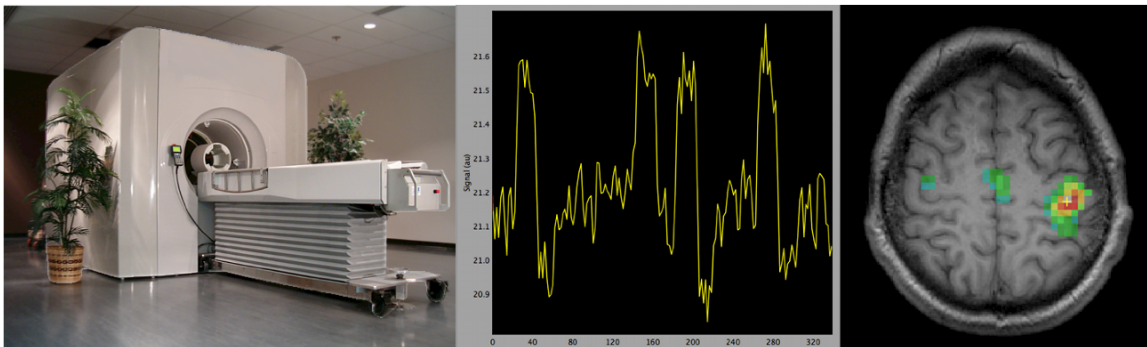


Figure 1.1: The 4 Tesla Varian fMRI scanner used in this thesis (left), a typical raw fMRI signal for a single task-responsive voxel (middle), and the resulting activation map produced by a finger tapping task (right).

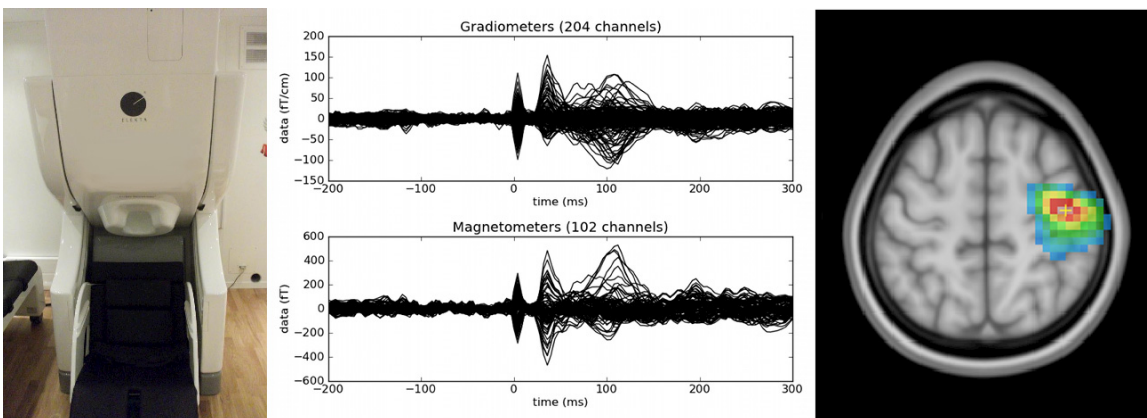


Figure 1.2: The 306-channel Elekta MEG scanner used in this thesis (left), typical accumulated sensor-level data (middle), and the resulting activation map produced by median nerve stimulation (right).

The use of fMRI and MEG for pre-surgical mapping has been validated by comparisons with CS. MEG validation studies have focussed primarily on somatosensory mapping [18–30], along with a number of studies on motor mapping [24, 28, 30–33], and relatively few for language mapping protocols [34, 35]. For fMRI, the majority of comparisons with CS have focussed on motor [29, 36–46] and language [37, 42, 44, 47–54] mapping, with less attention to somatosensory localization [55].

The agreement between the non-invasive mapping modalities and CS is highest for simple functions like primary sensory and motor, whereas for language localization the results are more equivocal. For example, motor mapping by fMRI can achieve

92% sensitivity [43], with lower bounds around 77% [45]. MEG can obtain very high sensitivity (98%) and specificity (94%) [31] for sensorimotor mapping, with up to 77% of MEG localizations being within 3 mm of CS locations [25]. However, larger discrepancies have been reported, in some cases greater than 12 mm on average [27]. Importantly, the MEG detection rate was unaffected by the presence of tumors [31], whereas fMRI signal is known to be suppressed near high-grade gliomas [56]. Korvenoja *et al.* found that MEG was more sensitive than fMRI for mapping the sensorimotor cortex, but notably used sensory mapping for MEG and a motor task for fMRI [29]. A recent report argues that CS remains a more reliable tool than fMRI for mapping the primary motor cortex, due to potential false negatives by fMRI [45]. Nonetheless, fMRI appears to be more reliable than anatomical MR imaging alone for identifying the primary motor area in the presence of pathological cortex, as demonstrated by Wengeroth *et al.* [46].

For language mapping, fMRI studies have shown a distinct trade-off between sensitivity and specificity. For instance, Roux *et al.* [51] found 91-97% specificity with 59-66% sensitivity, whereas Rutten *et al.* [50] found high sensitivity (100%) with lower specificity (61%). These seemingly contradictory results show that sensitivity can be traded for specificity depending on the methodology employed. Indeed, Rutten *et al.* used the conjunction of several language tasks in order to increase sensitivity, which clearly also decreases specificity. For MEG, no comparisons of language mapping to CS have been reported with sample sizes large enough to calculate sensitivity or specificity, but case reports indicate high concordance with CS [34,35]. Overall, there is considerable room for improvement of language mapping techniques in terms of predicting the location of eloquent cortex [57].

1.3 Single-Subject Imaging

One of the greatest challenges for functional MRI and MEG in pre-surgical mapping is performing robust imaging at the single-subject level. Single-subject imaging is clearly needed for clinical functional mapping, as we are interested in where a particular brain function is located in an individual patient - not in making generalizations to populations. However, single-subject mapping is difficult due to the inherently low signal-to-noise for both fMRI and MEG (see chapter 2). This is compounded

by artifacts associated with both intrinsic physiological signals (e.g. heart beat) or extrinsic issues, like subject motion. Many of these issues are amplified in patient populations, and additional issues arise with task compliance or performance associated with impacts of pathology.

There is a wealth of pre-processing tools available for fMRI and MEG to help deal with data quality issues or artifacts, but this places a burden on the user to determine the best pipeline for a given data set. While it is generally accepted that motion correction and spatial smoothing improves the reliability of fMRI maps, the impact of other pre-processing options is less clear [58–61]. This has led to the development of quantitative quality assurance metrics like ROC-r and NPAIRS (Nonparametric Prediction, Activation, Influence and Reliability), which are capable of evaluating the impact of pre-processing choices on a case-by-case basis. Previously, no analogous tool has been available for volumetric MEG source mapping, although goodness-of-fit parameters are routinely used to determine the quality of MEG dipole localizations, and automated processing of sensor level MEG data has been demonstrated [62, 63].

Even using individualized pre-processing strategies, the issue of thresholding functional maps to reveal the task-related areas is a significant challenge at the single-subject level. While threshold strategies for multiple-comparison control in group level analyses are well developed [64–67], these methods are not flexible enough to accommodate the significant inter-individual differences in activation. Even within individuals, significant variations in activation strength can be seen from run to run, including well known habituation effects. ROC-r provides an alternative method of individualized, data-driven thresholding by enforcing requirements on spatial reliability and placing minimal assumptions on the underlying data distributions.

ROC-r was developed for data quality assessment, pipeline optimization, and threshold selection based on spatial reliability of activation maps. Because this method operates on the final product of the pre-surgical mapping process (i.e. activation maps), and because the activation map is the common link between fMRI and MEG source imaging, ROC-r provides a unified approach to optimizing both modalities.

1.4 Research Objectives

In this thesis, we will demonstrate the utility of ROC-r across a variety of experimental conditions. We will convey the importance of taking an individualized approach to the analysis of pre-surgical mapping data, in order to produce the most reliable results. ROC-r will be shown to provide effective control of data quality for both MEG and fMRI, and the capabilities of this approach will be demonstrated *in situ* for pre-surgical mapping in patients with brain tumors. This thesis will consist primarily of a series of four manuscripts, addressing the following research objectives:

- Manuscript 1: Demonstrate validity of ROC-r as a measure of fMRI image reproducibility that is sensitive to individual variability (Ch. 3).
- Manuscript 2: Demonstrate the application of ROC-r for quality assurance and automated localization of volumetric MEG maps (Ch. 4).
- Manuscript 3: Show that ROC-r quality assurance and optimization improves the ability of pre-surgical fMRI to localize critical eloquent cortex (Ch. 5).
- Manuscript 4: Illustrate ROC-r as a common framework for processing optimization and automated thresholding of both MEG and fMRI images (Ch. 6).

Throughout these manuscripts, the themes of data quality assessment, optimization of pre-processing pipelines, and automated thresholding for the production of robust functional maps will be stressed.

Chapter 2

Theory

In this chapter, a brief discussion of the theoretical underpinnings of fMRI and MEG mapping will be presented. The generation of the relevant signals will be discussed, and the basic steps involved in the formation of statistical maps are outlined. A summary of the available techniques for thresholding statistical maps will be given, and finally a detailed description of the motivation behind and implementation of the ROC-r framework is presented.

2.1 Functional MRI

2.1.1 Signal Generation

Magnetic resonance imaging (MRI) is a non-invasive imaging technique, based on the interaction of the magnetic dipole moment of (typically hydrogen) nuclei in the body with a strong static magnetic field (\vec{B}_0). The torque experienced by the nuclear magnetic moment in this field leads to precession at the ‘Larmor frequency’ (ω_0), given by:

$$\omega_0 = \gamma B_0 \tag{2.1}$$

where γ is the gyromagnetic ratio (42.6 MHz/Telsa for Hydrogen). Macroscopically, this equilibrium state does not create an observable signal, as the bulk magnetization (\vec{M}) is constant in time due to a lack of (transverse) phase coherence of the precessing dipoles. The application of an orthogonal magnetic field in the form of a radio-frequency pulse tips this bulk magnetization vector into the transverse plane, and introduces the necessary phase coherence. This magnetization then produces an observable signal as it rotates and relaxes back to its equilibrium state (Figure 2.1). This relaxation is described by a longitudinal relaxation rate governing return to equilibrium (R1), and an apparent rate of signal loss (R2*) due to loss of transverse phase coherence.

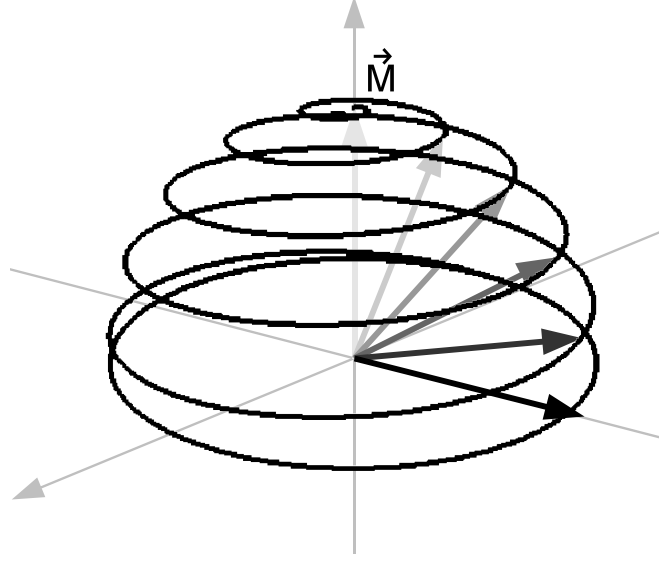


Figure 2.1: MR relaxation. After a radio-frequency excitation pulse, the magnetization vector \vec{M} is shown in the transverse plane. This proceeds to precess and relax back towards the equilibrium (longitudinal) state. The rate of return to equilibrium (R1) is typically longer than the rate of signal loss (R2*) due to loss of transverse phase coherence.

Functional MRI exploits endogenous contrast produced by the sensitivity of MR relaxation to the molecular environment of hydrogen protons. The most common fMRI techniques use the Blood Oxygen Level Dependent (BOLD) contrast generation first described by Ogawa *et al.* [15]. BOLD contrasts arises from changes in the transverse relaxation rate (R2*) of the MR signal caused by changes in the relative concentration of oxygenated and deoxygenated hemoglobin. Deoxygenated hemoglobin is paramagnetic, and increases the local magnetic susceptibility of blood when present. This in turn induces local field offsets compared to the static field around an idealized cylindrical blood vessel, (ΔB) given by:

$$\Delta B = 2\pi\Delta\chi(1 - Y)B_0\sin^2(\theta) \left(\frac{a}{r}\right)^2 \cos(2\phi) \quad (2.2)$$

outside of the blood vessel, where $\Delta\chi$ is the susceptibility difference between fully oxygenated and deoxygenated blood, $(1-Y)$ is the fraction of deoxygenated hemoglobin in the blood, B_0 is the main magnetic field, θ is the angle of the blood vessel to the main magnetic field, a is the radius of the vessel, r is the distance from the center of the vessel, and ϕ is the polar angle about the vessel (Figure 2.2a). Inside the blood

vessel, a constant field offset of:

$$\Delta B = 2\pi\Delta\chi(1 - Y)B_0(3\cos^2(\theta) - 1)/3 \quad (2.3)$$

is present (Figure 2.2). These intra-voxel field inhomogeneities lead to more rapid transverse relaxation of the MR signal as individual spins gain or lose phase due to precession in their local magnetic field.

The physiological links between BOLD contrast and brain function are complex [69], but essentially relate to increases in cerebral blood volume (CBV), cerebral blood flow (CBF), and cerebral metabolic rate of oxygen consumption (CMRO₂) following neuronal activity. The change in deoxyhemoglobin concentration inside a vessel (ΔY) can be shown to be:

$$\Delta Y = (1 - Y) \left(\frac{\Delta CBF/CBF - \Delta CMRO_2/CMRO_2}{\Delta CBF/CBF + 1} \right) \quad (2.4)$$

where Y is the baseline deoxyhemoglobin concentration. To some degree, these effects counteract each other as increases in CBV and CMRO₂ both increase local deoxyhemoglobin concentration, whereas increased CBF washes away deoxyhemoglobin, replacing it with fresh oxygenated blood. The dominating response is typically the CBF increase, which leads to a seemingly paradoxical overall increase in local blood oxygenation following neuronal activity (and therefore increased signal on a R2* weighted image) [68].

The time-course of the BOLD response to neural activity is referred to as the hemodynamic response function (HRF). The HRF is important to consider as it is needed for the analysis of fMRI images (Figure 2.3), and typically limits the temporal resolution of fMRI experiments. The main BOLD response, corresponding to the peak in the HRF, occurs approximately 5 seconds post-stimulus, with a full-width-half-maximum of 4-5 seconds. This is usually followed by a post-stimulus undershoot, which may take tens of seconds to fully return to baseline. An initial negative BOLD dip is sometimes observed as the CMRO₂ changes preceding the CBF and CBV responses, but is not robust enough to be used for functional mapping. The temporal sampling achieved in typical whole-brain fMRI studies (1-3 seconds) is thus sufficient to sample the main HRF components.

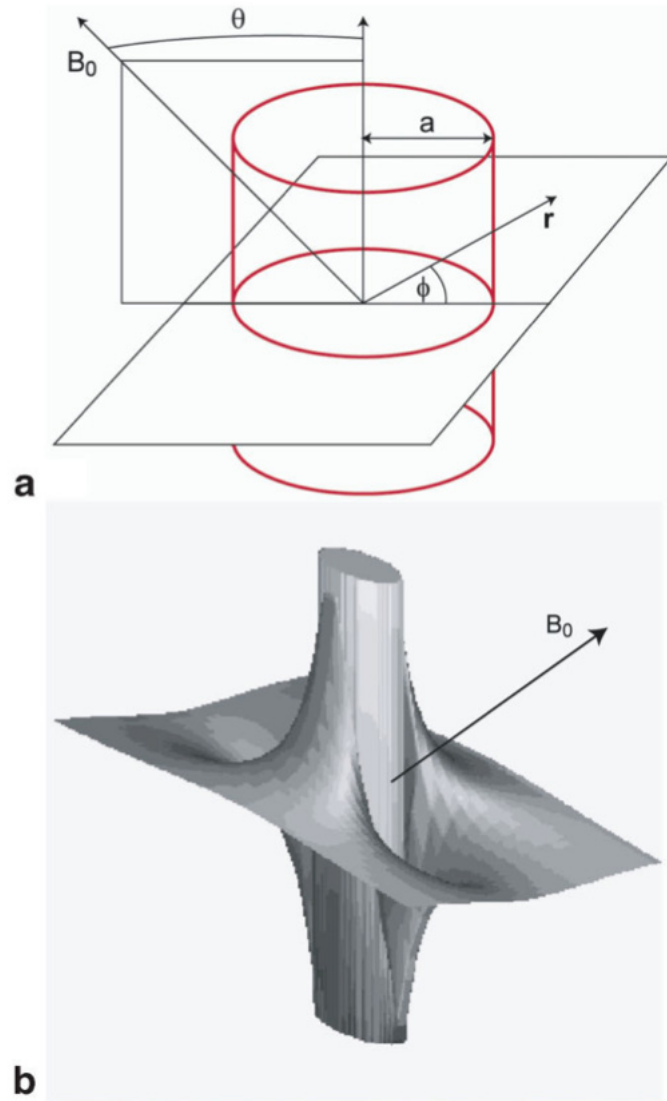


Figure 2.2: a) Idealized blood vessel represented as a uniform cylinder of radius ‘a’, at an angle (θ) to the static magnetic field (B_0). b) Field offsets in and around the vessel caused by magnetic susceptibility of deoxygenated hemoglobin in the blood. Adapted from [68].

2.1.2 Image Formation

Typical fMRI analysis pipelines include a variety of pre-processing steps including rigid-body co-registration of the fMRI images to initially correct for motion within the scanning session. Affine transformations are typically employed using the anatomical image as a template, in order to correct for geometric distortion. High-pass filtering is commonly performed to remove low-frequency drift from the fMRI signal, although this step can alternatively be incorporated into the general linear model (GLM, see below). Image smoothing is also commonly performed in the pre-processing pipeline, in order to increase the power for detection of activation, albeit at the cost of spatial resolution.

At the heart of fMRI analysis is the general linear model (Figure 2.3). For the GLM approach, the expected fMRI time-course is modelled by the convolution of a canonical HRF with the experimental timing (e.g. the stimuli, responses, or some contrast of predictors). The recorded voxel timecourse ($y_a(t)$) of an active voxel is assumed to follow the predicted timecourse ($f(t)$), plus additive effects of noise ($n(t)$), polynomial baseline variation ($P_a(t)$), and any other modelled sources of signal ($m(t)$, e.g. motion):

$$y_a(t) = \alpha_0 f(t) + P_a(t) + m(t) + n(t) \quad (2.5)$$

whereas an inactive voxel timecourse ($y_i(t)$) will not exhibit any task-related signal:

$$y_i(t) = P_i(t) + m(t) + n(t) \quad (2.6)$$

where α_0 estimates the magnitude of the task regressor in that particular voxel, and the polynomial baseline function ($P_i(t)$) is not necessarily the same as in the active case (although in practice the difference is typically small). By finding the value of α_0 that minimizes the sum-of-squares residuals, the magnitude of the task response is estimated for every voxel. Finally, a goodness-of-fit statistic for each voxel is calculated, for instance, by taking the ratio of the effect size (α_0) to a measure of the residual error:

$$t^* = \frac{\alpha}{MSE(\mathbf{X}^T \mathbf{X})^{-1}} \quad (2.7)$$

Where MSE is the mean squared residual error, and \mathbf{X} is the design matrix, specified

by the stimulus timing and nuisance regressors. In this work, the t- or z-statistic is used.

There are additional pre-processing options that can be implemented at the time of the GLM analysis. As alluded to previously, one of these options is the number of polynomial terms included in the baseline model of the GLM. Typically this is limited to quadratic or cubic terms, depending on the length of the fMRI experiment. The translation and rotation timecourses determined during rigid body motion correction are also frequently incorporated into the GLM model, a process called motion parameter regression (MPR). This procedure can be used to account for residual signal variation that correlates with subject motion, however it must be applied with caution as even small amounts of task-correlated motion may cause MPR to suppress fMRI sensitivity dramatically. Finally, auto-correlation correction (ACC), or pre-whitening, is frequently used to correct t-values for residual timecourse correlations that were not accounted for in the original GLM.

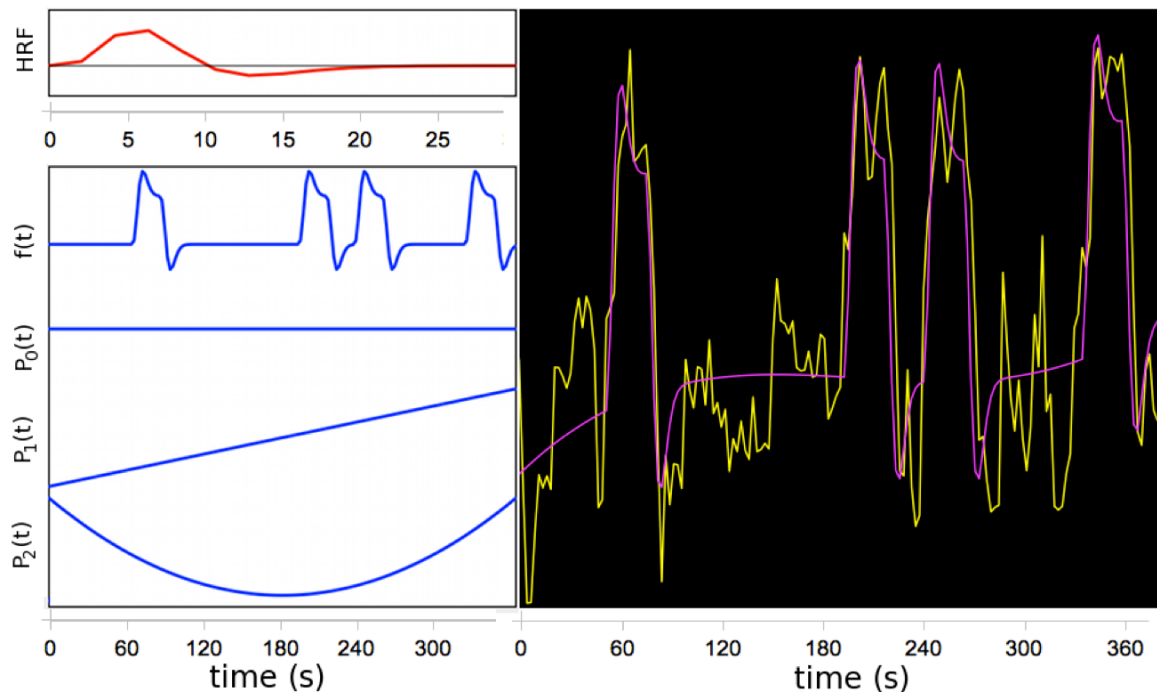


Figure 2.3: Example setup of a general linear model. Top left: canonical hemodynamic response function. Middle left: task block design convolved with HRF. Bottom left: polynomial terms for baseline model. Right: Voxel displaying high correlation to the GLM task model. Raw timecourse in yellow, fit voxel response in pink.

2.2 Magnetoencephalography

2.2.1 Signal Generation

Magnetoencephalography is also a non-invasive method of detecting brain function, but unlike fMRI, it is a passive recording technique. MEG measures the natural magnetic fields resulting from the coherent activity of small patches of cortex containing millions of neurons. The field strengths produced are incredibly small (tens to hundreds of femtoTesla, or about one billionth of the earth's field). It is thus necessary to perform MEG experiments in magnetically shielded environments, in order to suppress signals originating from outside the body. Even still, in typical experiments it is necessary to average the responses to many stimuli together in order to achieve sufficient signal-to-noise, producing an 'evoked response' (Figure 2.4).

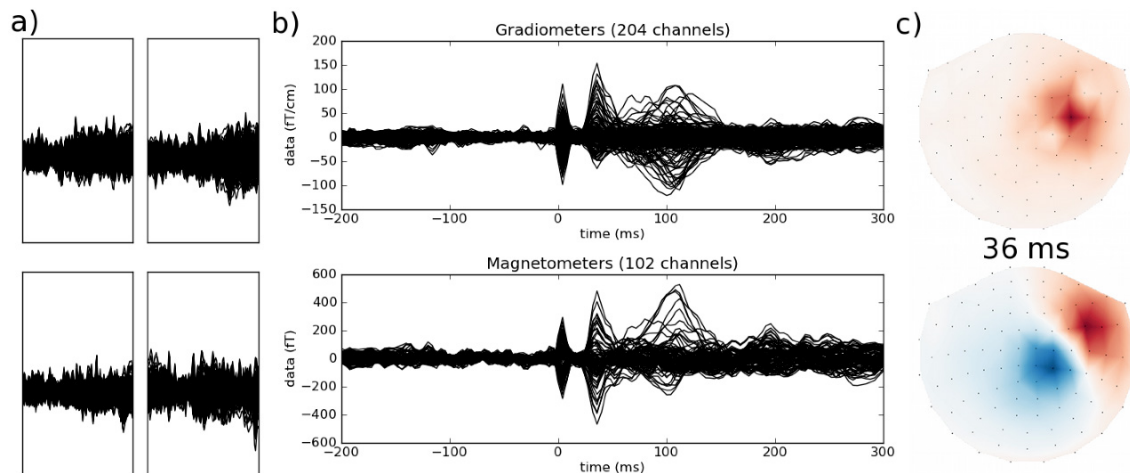


Figure 2.4: Representative MEG data from median nerve stimulation. a) Raw data epochs. The evoked response is not visible in single epochs. b) Averaged evoked response for the planar gradiometers (top) and axial magnetometers (bottom). c) Sensor topographies for the main deflection in the evoked response at 36 ms. The dipolar pattern is obvious on the magnetometers, corresponding to a source in the right parietal lobe.

The MEG signal arises primarily from excitatory post-synaptic input to the dendrites of cortical neurons [70] (Figure 2.5). Excitatory input causes small current inflow to the dendrites, which can be modelled as a current dipole. The coherent summation of many of these microscopic post-synaptic potentials produces the observed evoked response, and constitutes what is called the primary current source.

As the brain is by nature an electrically conductive medium, there are passive macroscopic ohmic return currents that ensure no net build-up of charge occurs. As we are interested in imaging only the primary currents, it is useful to formalize this distinction:

$$\vec{J}(\vec{r}) = \vec{J}_p(\vec{r}) + \sigma(\vec{r})\vec{E}(\vec{r}) \quad (2.8)$$

where $\vec{J}(\vec{r})$ is the total current density, $\vec{J}_p(\vec{r})$ is the primary current, $\sigma(\vec{r})$ is the conductivity of the medium, and $\vec{E}(\vec{r})$ is the macroscopic electric field.

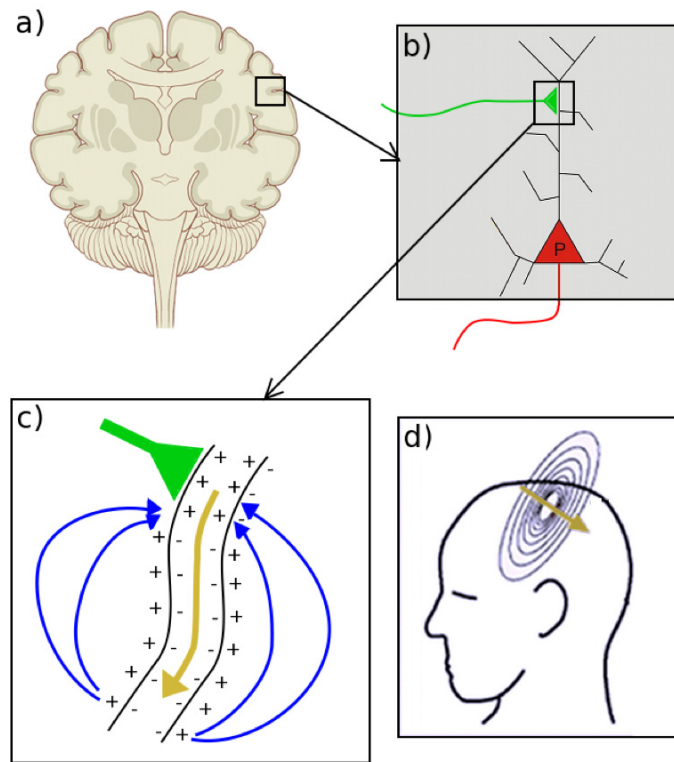


Figure 2.5: Diagram of the generation of the MEG signal. a) The MEG signal arises from post-synaptic potentials of cortical neurons. b) pyramidal neurons receive various inputs (green) along the dendrites, which propagate towards the cell body (red). c) the post-synaptic dendrite opens ion channels, allowing an influx of charge, and causing the primary current flow (yellow). Return currents (blue) ensure charge equilibrium. d) the primary current source (yellow) creates magnetic field that can be measured outside the head.

In order to localize the primary current density, it is necessary to understand the signal that is induced by both the primary and return currents, beginning with the magnetic field produced by these currents (the forward solution, Figure 2.6). It can

be shown that the return currents only contribute to the measured magnetic field where there is a gradient in electrical conductivity. Typically the head is assumed to be a piecewise homogeneous conductor, in which case the magnetic field can be shown to be:

$$\vec{B}(\vec{r}) = \vec{B}_p(\vec{r}) + \frac{\mu_0}{4\pi} \sum_{ij} (\sigma_i - \sigma_j) \int_{S_{ij}} V(\vec{r}') \frac{\vec{R}}{R^3} \times d\vec{S}'_{ij} \quad (2.9)$$

where $\vec{B}_p(\vec{r})$ is the field caused by the primary current, μ_0 is the permeability of free space, S_{ij} is the surface between compartments ‘i’ and ‘j’, $V(\vec{r}')$ is the electric potential, and \vec{R} is the vector from a position on the surface (\vec{r}') to the point of measurement (\vec{r}). This formula allows for the calculation of the magnetic field produced at the sensors by an arbitrary primary current source by calculating the potentials on compartment boundary surfaces. This procedure is commonly referred to as the boundary element method (BEM) [71]. Alternatively, a homogeneous sphere model can be employed, which is computationally simpler. The homogeneous sphere model gives adequate results in certain situations, but should not be used when highly accurate localization is required [72].

A closely related quantity to the forward solution is the lead field ($\vec{L}(\vec{r})$), which describes the sensitivity of the MEG detectors to a unit dipole at location \vec{r} . This formalism thus includes the orientation and type of MEG detector used in order to relate the fields produced by the dipoles to the signal induced on the sensors. By summing over all source locations in the brain volume, the MEG signal (\mathbf{m}) for an arbitrary source configuration can be calculated:

$$\mathbf{m} = \int \vec{L}(\vec{r}') \cdot \vec{J}(\vec{r}') d^3 r' \quad (2.10)$$

In practice, the leadfield is a discretized matrix \mathbf{L} , relating ‘m’ sensor readings to ‘n’ discrete brain locations.

2.2.2 Image Formation

Prior to image formation, there are an array of pre-processing steps that are commonly performed on MEG data. Removal of non-biomagnetic field components is

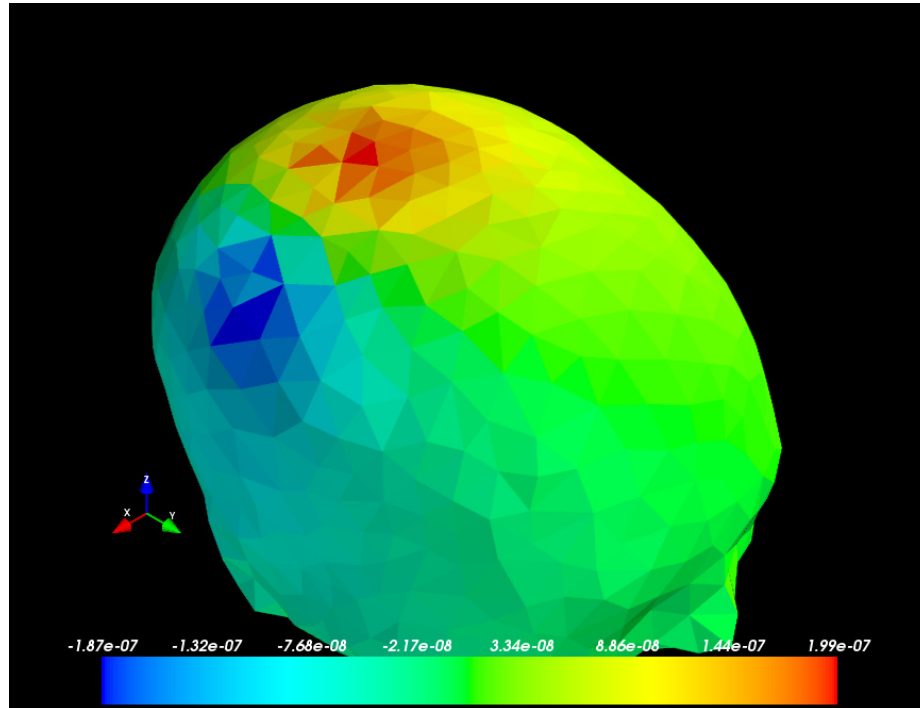


Figure 2.6: Normal component of the magnetic fields produced by a unit current dipole (1 Am) located in a cortical sulcus between the two field extrema (pointed in the anterior direction, tangential to the nearby head surface).

accomplished using either signal space separation techniques (SSS or tSSS), or reference sensor approaches. The raw data are usually band-pass filtered (e.g. 1-70 Hz), in order to restrict the spectral content to the range of typical brain signals. Down-sampling is frequently employed in order to reduce computational load. Independent component analysis (ICA) or other decomposition techniques (e.g. SSS) can also be used in order to separate the MEG signals into additive components. By correlating these components with known sources of artifact (e.g. eye blink or heart beat recordings), sources of noise can be pre-emptively removed from the raw data.

Many inverse solution / source mapping techniques are available for MEG. The earliest and most thoroughly investigated is the equivalent current dipole (ECD) [70], in which a single dipole is placed at the location and orientation that explains as much as possible of the observed field pattern. This point source technique is robust in many cases, but when distributed activations are expected, require the *a-priori* specification of the number of dipoles to model. For this reason, ‘dipole scanning’ techniques have been introduced, in which the dipolar source strength is estimated

independently for each location in a pre-defined grid.

Dipole scanning techniques find a unique solution to the MEG signal equation:

$$\mathbf{M} = \mathbf{L}\mathbf{Y} + \epsilon \quad (2.11)$$

independently for each spatial location on the source reconstruction grid (where \mathbf{M} is the measured signal across the sensors, \mathbf{L} is the discretized lead field, \mathbf{Y} is the grid of source strengths, and ϵ is additive noise). Beamformers are a particularly popular form of dipole scanning techniques, in which the amount of cross-talk to each location on the mapping grid is minimized (e.g. by enforcing a minimum variance constraint, or by increasingly penalizing contributions from other spatial locations based on their euclidean distance to the current point of interest) [73, 74]. While beamformers are not strictly speaking imaging techniques (as the extent of a beamformer ‘activation’ has no well defined meaning), they do produce a 3D estimate of source strengths, which in many ways resembles an activation map. More formally, only the peak locations of a beamformer map can be interpreted to represent a source localization.

Alternatively, true ‘imaging’ techniques for MEG source mapping attempt to find a full inversion of the matrix equation 2.11 [74]. As the number of sensors (m) is typically much less than the number of source points (n) in the reconstruction grid, this inversion is ill-posed, and some constraints must be introduced to find a unique solution. The most common constraints are the minimum norm or minimum current estimates (MNE and MCE respectively) [74, 75]. In these cases the solution with the least source power (MNE) or least total current (MCE) are found (i.e. minimizing the ℓ_2 or ℓ_1 norm respectively). While these solutions are attractive in the simplicity of their constraining assumptions, they typically result in very superficial source estimates, as a weaker source near the cortical surface (and therefore the sensors) would produce the same field as a stronger source further from the sensors. Less surface-biased solutions can be achieved by introducing depth weighting to the inversion matrix, or by adopting a noise-normalized approach like dynamic statistical parametric mapping (dSPM) or standardized low resolution brain electromagnetic tomography (sLORETA) [74, 76, 77]. In both of the latter two imaging approaches, the noise covariance is projected to each location on the source grid, and is used to normalize the source estimates. It has been shown that both depth weighting and

noise normalization can reduce the surface bias of MEG imaging approaches [78].

In this thesis, MEG source mapping is performed primarily by the linearly constrained minimum variance (LCMV) beamformer spatial filtering approach [73]. In general, LCMV beamformer spatial filters attempt to find a set of weights ($\mathbf{W}_{r_0}^T$) for the sensor data that project unity power to a voxel of interest (r_0), and minimal source variance elsewhere. The output of the spatial filter ($\mathbf{y}(\vec{r}, t)$):

$$\mathbf{y}(\vec{r}, t) = \mathbf{W}_{r_0}^T(\vec{r})\mathbf{m}(t) \quad (2.12)$$

is ideally equal to zero everywhere except the point of interest. The weights matrix is that which minimizes the total source power (P_{r_0}):

$$P_{r_0} = tr(\mathbf{W}_{r_0}^T \mathbf{C}_m \mathbf{W}_{r_0}) \quad (2.13)$$

where tr is the trace, and \mathbf{C}_m is the covariance matrix for the data. The weights are subject to unity gain at the point of interest:

$$\mathbf{W}_{r_0}^T \mathbf{L}_{r_0} = \mathbf{I} \quad (2.14)$$

It can be shown that the minimum variance beamformer solution is:

$$\mathbf{W}_{r_0}^T = \mathbf{C}_m^{-1} \mathbf{L}_r (\mathbf{L}_r^T \mathbf{C}_m^{-1} \mathbf{L}_r)^{-1} \quad (2.15)$$

and thus:

$$P_{r_0} = tr\left([\mathbf{L}_{r_0}^T \mathbf{C}_m^{-1} \mathbf{L}_{r_0}]^{-1}\right) \quad (2.16)$$

This procedure is repeated for each voxel in the source space, producing a map of source power. However, as MEG noise projects non-uniformly throughout the brain, the source estimates must be normalized to the projected noise power (N_{r_0} , e.g. from a pre-stimulus period):

$$N_{r_0} = tr\left([\mathbf{L}_{r_0}^T \mathbf{C}_n^{-1} \mathbf{L}_{r_0}]^{-1}\right) \quad (2.17)$$

where \mathbf{C}_n is the sensor noise covariance matrix. Thus the final beamformer output is

a ‘pseudo- Z ’ statistical map:

$$\begin{aligned} Z_{r_0}^2 &= \frac{\text{tr} \left([\mathbf{L}_{r_0}^T \mathbf{C}_m^{-1} \mathbf{L}_{r_0}]^{-1} \right)}{\text{tr} \left([\mathbf{L}_{r_0}^T \mathbf{C}_n^{-1} \mathbf{L}_{r_0}]^{-1} \right)} \\ &= \frac{P_{r_0}}{N_{r_0}} \end{aligned} \quad (2.18)$$

The beamformer output may be calculated for each time-point of the evoked response separately, in order to reconstruct dynamic (i.e. 4D) MEG source ‘images’.

2.3 Statistical Images and Thresholding

The fMRI and MEG image formation methods used in this thesis all result in statistical maps of brain activity - that is an estimate of signal strength relative to the variance or noise at that location. The final step in taking a pre-processed functional image and producing a fully processed activation map is thresholding the image into active and inactive areas. This introduces a fundamental issue for functional mapping - deciding what level of significance is appropriate for identifying active brain regions. Simple fixed error rates approaches are insufficient, due to the large number of brain voxels tested in typical functional mapping studies. For example, with 64x64x20 voxels, more than 80,000 tests are performed and a naive $p < 0.05$ significance threshold would result in more than 4000 false positive voxels.

Simple multiple comparison corrections like the Bonferroni correction are not suitable alternatives [66, 67], as the corrected p -values (p_B) assume that all voxels (V) represent an independent test:

$$p_B = \frac{p}{V} \quad (2.19)$$

As there is some degree of spatial correlation in functional images (e.g. regions of activity are not typically single voxels), the number of truly independent tests is much lower, and the Bonferroni correction is overly strict. An improved approach is to use gaussian random field (GRF) theory to estimate the image smoothness and determine the true number of independent tests that are available [64].

An alternative strategy is to specify an acceptable false discovery rate (FDR)

[65, 79], which is the proportion of false positives (FP) amongst the active voxels:

$$FDR = \frac{FP}{FP + TP} \quad (2.20)$$

where TP is the number of true positives. The significance level that satisfies this criteria (p_G) can be found by incrementally increasing the number of active voxels ‘ i ’, and finding the maximum number of voxels for which the i ’th p-value (p_i) satisfies the relation:

$$p_G = \max \left\{ i : p_i \leq \frac{iFDR}{V} \right\} \leq \frac{iFDR}{V} \quad (2.21)$$

The FDR and GRF approaches offer some degree of data-driven adaptation, and are widely used for group level studies. Both of these approaches are focussed on avoiding false positives, which may not be ideal in the context of clinical functional imaging, where false negatives are of greater concern in order to avoid incorrectly identifying a region of cortex as being safe to resect [80].

The above approaches specifying desired p-value levels of statistical significance all suffer from being essentially fixed-threshold techniques, which are unable to adapt sufficiently to individual variability in activation maps. One recently developed alternative is the adaptive thresholding method [80], which models image histograms as a combination of gaussian noise, and gamma activation/de-activation distributions. This approach is flexible to different levels of activation and noise, but does not incorporate the rich spatial information available in imaging. For MEG, thresholding methods based on permutation testing [81, 82] have been suggested, but in practice manual adjustment of threshold levels are still common, as no broadly accepted procedure has emerged. In general, data-driven methods are more suitable for dealing with individual variability than fixed significance or multiple comparison based methods, as the latter do not typically adjust to differing levels of noise or activation.

In this thesis, we present a data-driven thresholding strategy based on spatial reliability of activation maps. This technique will be shown to provide robust thresholded images for single-subject mapping. Furthermore, measuring reliability allows for evaluation of the pre-processing choices made to produce these maps, and for quality control of the activation images. This method of guiding functional image formation is described in detail in the following section.

2.4 The ROC-r Framework

2.4.1 Motivation and Background

Determining appropriate threshold levels is not the only challenge facing single-subject functional mapping. The low signal-to-noise inherent to both fMRI and MEG makes these techniques very sensitive to artifacts, and the quality of the resulting images is therefore highly dependent on the analysis methods employed. Unfortunately, there is no globally appropriate combination of processing choices that will produce the best results in all subjects. Several authors have shown the potential of ROC analysis for assessing the effect of processing choices on the resulting image quality [83–85]. In this thesis, a novel test-retest ROC-reliability framework will be introduced, and its usefulness for single-subject functional mapping will be demonstrated.

What makes the ROC-r approach particularly well suited to handle the variability of functional imaging, as well as the differences between fMRI and MEG data, is that minimal assumptions are placed on the activation maps. The two basic assumptions of the ROC-r method are: 1) the signal intensity in the images is larger than the noise amplitude, and 2) the signal originates from a consistent location across replications, whereas the noise amplitudes will be randomly distributed across the image. Being noise-normalized statistical maps, functional images implicitly satisfy assumption one. The second assumption is typically satisfied for scanner and physiological noise sources, but may be violated by some artifacts with systematic locations. Fortunately, sources of such artifacts tend to be easily recognized (e.g. eye blinks in MEG data), and methods for removing them from the raw data (e.g. epoch rejection) are widely available.

For images that meet these two assumptions, it is reasonable to assume that the spatial reliability of the images will increase with increasing threshold, as the spuriously located noise will be the first voxels to be thresholded out of the activation maps. Furthermore, once sufficient reliability is achieved, the threshold should not be increased further, in order to maintain activation sensitivity. Thus ROC-r provides information relevant to the selection of appropriate thresholds. It will be shown that the ROC-r method is also inherently capable of identifying poor quality datasets in

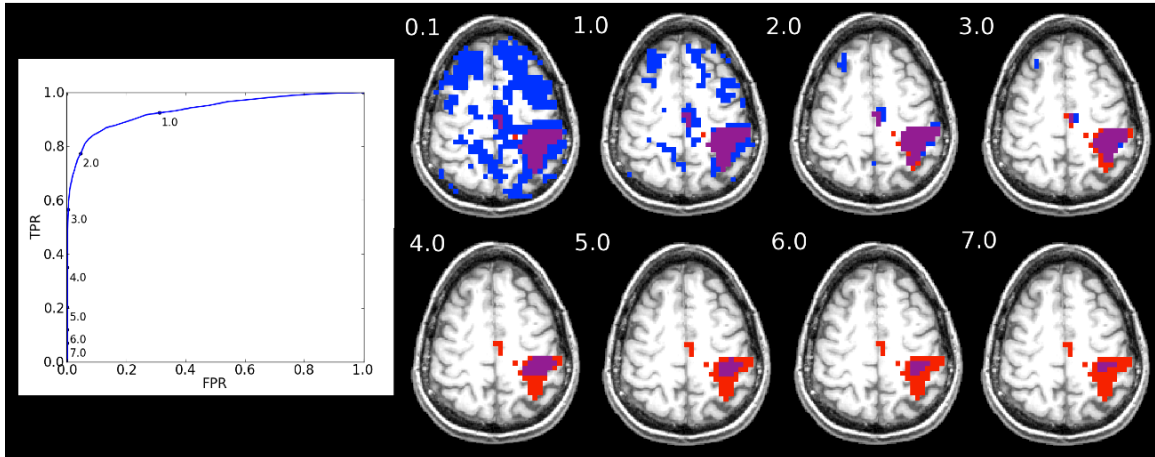


Figure 2.7: Demonstration of the ROC-r calculation of retest ROC curves. Left: ROC curve for an example template image thresholded at $t=3$. Right: Example template (red) and retest (blue) images for increasing retest image thresholds. Intermediate thresholds provide the optimal test-retest overlap (purple). This color scheme will be used extensively for showing ROC-r thresholded test-retest images.

which the above assumptions are not met, as the expected reliability versus threshold behaviour will not be observed (i.e. thresholding will not improve reliability due to lack of signal or presence of spurious artifacts). Finally, ROC-r can be used to guide pre-processing decisions, in order to improve the spatial reliability of activation maps. The ROC-r method is the only technique available that combines quantitative quality assurance metrics, pre-processing pipeline optimization, and automated individualized thresholding in a single package.

2.4.2 ROC-r Algorithm

The ROC-r algorithm calculates ROC curves based on the overlap of test-retest functional maps as a function of image thresholds. For the ROC-r calculation, one image (e.g. the ‘test’ image) is taken as the activation template for the ROC ‘gold standard’. The ROC curve (Figure 2.7) is defined as a plot of the true and false positive rates (TPR and FPR respectively), as a function of retest image threshold (t_2), at a fixed

template image threshold (t_1):

$$\begin{aligned} TPR(t_2) &= \frac{TP(t_2)}{TP(t_2) + FN(t_2)} \\ FPR(t_2) &= \frac{FP(t_2)}{FP(t_2) + TN(t_2)} \end{aligned} \quad (2.22)$$

where TP is the number of true positives (voxels active in both images, $A_{1,2}$), TN is the true negatives (voxels inactive in both images $I_{1,2}$), FP is the number of false positives (active in only the retest image A_2), and FN is the number of false negatives (active in only the template image A_1). The area under the ROC curve is calculated as a function of t_1 (i.e. $AUC(t_1)$), and used as the ROC-r indicator of retest reliability. The number of retest thresholds evaluated should be sufficient to produce accurate estimates of the retest ROC curves (typically ~ 20 threshold levels).

The retest ROC curves are highly dependent on the choice of template threshold. The ROC-r algorithm therefore explicitly evaluates the effect of the template threshold on retest image quality, by repeating the ROC and AUC calculation for all possible template image thresholds (Figure 2.8). This ensures that the resulting estimates of image reliability are not dependent on the choice of template threshold, and additionally allows one to determine threshold levels that produce robust template images directly. The basic output of a ROC-r analysis is thus a plot of the retest AUC as a function of template image threshold.

Overall reliability can be reduced to a quantitative metric for quality assurance purposes, and for determining the best analysis pipeline for a particular dataset. The metric of choice is the ‘reliable fraction’ (F_R), which is calculated as the fraction of the threshold range for which the activation pattern obtained is reliable (Figure 2.8):

$$F_R = \frac{\Delta t_{reliable}}{\Delta t_{reliable} + \Delta t_{unreliable}} \quad (2.23)$$

where the criteria for reliability is for the AUC to be above the ‘mid-range’ value (i.e. AUC_{mid} , half way between the minimum and maximum AUC values):

$$AUC_{mid} = \frac{AUC_f + AUC_i}{2} \quad (2.24)$$

This metric is particularly attractive as it measures how quickly the retest AUC (i.e. reliability) increases with template image threshold, and thus how much of the threshold range is reliable activation. For small activated regions, assuming random uncorrelated background noise, F_R is related to the image signal-to-noise ratio (SNR, see Figure 2.9).

The ROC-r AUC plots can also be used to determine data-driven thresholds. The approach taken in this work is to balance the desire for a high retest AUC with the diminishing returns observed at high thresholds. This is accomplished by defining the equivalent ‘linear-rate’ of AUC increase with threshold (AUC'_{lin}) as the slope of the line connecting the initial and final AUC values:

$$AUC'_{lin} = \frac{AUC_f - AUC_i}{t_f - t_i} \quad (2.25)$$

This provides a data-driven average rate of AUC increase with threshold (Figure 2.8). In order to balance the desire for high reliability with high sensitivity, the first threshold for which the AUC is above the mid-range value, and the rate of change drops below the linear-rate is identified as the ROC-r threshold. In earlier works (3) these cut-off parameters were determined from a group AUC plot, to take advantage

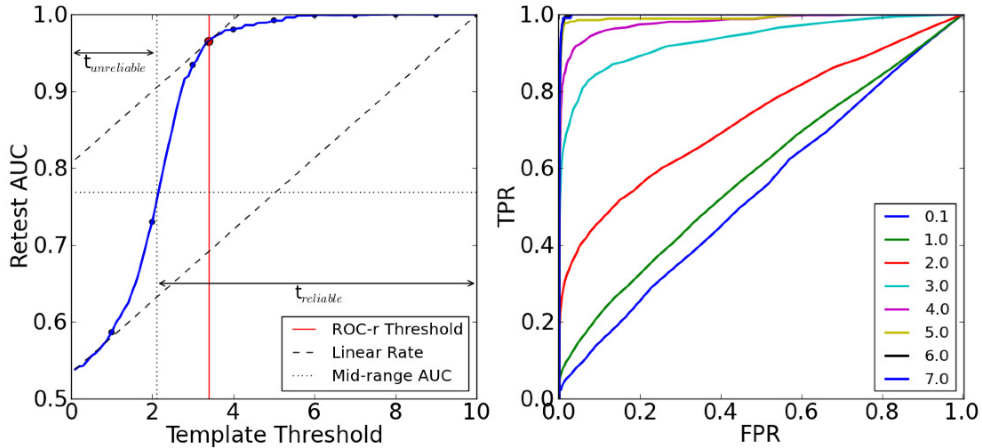


Figure 2.8: The output of the ROC-r analysis is a plot of the retest area under the curve (AUC) as a function of template image threshold (left). Overall reliability is measured by the fraction of the threshold range for which the AUC is above the mid-range value. The corresponding retest ROC curves for a variety of template thresholds is shown on the right.

of the stability provided by using the average ROC-r curves. However, in later works, these cut-offs are calculated directly from the individual ROC-r AUC plots, to offer greater individual adaptability. Two additional parameters can be introduced to fine-tune the ROC-r thresholds. The first such parameter, α , is used to increase or decrease the AUC cut-off value:

$$AUC_{thresh} = \alpha \frac{AUC_f + AUC_i}{2} \quad (2.26)$$

A second tuning parameter, β , can be introduced to allow variation of the conservativeness of the threshold levels:

$$AUC'_{thresh} = \beta \frac{AUC_f - AUC_i}{t_f - t_i} \quad (2.27)$$

Normally, both α and β are set to unity, unless otherwise noted. In chapter 5, the α and β parameters will be adjusted to increase the sensitivity of ROC-r thresholds in a patient group.

2.4.3 Simulation

A proof of concept for the ROC-r algorithm can be accomplished using a simple simulation (Figure 2.9). In this simulation, the images are represented using a 1D signal plus noise model. The signal was modeled by a gaussian distribution of varying full-width-half-maxima to represent different percent activation extents. The background noise was modelled by uncorrelated gaussian distributions of varying amplitude, to simulate different SNR levels. The noise magnitude was additionally scaled inversely to the amount of signal present in a given ‘voxel’, in order to represent a noise-normalized statistical map. For each SNR and activation extent, two 1D ‘images’ were simulated and submitted to a ROC-r analysis.

The initial AUC of the resulting ROC-r curves increases with activation extent, as a larger and larger proportion of the voxels are reliable at any threshold (Figure 2.9c). Thus the initial value of the AUC is not always 0.5, as would be expected for an image that is predominantly noise. The initial AUC value is thus indicative of the extent of the activation present in the images. The limiting cases of noise only images (AUC=0.5) and identical images (AUC=1.0) are also shown. Increasing the SNR does

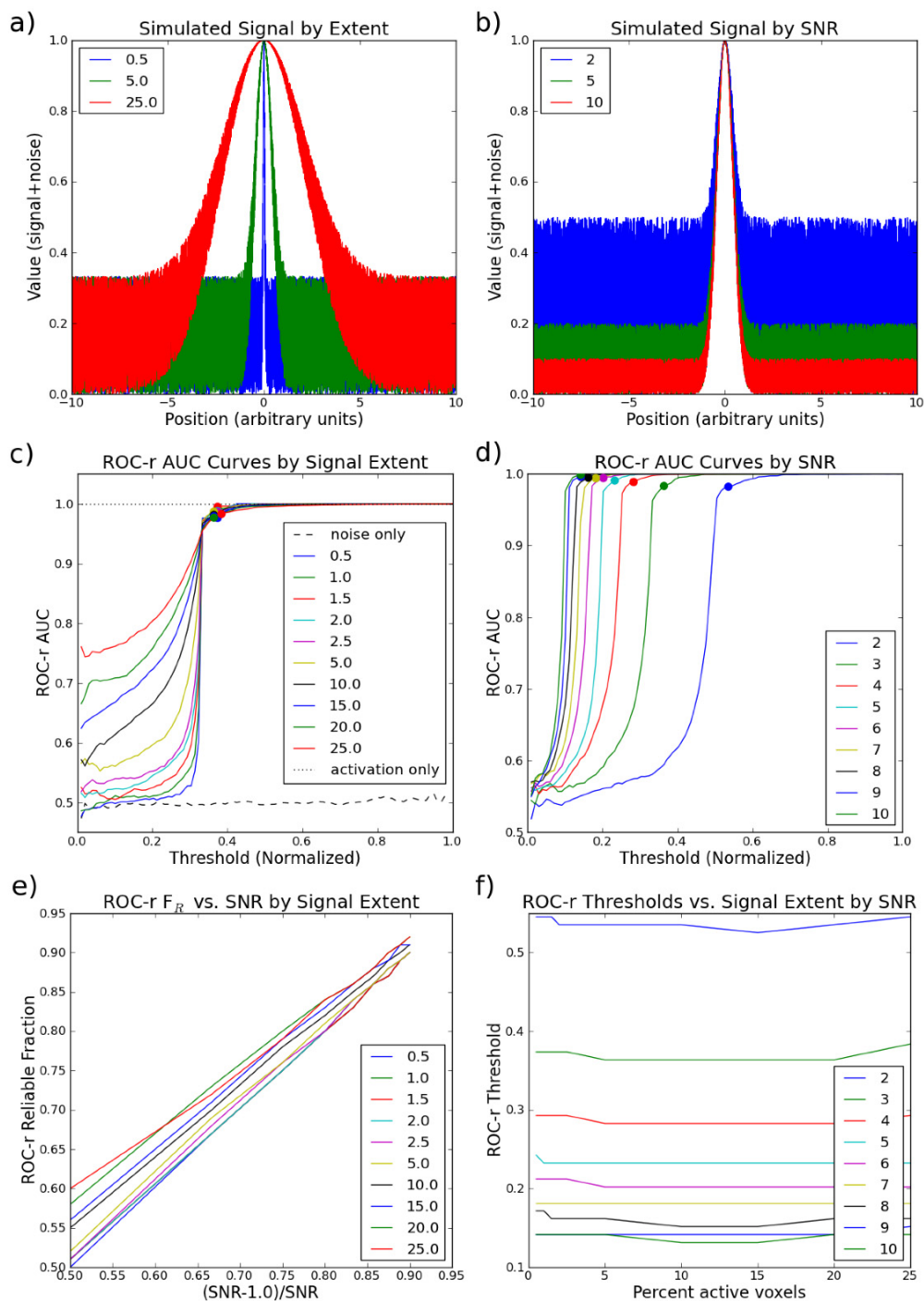


Figure 2.9: Simulated 1D signal for varying percent active voxels (a) and noise magnitude (b), and corresponding ROC-r analyses in (c) and (d), respectively. The ROC-r reliable fraction depends linearly on SNR, and is nearly independent of activation extent (e). The ROC-r thresholds increase with increasing noise levels, independent of activation extent (f).

not change the initial AUC value, but results in faster increase in AUC with threshold (Figure 2.9d). As a result, the reliable fraction increases with SNR, and is essentially independent of activation extent, especially for less than smaller percentages of active voxels (i.e. $\leq 10\%$). Likewise, the optimal threshold is independent of activation extent, but adapts for increasing noise levels, in order to isolate the reliable signal.

2.4.4 Repeatability, Reliability, and Accuracy

The ROC-r method is based on assessment of the test-retest reliability of functional maps. It should thus be emphasized that throughout this thesis, the term reliability is thus used in the same conceptual sense as repeatability or reproducibility of the functional images. It should also be noted that the repeatability of a test does not ensure validity of the result, although it can be considered a necessary - if not always sufficient - condition for the usefulness of a measurement. However, in general, a test is only considered valid if it is both repeatable and accurate.

While repeatability of functional imaging is relatively easy to assess, the accuracy of these maps is much more difficult to define, as there is no true gold standard measure for localization of brain function. In this thesis, several surrogates are used as standards for assessing the accuracy of ROC-r results. In cases where individual results are expected to be relatively homogenous, a group map can be used as a form of baseline expectations. In this case, accuracy is operationally defined as the closeness of individual results to the mean. In other cases, an established method for localization is available, and can be used to validate the ROC-r results, such as equivalent current dipoles for MEG. Finally, for the patient studies in this thesis, cortical stimulation is used as the gold standard for localization of brain function. While cortical stimulation has its drawbacks as a comparator for volumetric image-based methods, it is able to identify critical functional regions that must be spared during surgery, and is routinely used intraoperatively.

2.4.5 Summary

The ROC-r algorithm provides a quantitative method of assessing the reliability of activation maps. We will show that ROC-r provides a valuable tool in three distinct

roles for individual functional mapping: as a quality assurance indicator, for selecting of optimal pre-processing pipelines, and for determining data-driven thresholds. Because it only requires the activation maps as input, it is equally well suited to MEG and fMRI source mapping and providing a unified framework for push-button processing of both modalities. This thesis will demonstrate that these qualities provide enhanced pre-surgical mapping characteristics, by ensuring that the best possible results are produced from the available data, on an individualized basis.

Chapter 3

Manuscript 1: Thresholds in fMRI Studies: Reliable for Single Subjects?

Authors: Tynan Stevens, Ryan D'Arcy, Gerhard Stroink, David B. Clarke, Steven Beyea.

Status: Published

Journal: Journal of Neuroscience Methods

Volume: 219

Pages: 312-323

Date: 2013

Contribution: Conceptualization, Data Analysis, Primary Author

Copyright: Rights retained to include in thesis, no permission required.

3.1 Motivation

The following manuscript examines how the reliability of individual level mapping depends on thresholding. This manuscript introduces the ROC-r method, and compares it to an established method of evaluating test-retest overlap/reliability. This paper shows that production of reliable images requires data-driven thresholding, as there is a large variability in image reliability at a given threshold both between and within subjects. The ROC-r method of threshold selection is shown to control for image reliability effectively, and the potential for using ROC-r to guide pre-processing decisions to maximize the quality of activation maps is established. This manuscript lays the groundwork for the ROC-r method.

3.2 Abstract

Many studies have investigated test-retest reliability of active voxel classification for fMRI, which is increasingly important for emerging clinical applications. The implicit impact of voxel-wise thresholding on this type of reliability has previously been under-appreciated. This has had two detrimental effects: 1) reliability studies use different fixed thresholds, making comparison of results challenging; 2) typical studies do not assess reliability at the individual level, which could provide information for selecting activation thresholds. To show the limitations of traditional fixed-threshold approaches, we investigated the threshold dependence of fMRI reliability measures, with the goal of developing an automated threshold selection routine. For this purpose, we demonstrated threshold dependence of both novel (ROC-reliability or ROC-r) and established (Rombouts overlap or R_R) reliability measures. Both methods rely minimally on statistical assumptions, and provide a data-driven summary of the threshold-reliability relationship. We applied these methods to data from eight subjects performing a simple finger tapping task across repeated fMRI sessions. We showed that the reliability measures varied dramatically with threshold. This variation depended strongly on the individual tested. Finally, we demonstrated novel procedures using ROC-r and overlap analysis to optimize thresholds on a case-by-case basis. Ultimately, a method to determine robust individual-level activation maps represents a critical advance for fMRI as a diagnostic tool.

3.3 Introduction

3.3.1 Background

Functional MRI has emerged as a major diagnostic tool in human neuroscience. Most functional MRI maps reflect the statistical goodness-of-fit of a predicted response model to the signal measured in each voxel [86]. This process is used to overcome the noisy nature of the fMRI signal, but is hampered by the difficulty in defining an appropriate statistical threshold [64–67, 87]. In particular, differences between tasks, individuals, and scanners may not be properly accounted for in the statistical models used in fixed-threshold techniques (i.e. with pre-specified p-value levels) [88]. These problems are only made worse by sources of physiological noise and task-related

artifacts. As the threshold process is intended to separate the ‘active’ from ‘inactive’ voxels, it will clearly impact the reliability of the observed activation [89, 90].

Given that we cannot easily determine if a voxel is ‘truly’ active or inactive, measuring reliability through repeated scanning (e.g. within or between sessions) is one possible way to increase our confidence in the activation maps [39, 91]. However, there are many reliability measures to choose from [92], and each method is sensitive to different aspects of fMRI data. Furthermore, each method will be affected differently by decisions made during analysis (e.g. response model selection, spatial and temporal smoothing, etc: [84, 93]).

It is useful to divide the available approaches into two general categories: 1) magnitude and 2) classification reliability. Whereas reliability of activation strength or magnitude is investigated at the voxel level (e.g. with t-value scatter plots [94–98], or intra-class correlation coefficients [97–102]), reliability of active/inactive classification is assessed at the image level after application of a significance threshold. As we are principally interested in what effect the threshold has on fMRI mapping, we will focus on the latter, hereafter referred to as classification reliability.

Classification reliability has been shown to differ greatly between individuals [98, 103]. Despite this high individual variability, significant differences have been found between select patient and control groups [104]. Reliability has been shown to vary with functional tasks [105] and brain regions [97], two issues that are inevitably interrelated [97, 106]. Task-based and resting state fMRI can achieve similar reliability results [107], although task-based designs appear to be more robust when rest periods, rather than control states, are used as baseline [98]. The classification reliability also varies with threshold used to define the active/inactive voxels. This dependence is commonly characterized by either the test-retest true and false positive rates [88], or test-retest overlap coefficients [103].

We have developed data-driven methods to calculate classification reliability for individual subjects, using a test-retest framework. These methods alleviate the need for many task replications to accurately fit parameters in the traditional model-based approaches [108]. Our methods are designed to overcome large inter-individual differences in reliability that are observed when fixed thresholds are used in individual subjects. We will show that meaningful fMRI maps can be produced by optimizing

reliability of active/inactive voxel classification at the individual level.

3.3.2 Classification Reliability

The two most common ways to assess classification reliability for fMRI are overlap coefficients [97, 103, 105, 106, 109–114] and receiver operating characteristic (ROC) analysis [85, 88, 104, 107, 108, 115]. These two approaches differ in several ways.

Overlap Coefficients

Overlap coefficients are calculated directly from two thresholded activation maps. Therefore they are empirical measures of reliability. The two most common overlap indices are the Rombouts coefficient (R_R) [103], and the Jaccard overlap coefficient (R_J) [113, 116]. R_R is the ratio of the number of voxels active on both replications to the average number active on each replication. R_J is the proportion of voxels active in either replication that are active in both replications. Both R_R and R_J vary between 0 and 1, and are particularly attractive reliability metrics because of their simplicity. In this paper we will focus on R_R , as it is the more popular of the two metrics.

Overlap coefficients depend on the threshold used to classify active and inactive voxels [89, 90]. Rombouts *et al.* showed that the overlap coefficient is high at very low thresholds, and low at very high thresholds [89], as expected. While the report of Rombouts *et al.* demonstrated a local maximum in overlap at intermediate thresholds, a later study [90] did not reproduce this result. The variation in overlap was substantial in both studies: 0.0 to 0.7 in Rombouts *et al.* [89], and 0.21 ± 0.05 to 0.64 ± 0.03 in Duncan *et al.* [90], depending on the threshold used. It has recently been shown that adaptive thresholding can improve reliability beyond what is possible using a fixed threshold approach [80].

While the dependence of R_R on threshold has been known since shortly after its original demonstration [89], the majority of reliability studies focus on a single reliability threshold. Moreover, the thresholding level used varies from study to study. This has led to dramatic variation in the range of overlap reported by individual studies (average R_R from 0.230 to 0.856) [92].

ROC Analysis

The ROC curve is a plot of true positive and false positive rates (TPR, FPR; sometimes called ‘hits’ and ‘false alarms’) as a function of the classification threshold. ROC reliability can be summarized by the area under the curve (AUC). The AUC may vary from 0.0 (no true positives at any false positive rate) to 1.0 (no false negatives at any false positive rate). However, in practice it is rare for the AUC to be less than 0.5, as this is 50% classification accuracy, and could be obtained by randomly assigning active and inactive voxels. The AUC is useful for comparisons between experimental conditions, or with other reliability measures like R_R [104].

The most popular ROC analysis for fMRI data were developed by Genovese *et al.* [88], and further investigated by others [104, 107, 115, 117]. The Genovese ROC method uses a model-based approach to estimate the true and false positive rates. In their model, they asserted that for a series of ‘M’ test-retest replications, the number of times a voxel is found above a particular threshold, ‘n’, is drawn from a mixture of true and false positive detection probabilities (P_A , P_I) in proportion to underlying fraction of active voxels (λ):

$$n = \lambda \text{Binomial}(M, P_A) + (1 - \lambda) \text{Binomial}(M, P_I) \quad (3.1)$$

By calculating ‘n’ for all voxels, they are able to estimate P_A , P_I , and λ . They then repeat this method for many threshold values to estimate an ROC curve (i.e. use P_A , P_I to approximate TPR and FPR). A drawback of this process is that it depends on the availability of a large number of task replications to produce accurate estimates of P_A , P_I , and λ [108].

An alternative, test-retest method of ROC estimation was proposed by Le and Hu [85]. Le and Hu used a long fMRI experiment with a conservative ($p < 0.0005$) statistical threshold to estimate a true positive map. An ROC curve was then generated by varying the threshold on the second fMRI dataset, and calculating the TPR and FPR at each threshold. In this method, the TPR and FPR are calculated from overlapping/non-overlapping regions of the two images, and therefore operates using a similar framework to other empirical overlap coefficients. These are more accurately described as ‘test-retest positive’ and ‘test-retest negative’ rates, however we

will maintain the standard nomenclature of TPR and FPR. The impact of varying the threshold used to estimate the true positive map was not reported.

3.3.3 Research Objectives

We aim to compare the effects of threshold on both the established overlap coefficient (R_R) and novel ROC-reliability (ROC-r) analyses. For this purpose, we will investigate eight healthy individuals across two sessions (test-retest), using a standard finger tapping task. We will show that threshold dependence and individual variability leads to two outcomes: 1) reliability studies using different thresholds should not be directly compared, and 2) reliability should be measured and controlled for at the individual level to better ensure replicable results. Finally we will demonstrate new techniques for optimizing fMRI threshold selection using ROC-r analysis. These techniques produce automated, data-driven thresholds, resulting in robust activation maps at the individual level.

3.4 Methods

3.4.1 Participants

Eight healthy volunteers were recruited for this study (4 males, 4 females, 24.4 ± 3.5 years of age). All participants were right hand dominant according to the Edinburgh Handedness Inventory [118]. The subjects all spoke English as their first language, and had either normal or corrected-to-normal vision. The subjects had no known prior neurological conditions. Subjects were each scanned at 4 Tesla, using a simple motor task. Test-retest imaging was performed in separate scanning sessions 1-7 days apart. The study was approved by the local research ethics board (Capital District Health Authority REB, Halifax, NS), and all subjects provided informed consent.

3.4.2 MRI Acquisition Details

All eight volunteers were scanned twice with a 4 Tesla scanner (Varian INOVA, Palo Alto, California), for a total of 16 scanning sessions. During each session, both structural and functional images were acquired. The structural images were collected with an MP-FLASH sequence with the following parameters: TI = 500 ms, TR = 10

ms, TE = 5 ms, $\alpha = 11^\circ$, 256 x 256 matrix, 64 slices, and 0.94 x 0.94 x 3 mm voxels (FOV = 24 x 24 x 19 cm). Functional images were collected with a single-shot spiral out sequence, using TR = 2 s, TE = 15 ms, $\alpha = 90^\circ$, 64 x 64 matrix, 22 slices, and 3.75 x 3.75 x 5 mm voxels, with a 0.5 mm gap (FOV = 24 x 24 x 12 cm).

3.4.3 Functional Task

Each participant performed a finger tapping task that utilized a block design, consisting of 20-second alternating blocks of stimulation and rest. Left and right hand ascending/descending thumb-to-digit tapping blocks were interspersed with rest blocks (4 blocks/condition). Pace was fixed at 2 Hz using four circles (for four fingers) to control for finger tapping order and timing. Active block order was pseudo-randomized, with a rest block before and after each active block, for a total time of 5 minutes and 40 seconds (170 volumes). Stimuli were presented using E-Prime (Psychology Software Tools Inc.) via a projector in the MR console room. Subjects viewed the stimuli on a screen through a mirror mounted on the head coil. Task practice was done before each session to ensure optimal task performance.

3.4.4 Functional MRI Analysis

Functional MRI analysis was performed using the AFNI software package [119]. Data were first motion corrected by rigid body transformation to align all images with the first image of that time series. Segmentation was performed to remove the skull from both the functional and anatomical images. The high-resolution anatomical images were down-sampled to the functional image resolution prior to calculating a registration transformation (12 parameter affine). Functional MRI data were spatially smoothed (Gaussian kernel of 6 mm FWHM) prior to statistical analysis.

For statistical analysis, a standard boxcar function was convolved with the default AFNI hemodynamic response. Constant, linear, and quadratic terms were included in the baseline model to account for low frequency drifts. For each unique linear combination of the task regressors, the 3dDeconvolve program [119] was used to estimate the goodness-of-fit of the task activation model, and a t-statistic map was created. Group level activation maps for each contrast were created using a t-test after registration to the MNI-152 brain, and thresholded at FDR corrected $q = 0.01$

(approximately $p = 2 \times 10^{-5}$ uncorrected).

3.4.5 Reliability Calculations

In this work, both overlap coefficients and ROC-reliability (ROC-r) curves were calculated from pairs of test-retest images. Reproducibility analysis routines were programmed in Python and performed in individual space. Analysis was restricted to positive task correlations only, as we observed that the negative task correlations were substantially less reliable (by either overlap or ROC-r evaluation - data not shown). The number of unique voxels classified active in only the first image (A_1) and only the second image (A_2) were calculated (for independently varying thresholds t_1 and t_2). I_1 and I_2 were then calculated as the number of unique inactive voxels in each image, at the same pair of thresholds. $I_{1,2}$ denoted the number of shared voxels declared inactive (i.e. inactive in both images), and $A_{1,2}$ the voxels classified active on both images (Figure 3.1).

Overlap Coefficients

In terms of the active/inactive voxel counts defined above, the Rombouts overlap was calculated as $R_R = 2A_{1,2}/[A_1+2A_{1,2}+A_2]$ [92]. For each image pair, for each subject, R_R was calculated as a function of the threshold applied to both the test image (t_1) and retest image (t_2). Group results were obtained by averaging R_R produced at the individual level.

ROC-reliability

Our ROC-reliability estimation procedure (ROC-r) was based on the method outlined by Le and Hu [85]. We defined true positives as the voxels that were declared active in both images (i.e. $TP = A_{1,2}$). Those which were below threshold in both images were counted as true negatives ($TN = I_{1,2}$). False positives were counted from the voxels active in the retest image that were not active in the template ($FP = A_2$), and vice-versa for false negatives (i.e. $FN = A_1$). The true and false positive rates were then calculated in the usual fashion ($TPR = A_{1,2}/[A_{1,2}+A_1]$, $FPR = A_2/[A_2+I_{1,2}]$). The TPR and FPR were calculated for all values of t_2 at a fixed value of t_1 to produce

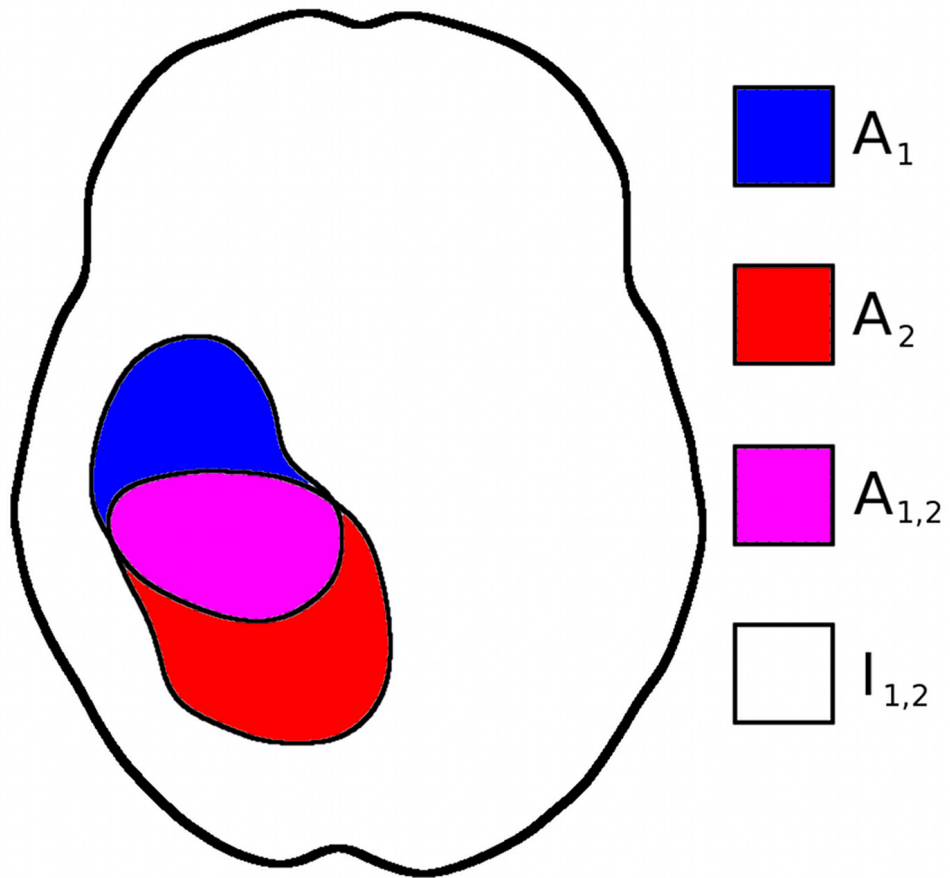


Figure 3.1: Schematic of test-retest overlap regions. Both the Rombouts coefficient and the true/false positive rates used for the ROC-r analysis are calculated from the overlapping/non-overlapping regions of fMRI images. Here A_1 and A_2 are the unique volumes classified active in only the first and only the second image respectively, $A_{1,2}$ is the shared activated volume, and $I_{1,2}$ is the common inactive volume (adapted from Rombouts [103]).

an ROC curve. These true and false positive rate estimates are based purely on test-retest measures, as the ‘true’ activity state of fMRI voxels cannot be obtained.

Whereas Le and Hu used a restrictive threshold level for t_1 , for the ROC-r methods we repeated the ROC calculation for all values of t_1 . The effect of restricting or expanding the template activation was then assessed quantitatively by plotting the AUC against t_1 . As we used identical procedures to obtain our test and retest images, the designation of one image as the template is arbitrary. For this reason both images were assessed as the template, resulting in two AUC plots for each test-retest pair. This procedure, and the subsequent analyses in section 3.5.2 we refer to as ROC-r, and is demonstrated in Figure 3.2.

3.4.6 Threshold Optimization

We developed an automated and empirical threshold optimization procedure using the ROC-r framework described in Figure 3.2. As exemplified in Figure 3.2, the AUC tends to increase monotonically as a function of template threshold. As the majority of inactive voxels are removed from the template image with increasing threshold, the rate of AUC increase declines. In order to balance the aims of achieving a high test-retest AUC (i.e. high reliability) and maintaining sensitivity to activation, we designed optimization procedures that consider both the AUC value and its rate of increase.

The AUC plots produced by the ROC-r analysis were fit with a smoothed cubic spline to obtain a smooth estimate of the first derivative. Optimal thresholds were taken as the first threshold for which the following two conditions were satisfied: 1) the AUC has increased to at least half of its maximum value (i.e. $AUC \geq [AUC_i + AUC_f]/2$) and 2) the AUC derivative has dropped below its average value (i.e. $AUC' \leq [AUC_f - AUC_i]/[t_f - t_i]$). Where AUC_i and AUC_f are the initial and final AUC values taken from the group mean. For comparison, we will also determine reliability optimized thresholds from the Rombouts overlap analysis by identifying local maxima in R_R as optimal threshold combinations.

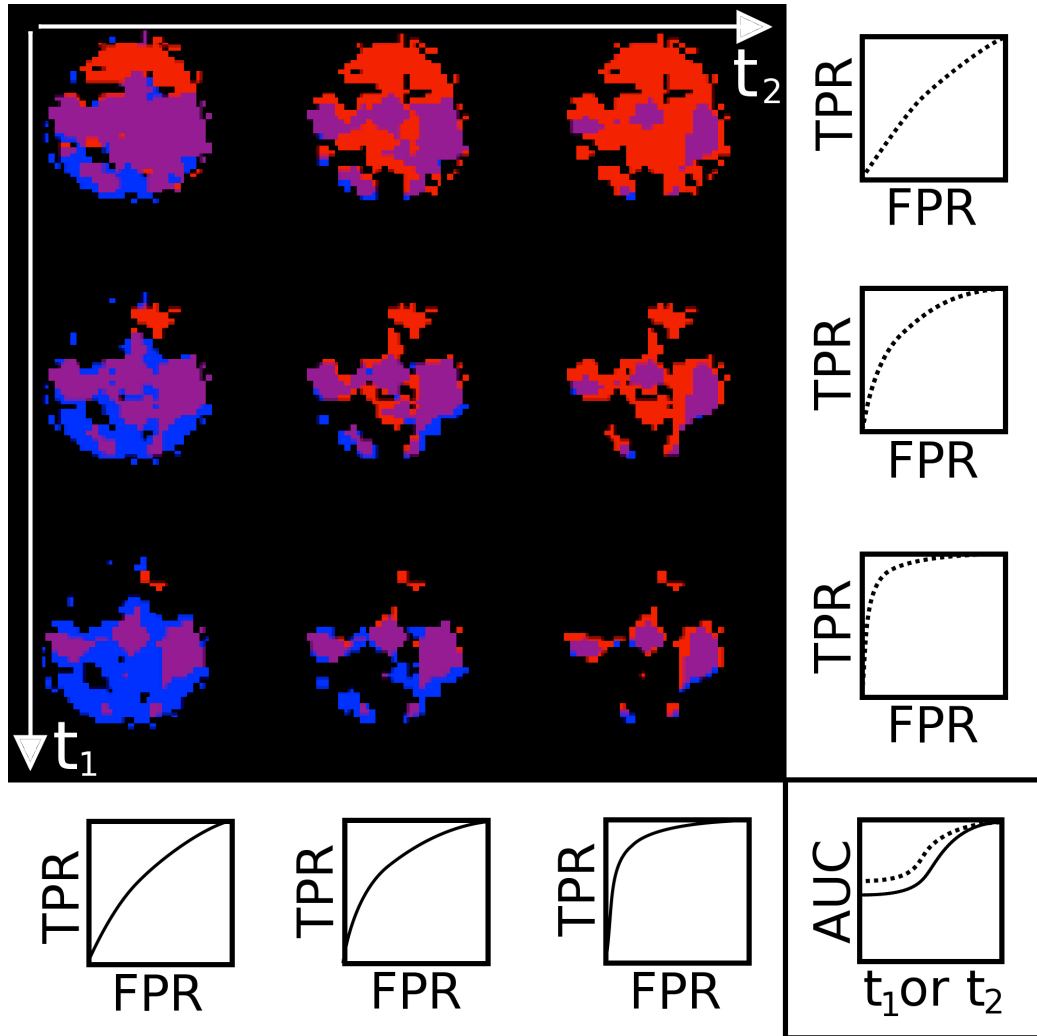


Figure 3.2: Schematic of the ROC-r method. At a given pair of image thresholds (t_1 , t_2), the TPR and FPR are calculated from the overlapping/non-overlapping regions. Repeating this for all t_2 values at a fixed t_1 produces an ROC curve, from which the AUC is calculated. This is repeated for all t_1 values to produce a plot of AUC vs. t_1 . The roles of the two images are then reversed to create both an AUC vs. t_1 and AUC vs. t_2 plot.

3.5 Results

3.5.1 Group Analysis

The right hand tapping condition of the motor task produced left-lateralized activation of the pre- and post-central gyri, supplementary motor areas, posterior cingulate gyri, striatum, and thalamus. Activity was also observed bilaterally in the visual cortex (occipital pole and lateral occipital cortex), and in the left cerebellum (Figure 3.3a). The left hand condition of the finger tapping task produced a similar distribution of activation, with more bilateral activation than that identified in the right hand condition (Figure 3.3b). Subject 6 was excluded from the group map due to motion issues.

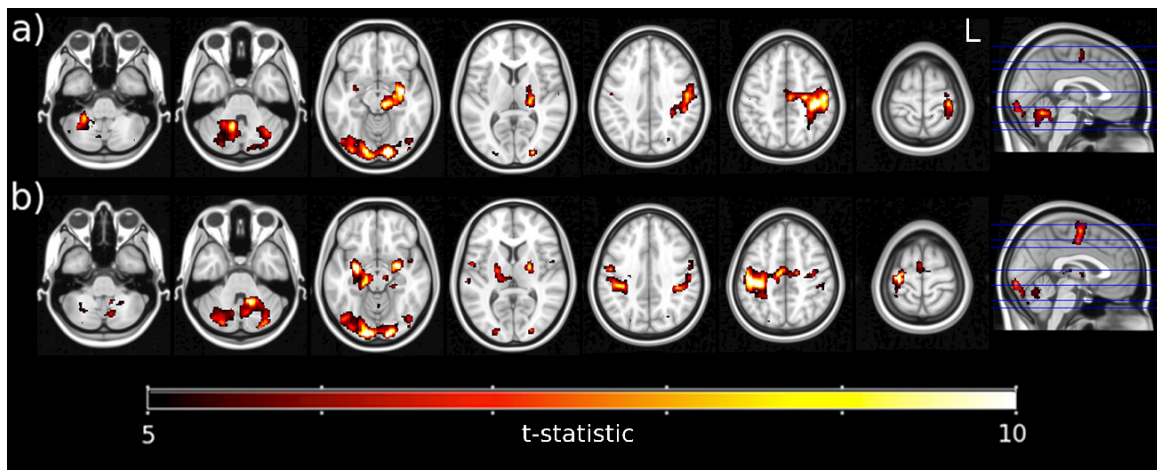


Figure 3.3: Group fMRI results ($n=7$). Group mean thresholded at $t \geq 5$ (FDR corrected $q \leq 0.01$): a) right hand contrasted to rest, b) left hand contrasted to rest (shown in radiological convention). The slices shown highlight the most extensive activated regions, and correspond to the axial slices indicated on the right. See the text for a full description of the corresponding anatomical locations.

3.5.2 Group Average Threshold-Reliability Dependence

Overlap Coefficient

Mean reproducibility was measured by averaging R_R across individuals (figure 3.4a). This grand average shows a trend of decreasing reproducibility as the threshold is increased, dropping rapidly from $R_R=1.0$ to $R_R=0.67 \pm 0.03$ as the threshold is

increased from $t = 0$ to $t = 2.6$ (approximately uncorrected $p = 0.01$). The average overlap coefficient then continues to decrease at a slower rate for higher analysis thresholds. This creates the appearance of an extended ‘tail’ region to the overlap plot, which in the group average occurs at equal analysis thresholds t_1 and t_2 . This tail region is highly variable across the group (figure 3.4b). From $t = 2.6$ to $t = 6.6$ (i.e. approximately uncorrected $p = 0.01$ to $p = 1 \times 10^{-6}$), the overlap decreases from 0.67 ± 0.03 to 0.56 ± 0.03

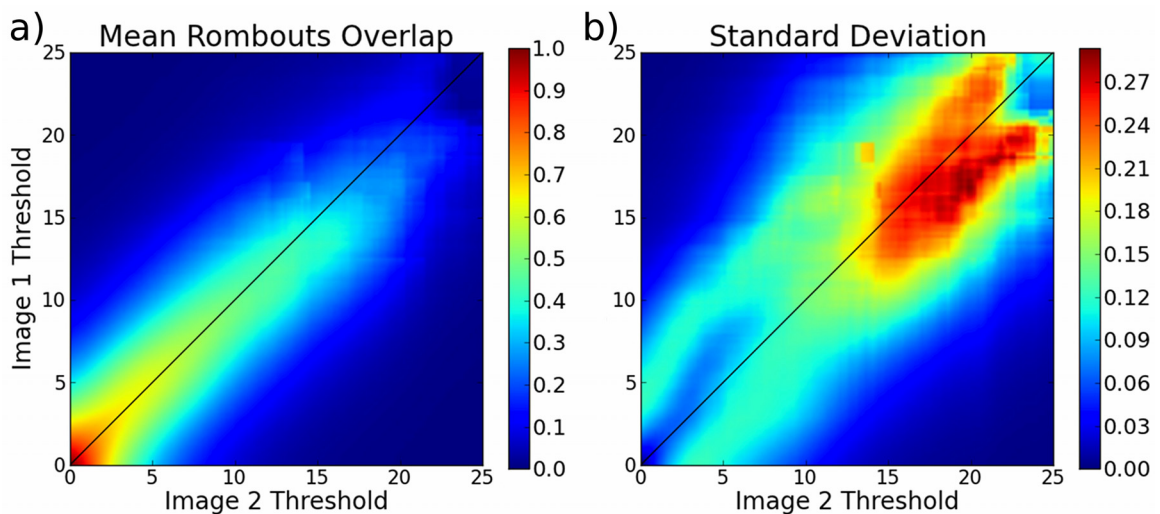


Figure 3.4: Group mean overlap coefficient (a), and standard deviation (b) as a function of independent image thresholds. The group averaged result obfuscates many phenomenon that may be observed at the individual level, as evidenced by the high subject-to-subject variability at high thresholds.

ROC-r

In the ROC-r analysis, the average of the single-subject AUC curves was found to increase monotonically with threshold on the template image (figure 3.5). This increase is initially rapid, as more and more inactive voxels are thresholded out of the test-image. From $t_1 = 0$ to $t_1 = 5$, the average AUC increases from 0.69 ± 0.01 to 0.87 ± 0.01 , and then more slowly thereafter. Note that an AUC of 0.5 is the same as random classification, so by this measure the classification reliability is reasonably above chance even at low thresholds. As the test-image becomes more representative

of the true active voxel distribution, the retest AUC increases more slowly, approaching 1.0 asymptotically. The average AUC varied from 0.78 ± 0.01 to 0.91 ± 0.02 as the analysis threshold was varied over the typical analysis range ($p = 0.05$ to $p = 1 \times 10^{-6}$ uncorrected).

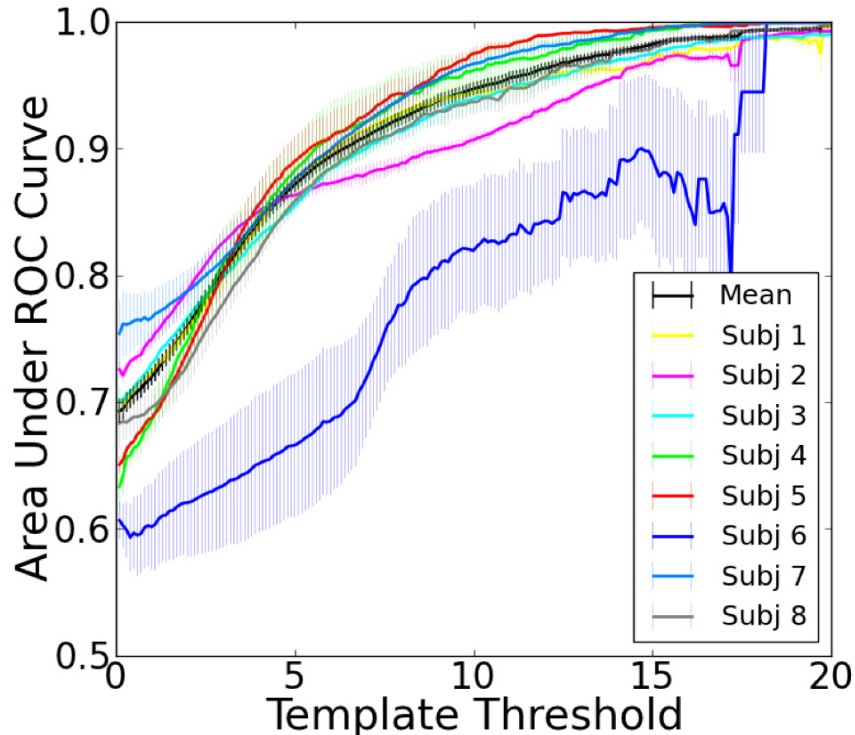


Figure 3.5: Individual ROC-reliability results (average \pm standard deviation of test-retest AUC): The AUC generally increases with test-image threshold, rapidly at first and then to diminishing returns. Subjects 2 and 6 are identified as having significantly below average AUC, whereas subjects 5 and 7 have above average reliability by the ROC-r analysis.

3.5.3 Individual Variability

Overlap Coefficient

At the individual level, the overlap-threshold relationship was more featured, and highly variable (Figure 3.6). Many subjects demonstrated local maxima, and these were frequently off-diagonal (i.e. not on the line $t_1 = t_2$). In some cases multiple local maxima were observed. The variability in the location of these local maxima

contributed to their averaging out at the group level, producing the plateau region observed in Figure 3.4. Therefore the group result likely does not represent a consistent trend, but rather a lack of consistent behaviour at the individual level. Subject 6 had the lowest overlap coefficients in the tail region, in agreement with the ROC-r analysis discussed below. Subjects 5 and 7 were identified as above average by the AUC plots, and also appear to have above average overlap coefficients in the tail region. These two subjects demonstrated overlap maxima at extremely high threshold levels, suggesting the presence of a few strongly activated, and highly reliable voxels.

ROC-r

Although qualitatively the ROC-r AUC plots looked very similar, significant quantitative differences were found between individual subjects, and between single subjects and the group mean (Figure 3.5). In particular, the AUC for subject 7 is significantly greater than the mean over all test-image thresholds tested. The AUC for subjects 4 and 5 begin below average but at $t \approx 4.0$ intersect the average, and thereafter is above the group mean. Subject 2 exhibits the opposite trend, beginning above average and crossing to below average for higher thresholds. Subject 6 is the clear outlier, exhibiting below average AUC over all test-image thresholds. This subject also exhibited an early plateau in the AUC plot, and downward spikes around $t = 17$. This subject required substantial motion correction (~ 1 mm displacement), suggesting that motion artifact may be contributing to the reduced reliability.

Threshold Optimization

The ROC-r threshold optimization successfully identified reliable activation in all but the least reliable subject (i.e. subject 6). For the seven subjects in which ROC-r based optimization succeeded, the resulting thresholds were $\bar{t}_{ROC-r} = 6.1 \pm 1.3$, resulting in $n = 1600 \pm 1200$ active voxels (means \pm st.dev.). These optimized thresholds are slightly higher than the Bonferroni corrected threshold of $t_{bonf} = 5.2$ (i.e. corrected $p = 0.01$), and significantly higher than the FDR corrected threshold of $t_{FDR} = 3.6$ (i.e. $q = 0.01$). The number of voxels declared active were therefore less than either the FDR ($n = 3900 \pm 2000$) or Bonferroni ($n = 2200 \pm 1200$) fixed-threshold approaches. The average thresholds were slightly higher for images from

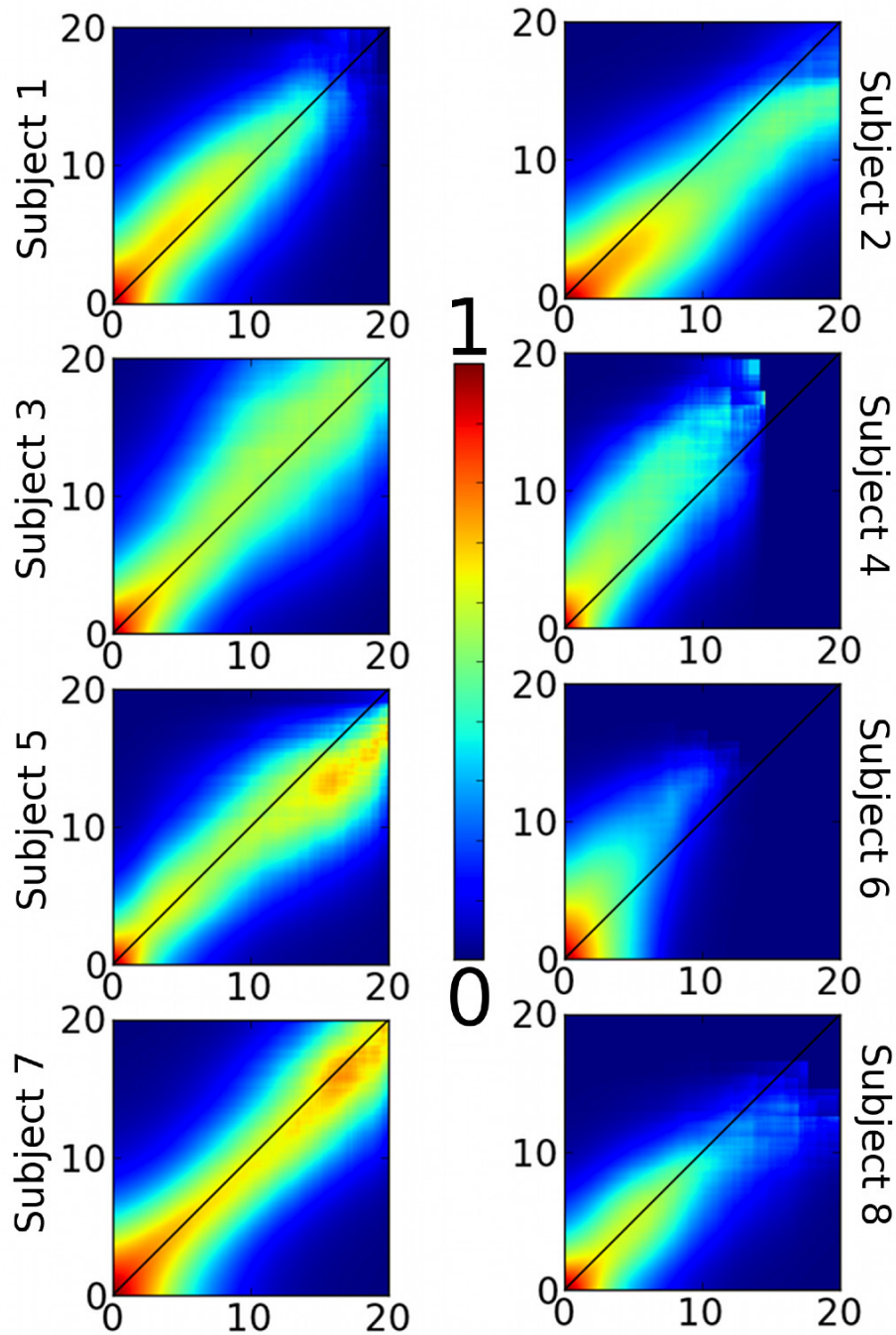


Figure 3.6: Individual rombouts overlap results: The overlap generally decreases with increasing threshold. Subject 6 is identified as having lower reliability than other subjects by inspection of the R_R plots, and subjects 5 and 7 demonstrated the highest overlap coefficients. Several subjects demonstrate local maxima on the R_R plots, although the location of these maxima are highly variable.

the first session ($\bar{t}_{ROC_r,1} = 6.3$) than the second session ($\bar{t}_{ROC_r,2} = 5.9$), however this difference was not significant. No difference was observed for the left and right hand conditions.

Optimal thresholds were additionally determined by finding local maxima in the overlap plots. As not all subjects exhibited local maxima, this was possible in only 11 of 16 cases, as opposed to the 14 of 16 datasets that could be optimized using the ROC-r approach. Additionally, in 6 of 16 datasets, there were multiple local maxima, with 20 local maxima found in total. It was observed that these local maxima were typically at much higher thresholds than the ROC-r optimized thresholds ($\bar{t}_{RR} = 13.5 \pm 5.0$), with only a few occurring at thresholds below $t = 10$. The R_R maxima below $t=10$ were typically similar to the Bonferroni corrected threshold ($n = 4$; $\bar{t} = 5.1 \pm 0.5$).

Demonstrative examples of a) highly reliable data, b) average, and c) poorly reproduced datasets are shown in figures 3.7, 3.8, 3.9, and 3.10. Subject 5 (right hand condition shown in figure 3.7) produced above average reliability by both the Rombouts and ROC-r methods. In this case, there are multiple local maxima in the Rombouts plot, and a clear point of diminishing returns in the AUC. The ROC-r optimized thresholds are just slightly above the Bonferroni level, and near a local maxima in the Rombouts overlap. The additional maxima in the Rombouts overlap occur at much higher thresholds, and produce highly specific maps of the primary motor region (i.e. hand knob). Representative examples of the activation maps produced at these optimized thresholds are shown as well.

Figure 3.8 shows the results from subject 3 for the left hand condition. This dataset is very near to the average by both reliability measures. No clear local maxima in the Rombouts overlap were observed, however the ROC-r method was still able to predict optimal thresholds of $t_1 = 5.6$ and $t_2 = 5.9$. The resulting activation maps produce very high overlap, and identify all key regions identified in the group level. This subject demonstrates that even when no local maxima in the overlap are present, the ROC-r automated thresholds typically lay within the ‘tail’ region of the overlap plot, and thus identify reliable activation patterns.

Figures 3.9 and 3.10 illustrates two of the least reliable datasets obtained in this experiment (subject 4, right hand and subject 2, right hand). It is readily seen from

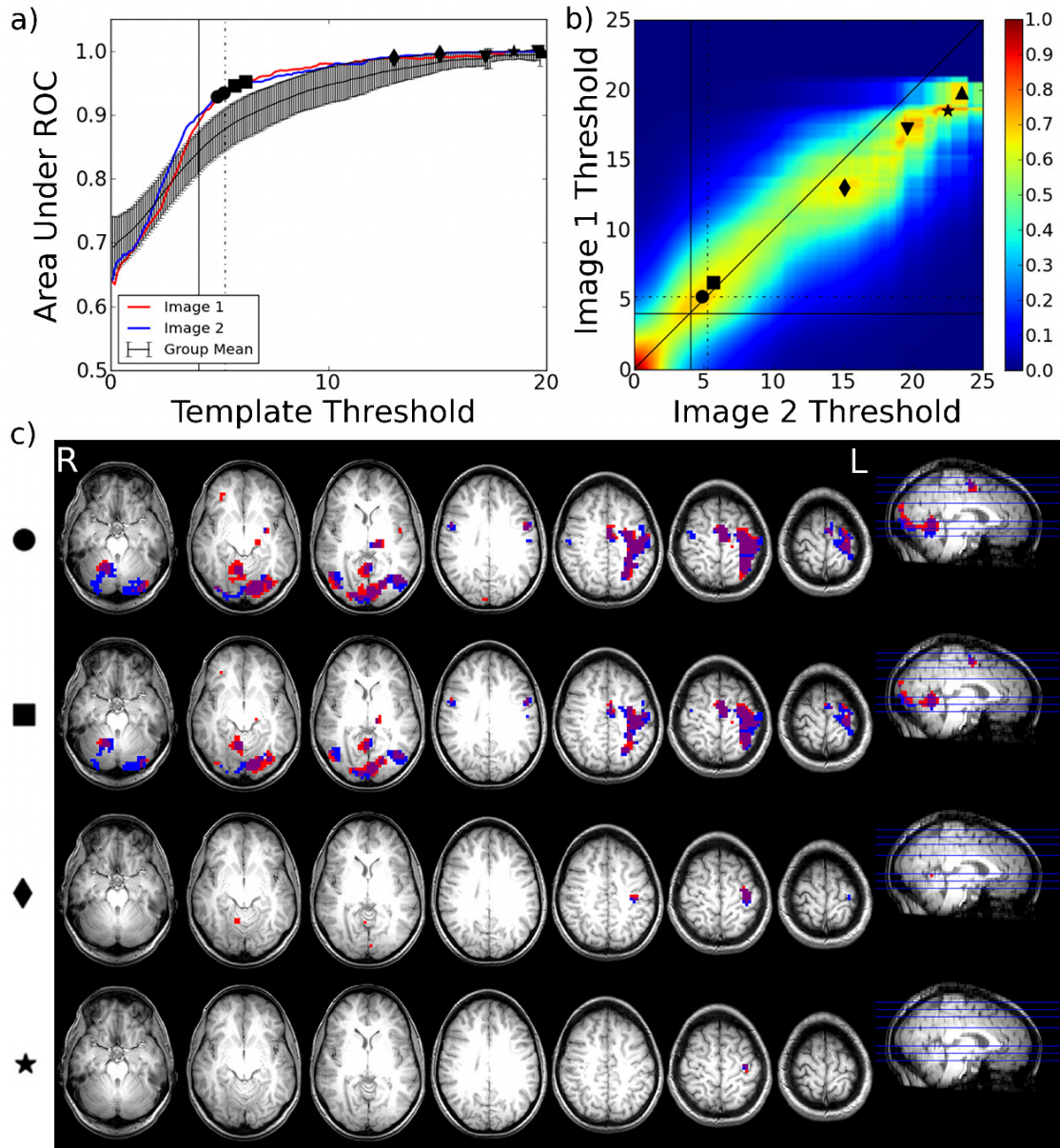


Figure 3.7: Threshold optimization for a highly reliable dataset (subject 5, right hand vs. rest): a) ROC-r AUC, b) Rombouts overlap, and c) thresholded activation maps (red = image 1; blue = image 2; purple = overlap). Squares: ROC-r optimized thresholds; circles, triangles, stars, and diamonds: thresholds for local R_R maxima. FDR corrected ($q \leq 0.01$, solid lines) and Bonferroni corrected ($p \leq 0.01$, dashed lines) thresholds are also shown.

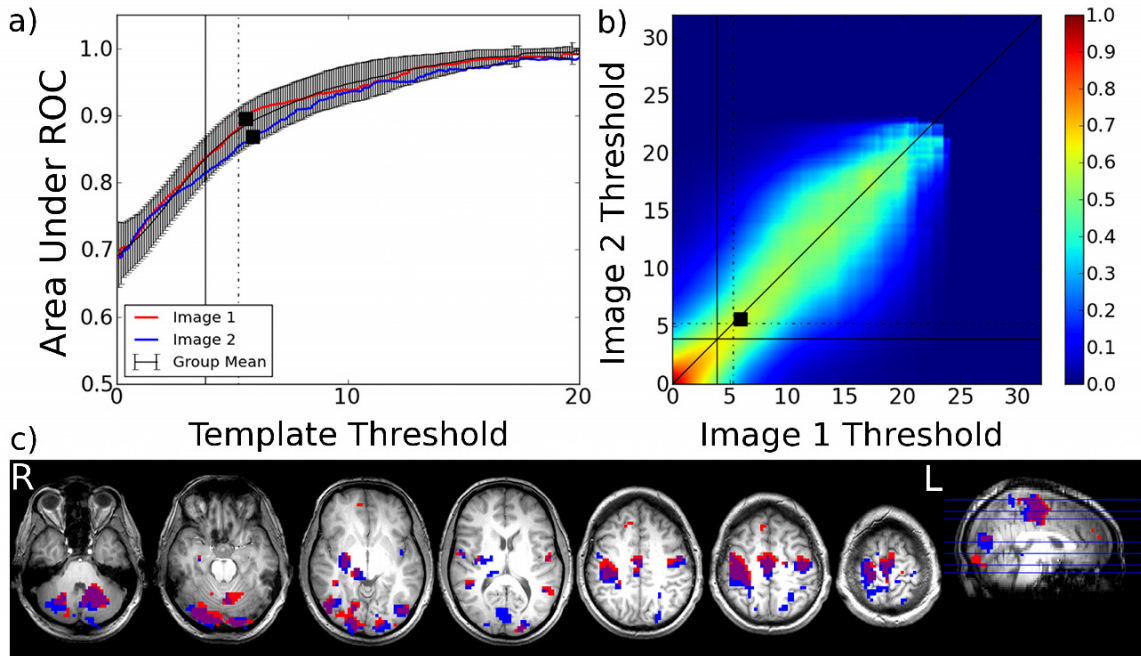


Figure 3.8: Threshold optimization for a moderately reliable dataset (subject 3, left hand vs. rest): a) ROC-r AUC, b) Rombouts overlap, and c) ROC-r thresholded activation maps (red = image 1; blue = image 2; purple = overlap). Squares: ROC-r optimized thresholds. FDR corrected ($q \leq 0.01$, solid lines) and Bonferroni corrected ($p \leq 0.01$, dashed lines) thresholds are also shown.

the Rombouts plot that the optimal thresholds will be different for the two images in both cases. As a result, the use of a fixed-threshold approach results in very poor test-retest reliability. This can also be seen on the ROC-r plots, as the threshold required to achieve the same AUC is different for the two images. However, there are local maxima present in the Rombouts overlap at high thresholds ($t_1 = 18.4$, $t_2 = 13.4$ for subject 4 and $t_1 = 14.8$, $t_2 = 19.3$ for subject 2). Both of these threshold pairs restrict activation to the hand knob of the primary motor region. The ROC-r optimized thresholds produce much lower thresholds in both cases ($t_1 = 7.8$, $t_2 = 4.5$ for subject 4, $t_1 = 3.3$, $t_2 = 5.6$ for subject 2), and include most of the group-level activated regions. Either reliability-based threshold method reduces the test-retest activation extent differences observed with fixed thresholds.

The reliability optimized thresholds were applied to each individual's activation

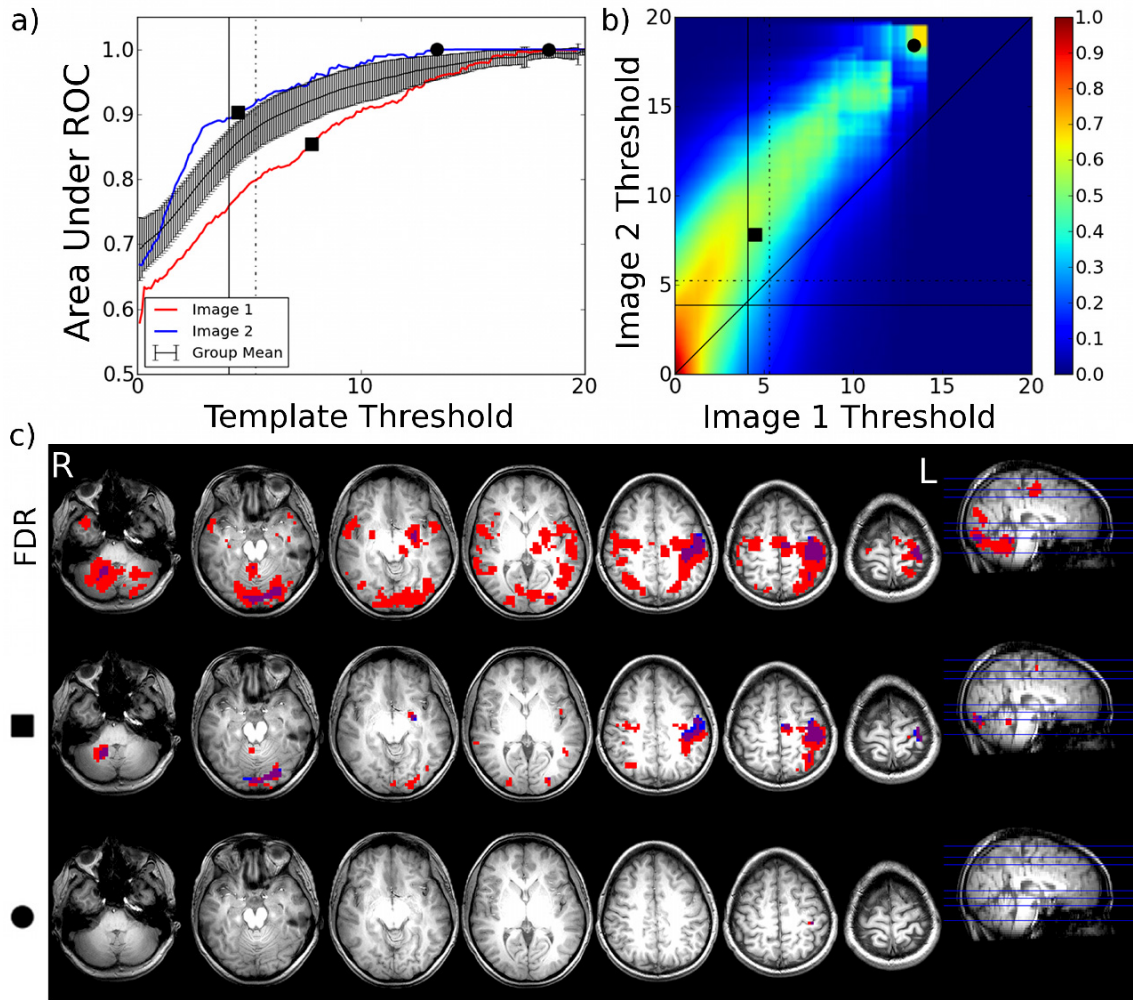


Figure 3.9: Threshold optimization for a low reliability dataset (subject 4, right hand vs. rest): a) ROC-r AUC, b) Rombouts overlap, and c) thresholded activation maps (red = image 1; blue = image 2; purple = overlap). Squares: ROC-r optimized thresholds; circles: thresholds for local R_R maxima. FDR corrected ($q \leq 0.01$, solid lines) and Bonferroni corrected ($p \leq 0.01$, dashed lines) thresholds are also shown. The maximal test-retest overlap occurred for unequal thresholds t_1 and t_2 , so the use of fixed thresholds results in more unreliable activation.

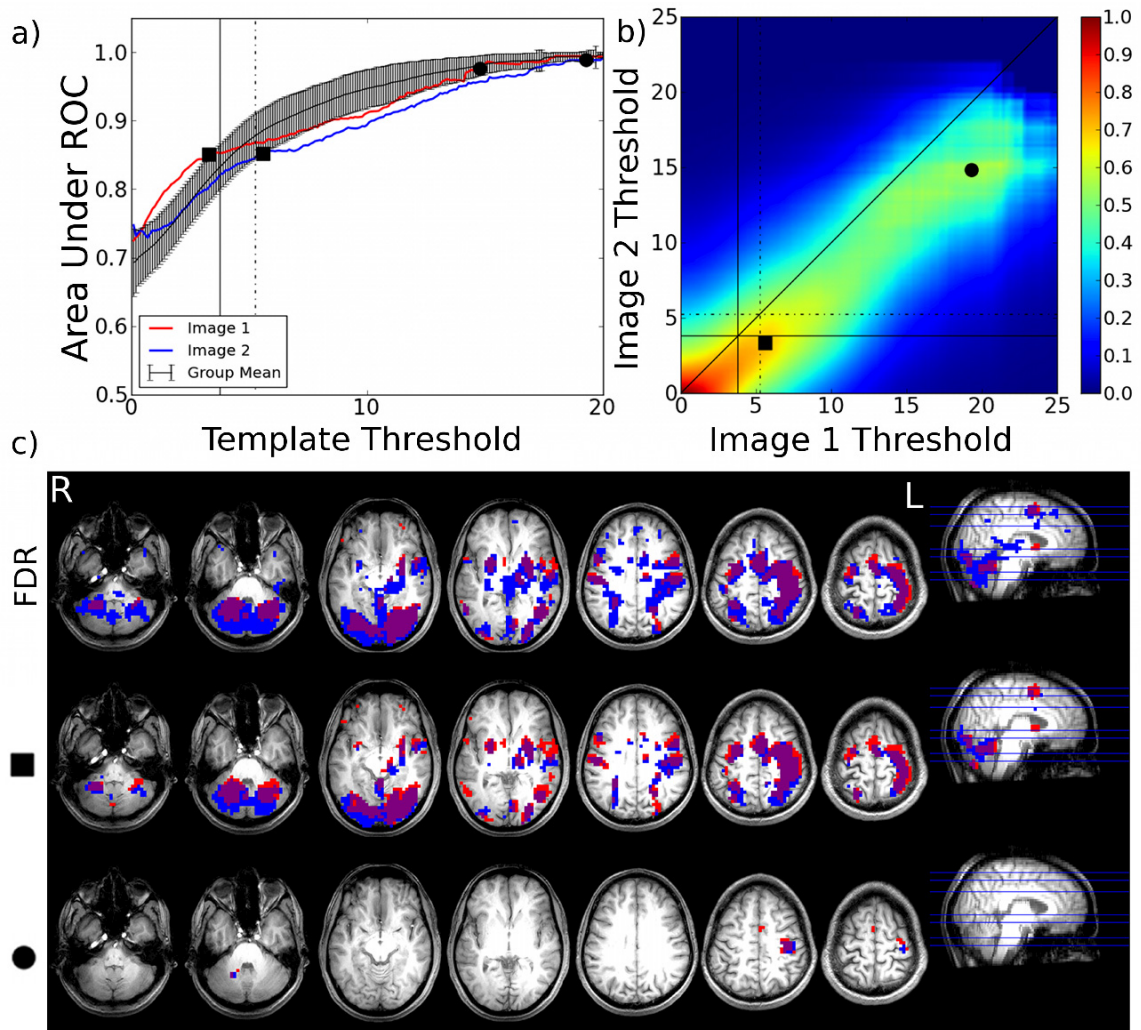


Figure 3.10: Threshold optimization for a low reliability dataset (subject 2, right hand vs. rest): a) ROC-r AUC, b) Rombouts overlap, and c) thresholded activation maps (red = image 1; blue = image 2; purple = overlap). Squares: ROC-r optimized thresholds; circles: thresholds for local R_R maxima. FDR corrected ($q \leq 0.01$, solid lines) and Bonferroni corrected ($p \leq 0.01$, dashed lines) thresholds are also shown. The maximal test-retest overlap occurred for unequal thresholds t_1 and t_2 , so the use of fixed thresholds results in more unreliable activation.

maps, and the results across the group were compared to the traditional group analysis in figure 3.3. The resulting group activation patterns are shown in figure 3.11, displayed as a percent of individuals for whom a given voxel was active. It is clear that in the majority of cases, the ROC-r analysis reproduces activation at the individual level in the key regions identified at the group level. However, activation of the sub-cortical regions observed at the group level, is not reliably present at the individual level. This is due to a combination of some subjects lacking activation in this region, and inconsistent location of these activations when present. The overlap-maximized thresholds typically produced activation in the primary motor region only, with some subjects displaying activation in the cerebellum as well.

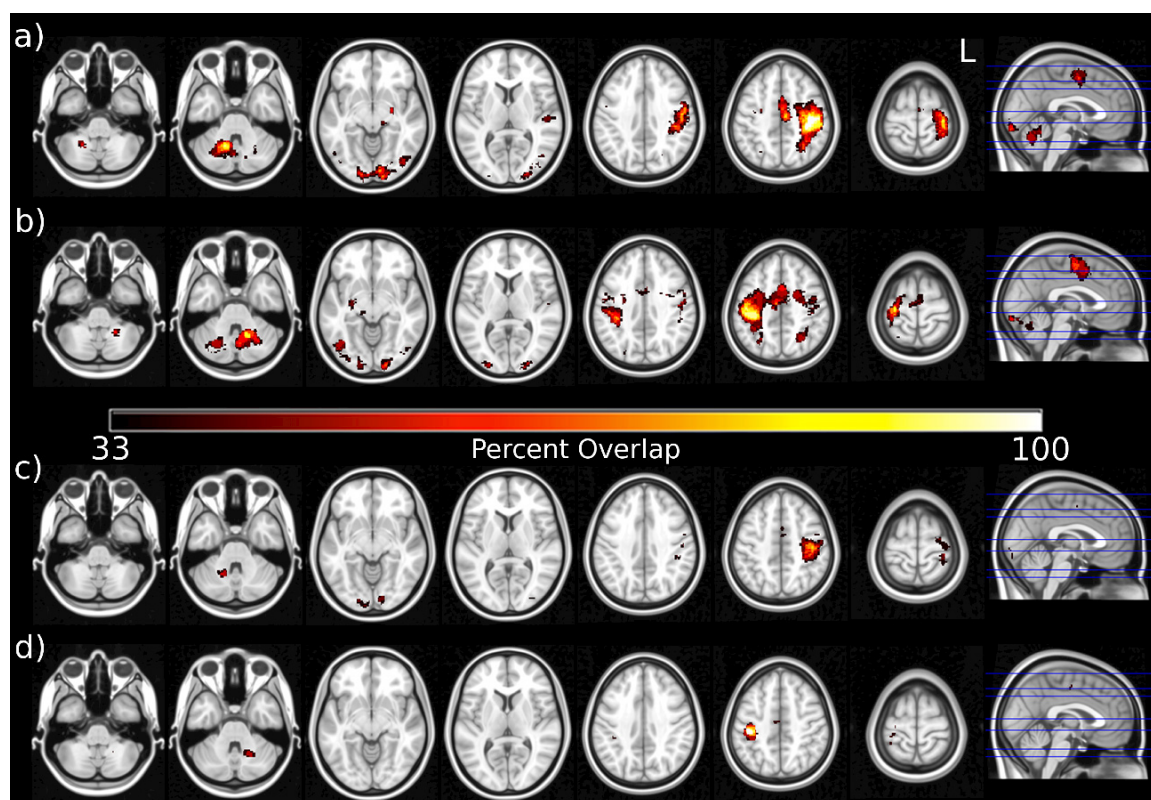


Figure 3.11: Reliability-optimized group fMRI results. Individual images thresholded using the automated ROC-r procedure (a-b) or Rombouts overlap maxima (c-d). Both the right hand (a,c) and left hand (b,d) contrasts to rest are displayed. The color scale corresponds to the percentage of subjects activating each voxel. When multiple local maxima were present, the lowest non-zero threshold was selected for the group map for maximal sensitivity.

3.5.4 Analysis of Poor Datasets

Subject 6 produced unreliable activation maps when compared with the other subjects (see Figures 3.5 and 3.6). We observed that this subject exhibited a large amount of motion, especially during the retest scan, resulting in significant image artifacts. Although standard motion correction (re-alignment) was performed for every subject, this was not sufficient for such large motion events. As the motion time-course for subject 6 was not strongly task-correlated, we attempted to correct for this artifact by using the motion correction parameters as regressors of no interest in the fMRI response model.

The resulting activation maps for subject 6 were much more reliable after inclusion of the motion parameters in the null model. This is evidenced by the Rombouts plot exhibiting an extended ‘tail’ (Figure 3.12c) that was not present using the standard analysis pipeline (Figure 3.12b). Furthermore, the AUC recovered to within or above normal ranges (Figure 3.12a). There was still some discrepancy in the activation magnitude between the first and second scans, which rendered the standard fixed-threshold approaches inappropriate (figure 3.12d). However, using the ROC-r approach we were now able to determine optimal thresholds for this subject, which recovered similar activation patterns to those seen at the group level.

This pre-processing step was not beneficial in all subjects, as low-amplitude motion did not produce noticeable artifact, and when task-correlated, inclusion of these regressors in the null model reduced sensitivity to true activation. Thus at the group level, inclusion of motion regressors cause a modest, but significant ($p < 0.01$), reduction of both the maximum and mean (above threshold, FDR corrected $p < 0.01$) t-statistic values (12% and 5% respectively). Using an FDR or Bonferroni approach to threshold these datasets resulted in a significant reduction of active voxels after motion regression by 32% or 36% respectively. However, the reduction in active voxels decreased to 9% when ROC-reliability based thresholding was used, and was no longer statistically significant ($p > 0.05$). This demonstrates the utility of reliability-based thresholds for mitigating the sensitivity loss that could otherwise occur when using motion regression.

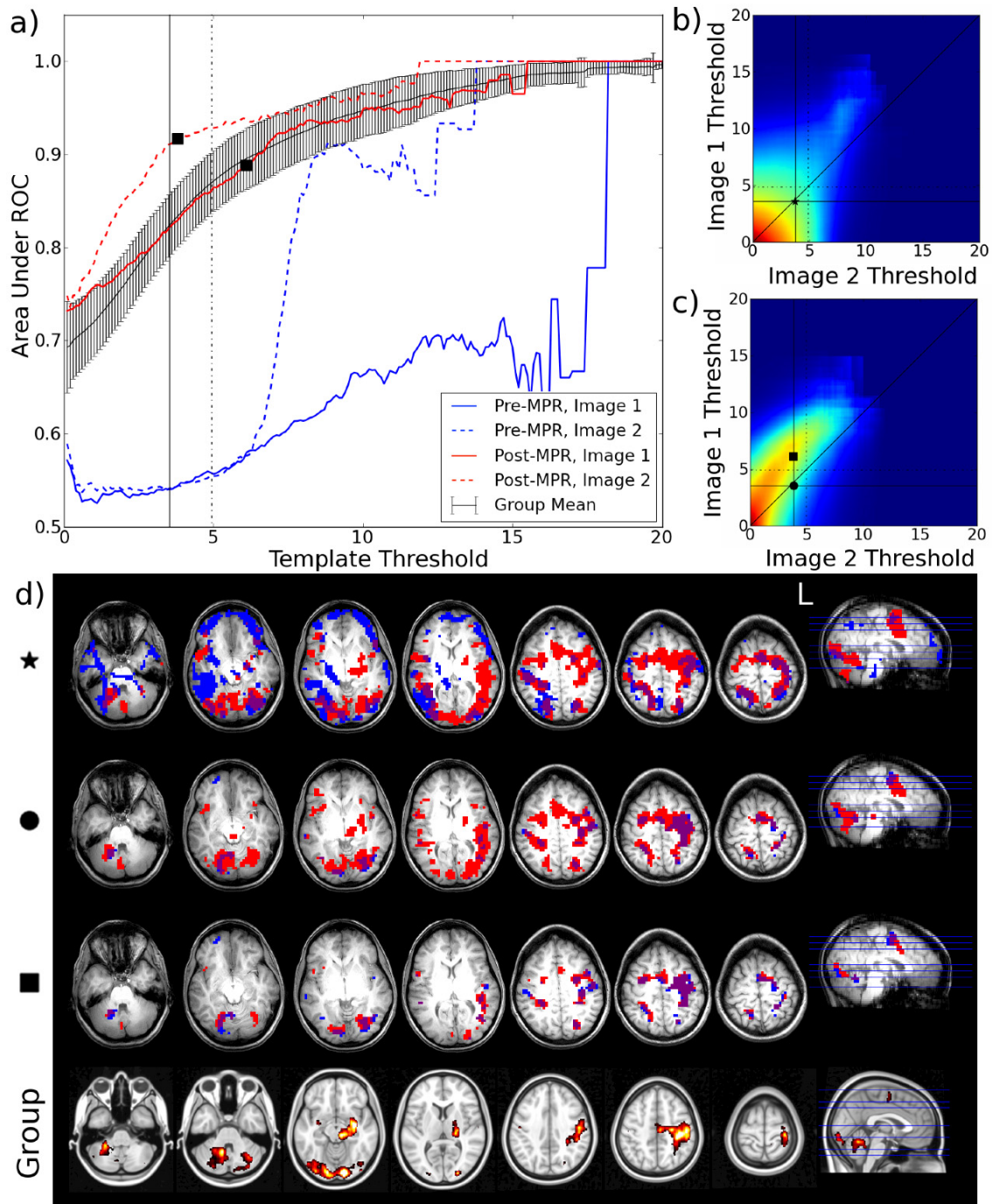


Figure 3.12: Effects of motion parameter regression (MPR) for enhanced reliability of a problematic dataset (subject 6, right hand vs. rest): a) ROC-r AUC with/without MPR, b) R_R without MPR, c) R_R with MPR, d) thresholded activation maps. Squares: ROC-r optimized thresholds; stars: FDR corrected thresholds without MPR; circles: FDR thresholds with MPR. FDR corrected ($q \leq 0.01$, solid lines) and Bonferroni corrected ($p \leq 0.01$, dashed lines) thresholds are also shown. The group map for approximately the same locations is shown for reference.

3.6 Discussion

3.6.1 Group-level Reliability

We have shown that classification reliability varies dramatically with threshold using both overlap and ROC-r approaches. This calls into question the usefulness of using single, fixed thresholds when reporting reliability, an issue that deserves special attention given the lack of a consensus on appropriate threshold strategies. In order to provide a more complete picture of fMRI reliability, reliability should be reported as a continuous function of image thresholds, and these reliability plots should form the basis of comparison between studies. The ROC-r framework is particularly well suited to this task, as quantitative differences between groups (e.g. between patient groups or across multiple pre-processing pipelines) can be assessed using plots of the group mean and standard error. This will ensure that differences in reliability between groups are not simply the result of fortuitous choice of threshold.

3.6.2 Single-subject Reliability

The threshold-reliability relationship we observed was highly individual, and the group-level reliability was a poor predictor of reliability at the individual level. These simple statements have profound implications for adaptation of fMRI as a diagnostic technique. The use of a significance threshold is intended to separate spuriously correlated voxels from those that are truly modulated by the task. However, it has been shown that family-wise error control (i.e. Bonferroni and FDR corrections) does not produce optimal reliability at the group level [120], and it is clear from this work that it will not ensure reliable results at the individual level either. Moreover, even well validated, robust fMRI paradigms are suspect to poorly performing subjects. Issues such as task-related artifact, physiological noise, compliance, and habituation all likely contribute to this problem. It is therefore paramount that test-retest reliability is checked at the individual level for clinical applications.

The finding that the use of a fixed threshold is not optimal for obtaining reliability estimates parallels advances with fMRI lateralization measures. Lateralization indices are known to depend strongly on the significance threshold used, and so several

strategies for incorporating this information have arisen [121,122]. Notably, the generation of laterality vs. threshold curves has become established practice [121,123–125]. These curves have been used to show large variations in lateralization between subjects and tasks [124,126], and have even been used to determine the best threshold to use for calculating laterality indices [121]. We similarly recommend reporting reliability as a function of analysis threshold, in order to avoid drawing conclusions that are threshold-specific. This is especially important when assessing individual subjects, as reliable activation may be overlooked by poor choice of threshold.

In such applications, reliability should be assessed through test-retest imaging, and as a continuous function of image thresholds. Both the Rombouts overlap and ROC-r approaches have relative merits in this context: overlap coefficients are highly intuitive and therefore easily interpreted, whereas the ROC-r approach provides an easier framework for comparing subjects quantitatively, by reducing the results to a 1D plot. Thus for clinical applications, qualitative inspection of the Rombouts overlap plots, followed by a quantitative comparison of individual ROC-r plots to a normative group mean is ideal. The latter is similar to the approach taken by Abbott *et al.* [124] to separate typical from atypical lateralization curves. Practically speaking, this requires a pilot group be employed to establish normative reliability-threshold plots (i.e. means and standard deviations) for a given task/scanner. Ideally this is already being done prior to any clinical fMRI studies.

3.6.3 Threshold Optimization

One of the primary aims of our study was to investigate means of using reliability to determine optimal thresholds for individual fMRI studies. Several authors have independently concluded that reproducibility of fMRI results could provide meaningful insights for active voxel identification [91,117,127]. From the outset, the potential of these methods for optimizing threshold selection has been identified [88]. Meanwhile other studies have used a mixture-model approach to determine adaptive thresholds, and then used overlap reliability plots as a standard to assess their results [80]. The data-driven methods used in this work may have advantages in this context to model-based approaches, especially when the input images do not conform to the assumptions of these models (e.g. presence of artifacts, scanning order effects, physiological

noise).

The most obvious caveat to reliability-based threshold optimization method is that it requires at least somewhat reliable input data in order to produce meaningful threshold estimates. It is clear that this will not always be the case, as a variety of factors will impact the fMRI reliability (e.g. compliance, scanner stability, movement, etc.). However outlying datasets are easily identified (Figures 3.5 and 3.6), and optimal pre-processing settings can be determined on a subject-by-subject basis (Figure 3.12). One potential limitation of these methods is the possibility of persistent artifacts across test-retest sessions being interpreted as reliable activation. Edge-artifacts associated with task-correlated head motion may be particularly problematic in this regard, warranting caution when analyzing tasks that induce significant head motion. For this reason, we explored motion regression for the elimination of motion artifacts. In general, motion regression decreased fMRI sensitivity in the presence of task-correlated motion. However, the loss in sensitivity was greatly diminished using reliability-based thresholds, suggesting that the same areas were reliably detected, albeit at lower thresholds.

While pre-processing strategies, such as motion regression, may help with specific artifacts, in order to obtain the best results, general strategies that maximize test-retest reliability should be adopted in the experimental design. For example, for well-learned tasks such as simple motor movements, it has been shown that reliability within sessions is higher than between sessions [128]. For higher cognitive functions, more complicated task repetition effects may need to be taken into account [129,130]. In the clinical setting, it is typically more reasonable to perform single-session test-retest experiments than to ask patients to return for multiple scanning sessions, which should result in slightly higher reliability estimates.

As other research groups have illustrated, ROC estimation is improved by collecting more test-retest replications [88,108,113]. However, the extra imaging required will need to be traded off against running fewer tasks per subject or fewer subjects for the same amount of scanner time. In the ROC-r framework, the collection of more test-retest datasets may be used to form more accurate template maps, for instance by averaging together individual runs [84]. When session time must be kept to an absolute minimum (i.e. no test-retest is available), a compromise to individual level

optimization may be necessary. For example, a pilot group activation map may be used to optimize subsequent individual-level maps using the ROC-r framework.

We explored two reliability-based thresholding strategies. In the first, thresholds were chosen from the Rombouts plots using local maxima of the test-retest overlap, which are easily interpreted as providing maximal overlap of the test-retest images. In the second, AUC plots were optimized by balancing test-retest accuracy (i.e. AUC), against the diminishing returns observed at high thresholds. This approach produced a better balance between sensitivity and specificity than the overlap-maximization approach, which tended to result in very limited activation extent. The overlap-maximization approach may thus be suitable when very high specificity is desired (e.g. to isolate the primary motor cortex), however this method was possible in fewer subjects than ROC-r based optimization.

On average, the ROC-r determined thresholds were more conservative than traditional fixed-threshold approaches of the FDR or Bonferroni corrections. This is in contrast with the findings of Thirion *et al.* at the group level that reliability optimized thresholds were somewhat lower than either of the fixed error rate correction schemes [120]. However, our method allows for tuning of the optimization parameters (i.e. AUC and AUC' cutoffs) to alter the sensitivity/specificity tradeoffs. The best optimization strategy will thus depend on the target application, and the particular risks associated with false positive or negative results. Ultimately, the advantage of these methods is the extra confidence obtained through reliability optimization, which will be particularly advantageous in clinical settings.

3.7 Conclusion

There is mounting evidence for moving beyond strict interpretation of p-values for significance of fMRI results [80, 88, 91, 131, 132]. These studies suggest that reliability of activation may be more informative than activation magnitude alone. With this in mind, we developed data-driven methods for evaluating the reliability-threshold relationship. Critically, we demonstrated automated procedures for producing robust activation maps by optimization of individual thresholds. These thresholds were shown to reliably identify critical task-related regions at the single subject level. We also showed that whereas fixed threshold approaches resulted in loss of sensitivity with

motion regression enabled, reliability-based thresholding mitigated the differences in activation extent with or without motion regression. The ability to produce activation maps using an entirely automated analysis pipeline is an important advance for fMRI. We expect these methods to be especially useful wherever individual level analyses are conducted, such as in clinical, diagnostic, and assessment applications.

Chapter 4

Manuscript 2: Fully Automated Quality Assurance and Localization of Volumetric MEG for Potential use in Pre-Surgical Mapping

Authors: Tynan Stevens, Tim Bardouille, Gerhard Stroink, Shaun Boe, Steven Beyea.

Status: Submitted (under review)

Journal: Journal of Clinical Neurophysiology

Contribution: Conceptualization, Data Analysis, Primary Author

4.1 Motivation

One of the strengths of ROC-r analysis for functional mapping is the use of minimal assumptions about the underlying data distributions. Because of this, ROC-r is equally well suited for quality assurance and automated processing of volumetric MEG source images. In this manuscript, we therefore use a very well known stimulation paradigm for MEG (median nerve stimulation), and show that the quality assurance and localization provided by ROC-r analysis of volumetric MEG maps parallels that offered for more traditional equivalent current dipole (point source) mapping methods. The introduction of a quality assurance metric for volumetric MEG images provides a critical tool that was previously unavailable.

Median nerve stimulation (MNS) is a well known MEG mapping paradigm, which uses peripheral electrical stimulation to evoke a controlled sensory response. The sensory evoked field (SEF) response to MNS has been shown to peak at at least three distinct latencies: the N20m, P35m, and P60m [133]. Most clinical studies have focussed on the N20 [23,29,134], however the P35 and P60 are typically stronger, and therefore easier to detect [133,135]. A recent study of tumor and epilepsy patients using MNS found that the strongest SEF occurred at an average latency of 56 ms [136]. This study also reported a large degree of between-subject variability in the latency

of peak SEF response (22-162 ms). In this study, we will use ROC-r to automatically identify the location of the P35m source.

The only requirement to perform a ROC-r analysis is the availability of at least two estimates of the activation map. However, this manuscript uses ROC-r without performing explicit test-retest imaging. Instead, we take advantage of the typical MEG experimental design, which consists of many independent units (epochs), which can be straight-forwardly divided into independent split-halves. We use these split-halves to form pseudo test-retest datasets. A similar approach can be taken for fMRI mapping, although more care must be taken in the generation of split-half maps, as fMRI does not have the discrete sub-units of MEG because of the long HRF. Nonetheless, single-run ROC-r has the obvious benefit of not requiring repeated imaging during the scanning session. This is especially important in clinical settings, as patients may fatigue quickly, and in pediatric populations, as children are not typically able to sit still for long periods of time. Furthermore, single-run ROC-r avoids the potential errors introduced by co-registration, and can produce large samples of pseudo test-retest images, paradoxically allowing us to calculate more accurate ROC-reliability estimates.

In this work, MEG mapping is performed using beamformer inverse solutions. As beamformers are dipole scanning techniques, there are some subtleties to the interpretation of these maps that must be considered. The most crucial caveat is that beamformer spatial extent can not be interpreted as the spatial extent of the underlying sources - indeed spatial resolution is proportional to SNR for MEG beamformers [137]. Therefore, strictly speaking, only the peaks (i.e. local maxima) of beamformer clusters should be relied on for localization. Nonetheless, there are many low-amplitude local maxima which are simply the result of measurement noise, and are highly unreliable in their spatial configuration. Thus ROC-r can still be used to determine: a) if there are reliably localized MEG sources in the beamformer map (i.e. to assess data quality), and b) what threshold should be used to distinguish the reliable and unreliable peaks in the MEG source map. Respecting the caveats described above, only the peaks of the reliable clusters should be utilized for localization.

4.2 Abstract

This paper demonstrates an automated procedure for both quality assurance and data-driven thresholding of volumetric MEG images using receiver operating characteristic reliability (ROC-r). These methods are ideally suited for presurgical mapping, where repeatability and spatial accuracy are crucial. To demonstrate ROC-r, somatosensory evoked fields (SEFs) were mapped in 18 healthy subjects using bilateral median nerve stimulation (MNS). Equivalent current dipole (ECD) and beamformer inverse solutions were calculated. The ROC-r reliable fraction (F_R) was compared to the ECD goodness-of-fit (GoF) for use as a quality assurance parameter. The peak locations and latencies of clusters defined by ROC-r thresholds were compared to the ECD for co-localization accuracy. The predominant component of the SEF response occurred around 35 ms, contralateral to the MNS. The ROC-r reliable fraction and ECD GoF were highly correlated (mean 0.66; 95% CI 0.32-0.85). There was no difference in the latency of the peak GoF (35.0 ± 0.6 ms) and F_R (35.5 ± 0.8 ms). The ECD fits and ROC-r peaks co-localized to within a mean (median) distance of 8.3 ± 5.9 mm (6.2 mm). ROC-r analysis of volumetric source maps provides automated quality assurance capabilities, comparable to those offered by GoF for ECD modelling. Furthermore, ROC-r thresholding was shown to co-localize closely to the gold standard of ECD. This analysis can be added to any whole-brain MEG source imaging, and is especially useful for pre-surgical mapping, providing automated localization with built-in quality assurance. The development of a ROC-r analogue to GoF for beamformer imaging is a critical improvement to volumetric source mapping for clinical applications.

4.3 Introduction

Pre-surgical mapping with magnetoencephalography (MEG) localizes functional neuroanatomy based on relatively direct measurements of cortical electrical activity. Among the most successful applications of MEG to pre-surgical mapping is localization of the somatosensory cortex [18]. The most ubiquitous paradigms are median nerve stimulation (MNS) [23, 29], vibrotactile stimulation [138], and pneumatic stimulation [28], all of which elicit sensory evoked fields (SEF) from the contralateral

primary somatosensory cortex. MNS is also used intra-operatively to map the central sulcus via phase reversal of surface electrocorticography [23].

Most localization studies use the equivalent current dipole (ECD) model [133, 135, 139], which has been validated in a number of pre-surgical mapping studies [18, 23, 29, 134, 136]. The ECD model is attractive because of its simplicity and well-defined goodness-of-fit (GoF) parameter for quality assurance (i.e. the percent of the sensor variance explained by a single dipolar source). It is common to see GoF as a criterion for selecting dipoles in pre-surgical mapping with ECD [134]. However, the validity of the ECD model is suspect for distributed cortical activity or multiple cortical sources with more complicated evoked fields. Models using multiple dipoles are available, but require *a priori* specification of the number of dipoles. This makes them challenging for clinical practice due mainly to poor inter-rater reliability.

More recently, studies have used volumetric source models to overcome limitations of the ECD model [30, 31, 33, 74–76, 140]. Volumetric source models like beamformers generate whole-brain source maps capable of describing multiple or distributed cortical sources, alleviating the need to specify the number of dipoles. Despite increasing use in pre-surgical mapping, there is no established method for quality assurance of volumetric source models. Additionally, thresholding of single-subject maps is often based on *a priori* expectations for the clinically relevant activation patterns, undermining improvements in inter-rater reliability achieved by moving away from ECD models. A method to assess the quality of volumetric source maps and determine appropriate threshold levels is needed.

We have thus developed methods for quality assurance and automated thresholding of volumetric MEG source maps to improve the reproducibility of the source modelling process. Our approach uses a receiver operating characteristic reliability (ROC-r) framework previously demonstrated for fMRI mapping [141]. The advantages of ROC-r are two-fold. Firstly, ROC-r provides quantitative measures of source map reliability, increasing confidence in localization results. Secondly, ROC-r identifies optimal data-driven thresholds, facilitating push-button processing of volumetric source maps. This reduces the reliance on *ad hoc* thresholding and decreases inter-rater variability. The addition of ROC-r analysis to whole-brain MEG mapping enhances pre-surgical mapping capabilities.

In this study, we validate the ROC-r method for the case of beamformer mapping of the MNS SEF, by means of a comparison to the well established ECD model. The MNS paradigm makes an ideal test case as it generally provides robust localization of the early SEF response in single subjects. We will show that ROC-r provides quality assurance metrics for whole-brain MEG mapping analogous to the GoF of the ECD model. Furthermore, we will show that ROC-r automated thresholds identify brain areas well-matched to those determined using ECD. These findings establish the utility of ROC-r for pre-surgical MEG mapping, by introducing quantitative measures of data quality and automated methods for detecting significant areas of activity.

4.4 Methods

4.4.1 Data Collection

Eighteen healthy volunteers participated in this study (10 females; age 19-29, mean 24 years). The study was approved by the local ethics board, and subjects provided informed consent. Each participant received an MEG scan during which the somatosensory cortices were localized using bilateral MNS. Head position indicator coils placed on both the left and right temples and mastoids monitored head position throughout the MEG scan. The nasion, left/right pre-auriculars, and scalp surface were digitized for source modelling. Electro-oculargraphy (EOG) electrodes were placed above and below the left eye and lateral to each eye for the removal of artifacts. MEG and EOG data were collected at 1000 Hz sampling frequency, with an in-line 0.1-330 Hz filter using a whole-head 306 channel Neuromag system (Elekta AB, Stockholm, SE).

4.4.2 MNS Paradigm

Both primary somatosensory cortices were mapped using bilateral MNS. Motor thresholds were determined by applying supra-threshold stimulation, and reducing the stimulation strength until thumb twitches were no longer discernible. Sub-threshold stimulation was delivered in single 0.5 ms pulses 1-2 s apart. Eighty to one-hundred stimuli were applied to each side in random order.

4.4.3 Data Pre-processing

MEG data were pre-processed to create the SEF responses to left and right MNS. Following environmental noise reduction with temporal signal space separation [142], a low-pass filter was applied (70 Hz), and data were down-sampled to 250 Hz. Independent component analysis was performed to remove components correlated with the EOG signals. The data were segmented into epochs relative to the left or right MNS onset ($-200 < t < 200$ ms), and baseline corrected for the -100 to 0 ms period. The epoched MEG data were averaged for left and right MNS separately to generate SEF responses.

4.4.4 Source Localization

ECD Modelling

Source localization using the ECD model was achieved using the xfit software (Elekta AB, Stockholm, SE). A spherical model was employed based on the head shape collected prior to MEG acquisition. At each time-point in the SEF, the location, orientation, and strength of the single dipole that provided the best GoF was determined. The latency of the peak GoF nearest to the P35m was identified, and the location at this latency defined the localization of primary somatosensory cortex.

Beamformer Mapping

Volumetric source mapping was performed using the beamformer spatial filter method on the epoched MEG data. The epochs were divided into split-halves prior to computing a dynamic beamformer (Elekta AB, Stockholm, SE), to facilitate subsequent ROC-r analysis (i.e. half of the trials were randomly selected to form one beamformer map, and the remaining half for a second beamformer). The dynamic beamformer produced whole brain activation maps for each time-point of the SEF. For each location in the brain, the dipole direction was chosen to maximize source power, and the pseudo-z statistic was calculated by taking the ratio of the source power to the projected noise covariance at that same location. Covariances were calculated from each split-half evoked response for the -200 to 0 ms (baseline) period, and the 0 to 200 ms (active) period. The beamformer forward solution was calculated using the

same spherical model employed for ECD localization. Independent spatial maps were calculated for left and right MNS, and for each split-half of the data. This process was repeated for 8 different randomized split-halves, generating sixteen SEF maps (i.e. 8 split-half pairs) for each participant and each side of stimulation. A final source map for each participant/side was obtained by averaging the 16 split-half maps.

4.4.5 Anatomical Template

The MNI152 template MRI [143] was used as an anatomical frame of reference for localization. The Isotrak head digitization was manually registered to the MNI head shape using a translation and rotation transformation. Applying this transformation to the MNI152 template produced an anatomical image in the individuals' head coordinates. This was used to interpret dipole locations, and to construct the beamformer source grids. The template brain was down-sampled to 4 mm to provide a reasonable source grid resolution. Beamformer source estimates were produced for each voxel in this grid.

4.4.6 Quality Assurance Analysis

Beamformer reliability was assessed using ROC-r (see Stevens *et al.*, 2013 for more details [141]), and compared to the ECD GoF. The ROC-r algorithm takes as input two source maps, and outputs the ROC area under the curve (AUC) as a function of threshold for each map. Overall reliability of the source maps is summarized using the reliable-fraction (F_R), which is the fraction of the threshold range for which the AUC is above its mid-range (Figure 4.1). High F_R indicates that reliability increases quickly with increasing threshold, and remains high for a large range of thresholds.

Reliability was assessed for each time point from -200 to 200 ms, using each split-half map pair as ROC-r inputs (i.e. each split-half produces two source maps, and these can be used to generate a ROC-r analysis). The F_R was then averaged across the 8 split-half pairs, producing a time-dependent estimate of the beamformer reliability for each subject/hand. The mean and variance of the F_R was compared to the GoF for the baseline and active periods, and the time courses of the F_R and GoF were compared via the correlation coefficient to demonstrate validity of the F_R metric. The latency of the peak F_R nearest to the P35m was also identified, and compared

to the latency of the peak GoF via a paired t-test to ensure both methods identified the same evoked response.

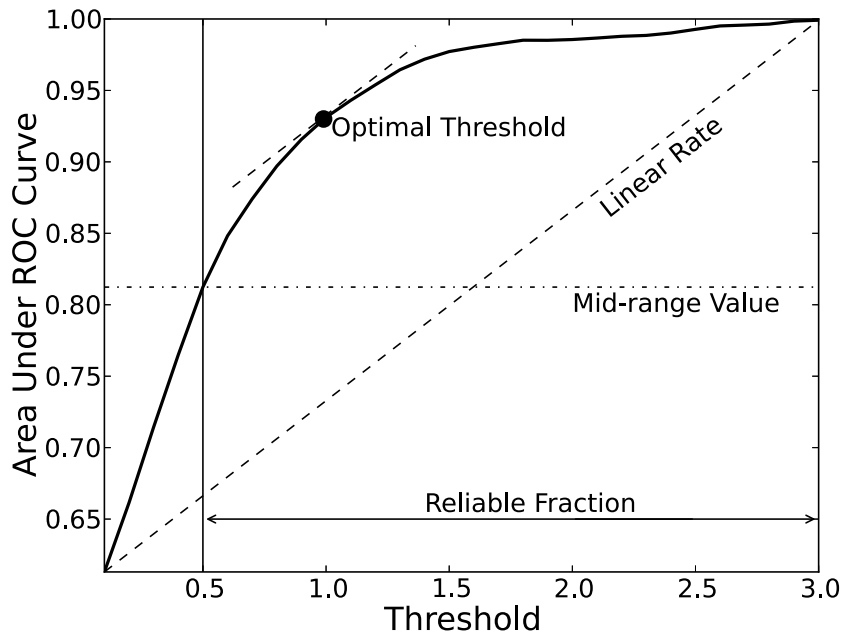


Figure 4.1: Diagram of the ROC-r output. The thick solid line shows the ROC area under the curve as a function of image threshold. The mid-range value (dash-dotted line), and the ‘linear rate’ (dashed line) are shown. The reliable fraction is the fraction of the threshold range for which the AUC is above the mid-range value (i.e. $F_R = 2.5/3.0 = 0.833$). The optimal threshold is the lowest threshold for which the AUC is above the mid-range value and the slope is equal to or less than the linear rate.

4.4.7 ROC-r Thresholding

ROC-r was also used to compute thresholds to identify clusters of significant activity in the beamformer maps. First, beamformer maps were extracted from 24 to 44 ms to capture the 35 ms peak. Each split-half pair was submitted to ROC-r analysis, resulting in 8 pairs of AUC versus threshold curves. Optimal thresholds were determined as the lowest threshold for which the AUC was above mid-range, and the AUC rate of change dropped below the ‘linear rate’ ($[AUC_{max} - AUC_{min}] / [t_{max} - t_{min}]$, see Figure 4.1), providing a balance between high reliability and high sensitivity. Finally, the average ROC-r threshold across the 16 AUC curves was applied to the average

beamformer map.

4.4.8 Localization Comparison

ROC-r beamformer localizations were validated by comparison with ECD locations. Thus for each thresholded beamformer map, activation was divided into contiguous clusters (i.e. adjacent voxels in space or time), and the largest cluster was identified. The peak location and latency of the largest cluster was extracted and compared to the ECD location at the same latency. Co-localization accuracy was measured as the euclidean distance between the two locations. Distances and displacements in the left/right, anterior/posterior, and superior/inferior directions were also calculated. Finally, we examined the relationship between data quality (GoF/F_R) and co-localization accuracy to investigate possible sources of co-localization error.

4.5 Results

4.5.1 Sensory Evoked Fields

SEF responses to median nerve stimulation were detected from the contralateral hemisphere of all subjects. Figure 4.2 shows the group averaged SEFs. The first SEF peak occurred at stimulus onset - an artifact of the electrical stimulation. A small 20 ms peak (N20m) was observed in the group average, but was not detectable in all individual subjects. The 35 ms peak (P35m) was the most prominent deflection, and was easily discernible in most subjects. Later responses (50-120 ms) of similar magnitude to the P35m were common, although exact latencies were subject-specific. The group level sensor topographies shown in Figure 4.2 were consistent with contralateral dipolar sources from 20 to 120 ms.

4.5.2 Beamformer Reliability and Quality Assurance

ROC-r successfully measured reliability of the beamformer source maps in all subjects. Representative F_R and GoF time-courses are shown in Figure 4.3. Both F_R and GoF were lower during the baseline period (0.10 ± 0.04 and 0.37 ± 0.14 respectively) than from 20-120 ms post-stimulus (0.53 ± 0.25 and 0.68 ± 0.19). The change in quality scores between the baseline and active periods was larger for F_R (factor of

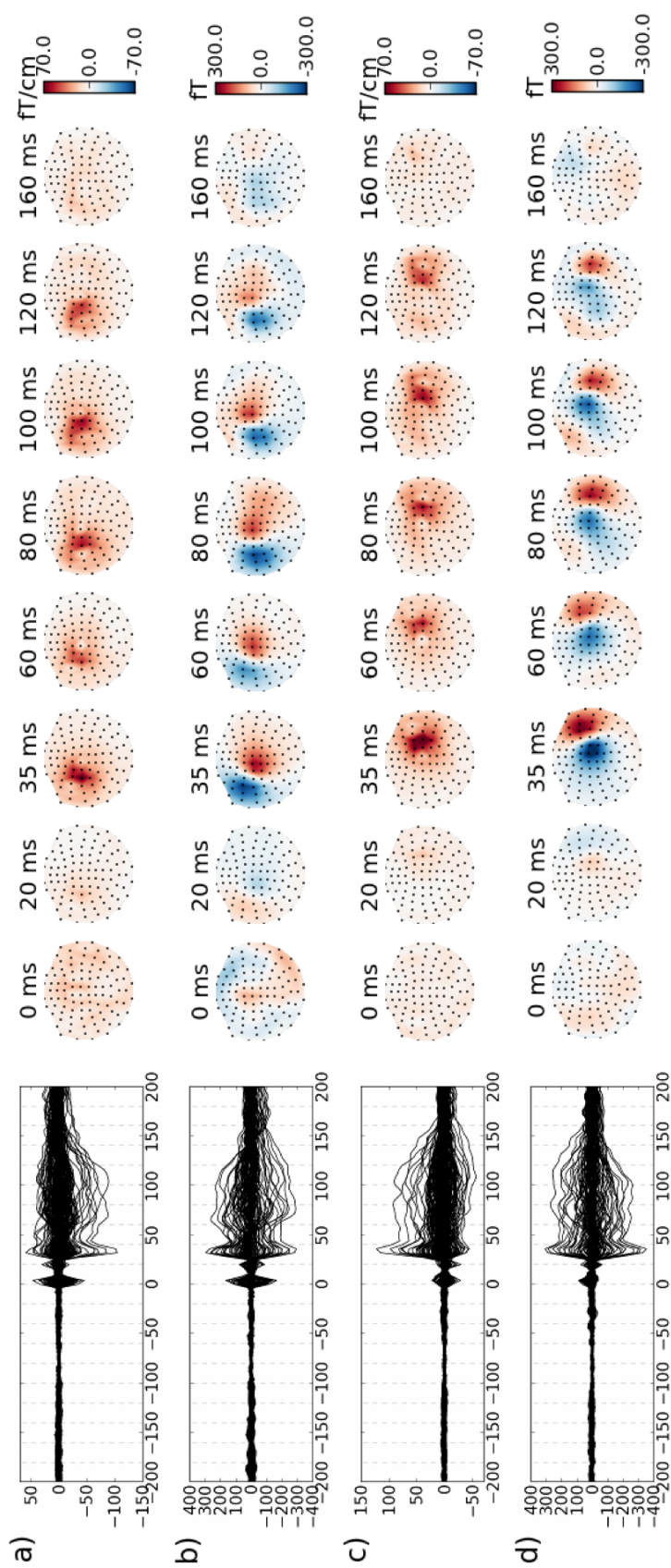


Figure 4.2: Butterfly plots (left) and sensory topographies (right) of the group average SEF to median nerve stimulation: a) right median nerve, gradiometers; b) right median nerve, magnetometers; c) left median nerve, gradiometers; d) left median nerve, magnetometers. A dipolar field pattern contralateral to the MNS side is observable from 20-120 ms post-stimulus, peaking around 35 ms.

5.3) than GoF (factor of 1.8), indicating that the ROC-r measure of data quality is more sensitive than GoF. Variance of the F_R was significantly less than GoF during baseline. The ROC-r F_R exhibited a peak at the time of stimulation, as the electrical stimulation device produced a reliable field pattern on the sensors, which in turn produces a characteristic beamformer solution. This field pattern was not well described by a single equivalent dipole, and thus the dipole GoF was low despite the F_R peak.

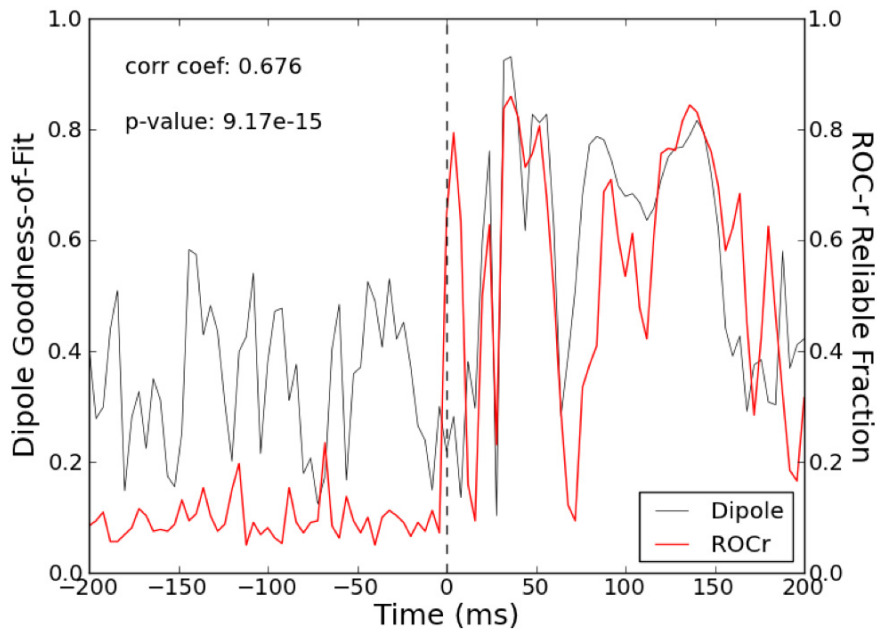


Figure 4.3: Dipole goodness-of-fit and ROC-r reliable-fraction over time for a representative subject. The mean and variance of the GoF during the baseline period (-200 to 0 ms) is higher than the F_R . The peak values and latencies of F_R are similar to those of the GoF, with the exception of the stimulus artifact. Overall there is a high correlation between the GoF and F_R , indicating that ROC-r F_R provides a successful analogue to GoF for quality assurance of beamformer source maps.

Across the group, ROC-r and ECD modelling identified the same latency for the P35m ($t_{ROC-r} = 35.5 \pm 0.8$ ms, $t_{ECD} = 35.0 \pm 0.6$ ms; $p = 0.46$). There was significant correlation between the F_R and GoF time-courses, indicating that the ROC-r quality assurance metric parallels the information provided by ECD GoF. The mean correlation coefficient between the F_R and GoF was 0.66 (95% CI: 0.32-0.85). Table 4.1 shows the correlation between F_R and GoF for each dataset.

Table 4.1: Correlation between ROC-r F_R and ECD GoF by subject and side of median nerve stimulation. The difference between the left and right MNS correlation was not significant. The range of correlations was substantial (0.388-0.864), but in all cases the correlation was statistically significant at $p < 0.001$.

Subject	Left	Right
1	0.641	0.700
2	0.542	0.584
3	0.766	0.533
4	0.393	0.670
5	0.745	0.655
6	0.815	0.692
7	0.582	0.531
8	0.519	0.598
9	0.676	0.686
10	0.458	0.645
11	0.388	0.558
12	0.695	0.738
13	0.787	0.677
14	0.613	0.774
15	0.414	0.474
16	0.431	0.793
17	0.864	0.811
18	0.718	0.829
Average	0.639	0.676

4.5.3 Source Localization and Thresholding

ECD localization between 24 and 44 ms was possible in 33/36 MNS datasets. ROC-r thresholds ranged from a pseudo-z of 0.56 to 1.34, with a mean of 0.92 ± 0.19 , identifying significant clusters for 32/36 datasets. Seven of the beamformer maps contained multiple clusters in the selected latency window. Datasets for which either method failed to achieve localization (i.e. no beamformer clusters were identified, or no dipole fit was possible) were excluded from co-localization analysis, resulting in 31 ECD and ROC-r beamformer peak comparisons.

Typical ECD and beamformer localizations are shown in Figure 4.4. The mean dipole to beamformer peak distance was 8.3 ± 5.9 mm. The distribution was skewed by a few datasets with large (> 15 mm) separation between the dipoles and beamformer peaks (Figure 4.5), rendering the median (6.2 mm) more representative of typical co-localization (e.g. Figure 4.4b). Dipole locations were frequently within the boundaries of the ROC-r beamformer clusters, but sometimes localized between multiple beamformer clusters (e.g. Figure 4.4a).

The mean distance between the ECD and beamformer locations was greatest in the left/right (4.6 ± 0.8 mm), followed by anterior/posterior (4.3 ± 0.6 mm), and then the superior/inferior directions (3.2 ± 0.6 mm). Displacement in the left/right and anterior/posterior directions did not differ significantly from zero (0.5 ± 1.1 mm and 0.1 ± 1.0 mm respectively). However, the beamformer peaks were displaced significantly in the superior direction compared to the ECD locations (2.1 ± 0.7 mm; $p = 0.008$).

Co-localization accuracy tended to be better for datasets with higher GoF and F_R , indicating that higher quality data were more likely to produce consistent localization results. F_R explained more variance in the dipole to beamformer distance ($R = -0.612$) than GoF ($R = -0.591$), but both were significant predictors of accuracy (Figure 4.6).

4.6 Discussion

We demonstrated ROC-r analysis for quality assurance and automated thresholding of beamformer MEG source maps on a single-subject basis in a well-known pre-surgical mapping paradigm. The reliable-fraction metric paralleled the goodness-of-fit

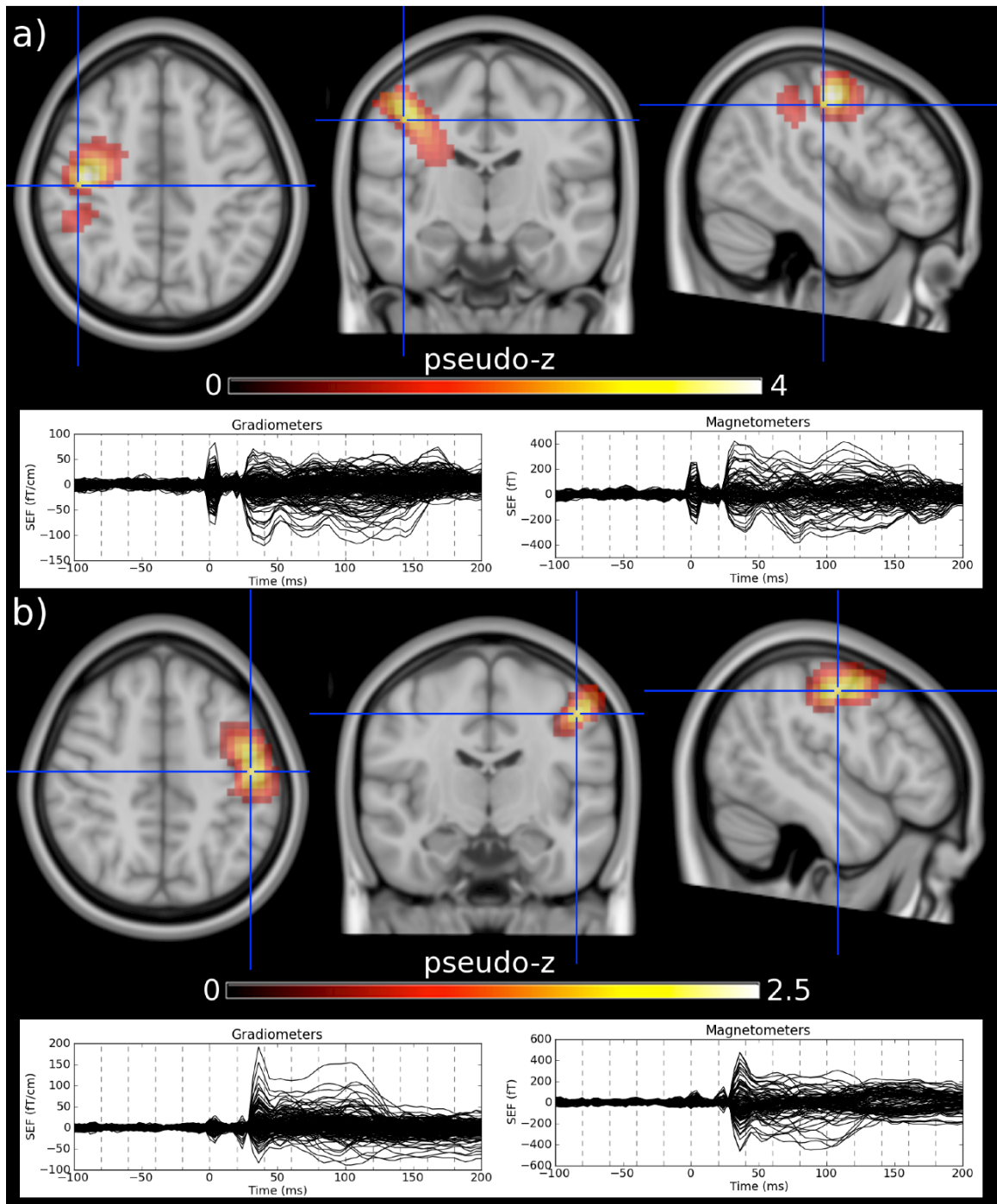


Figure 4.4: Representative dipole/beamformer co-localizations. a) ROC-r thresholded beamformer map (red-yellow) and ECD (crosshairs) for a subject with co-localization (8.2 mm between ECD and ROC-r peak) similar to the group mean (8.3 ± 5.9 mm). b) ROC-r map and ECD location for a subject with co-localization (5.89 mm) representative of the group median (6.2 mm). In both of these subjects, the ECDs were located within beamformer source clusters.

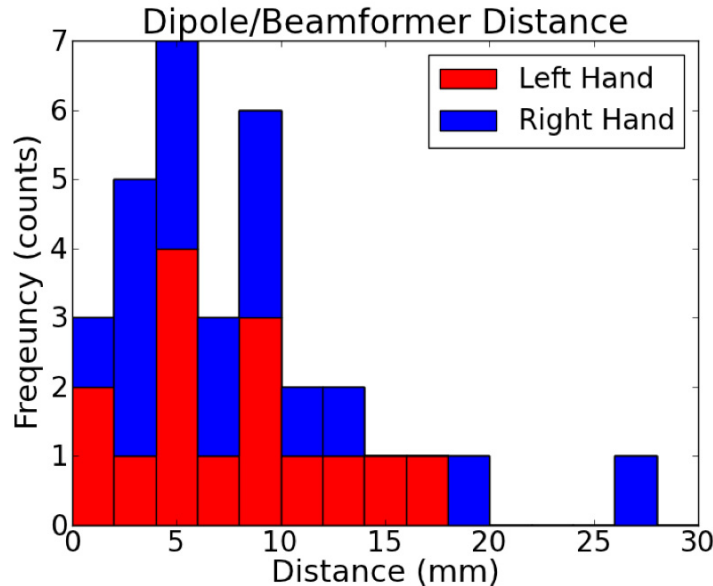


Figure 4.5: Histogram of the distance between the ECD and beamformer cluster locations. The distribution is skewed by a small number of datasets with high distances between the ECD and cluster peaks, resulting in a higher mean (8.3 ± 5.9 mm) than median (6.2 mm) distance. No obvious difference between left and right MNS was observed.

from ECD modelling, and automated thresholding co-localized with the gold-standard ECD locations. Overall, ROC-r analysis enhances MEG for pre-surgical mapping by reducing the need for expert intervention in the production and assessment of volumetric images.

4.6.1 The MNS SEF

We observed a robust P35m peak in most subjects, with more variable peaks between 50-120 ms. Notably, we did not reliably observe the N20m peak, which is frequently used in clinical mapping studies [29]. Our failure to produce an N20m peak was likely due to the number of stimuli used in this study. The N20m peak is known to have less than half the amplitude of the P35m, and most studies reporting the N20m use 200 to 500 stimuli to produce the SEF [23, 139]. With more stimuli, we would expect an enhanced N20m. Likewise, Sutherland *et al.* [144] showed that the later latencies of the SEF (i.e. > 50 -60 ms) produce bilateral sources, although the ipsilateral sources were much weaker, and were therefore not observed in this work.

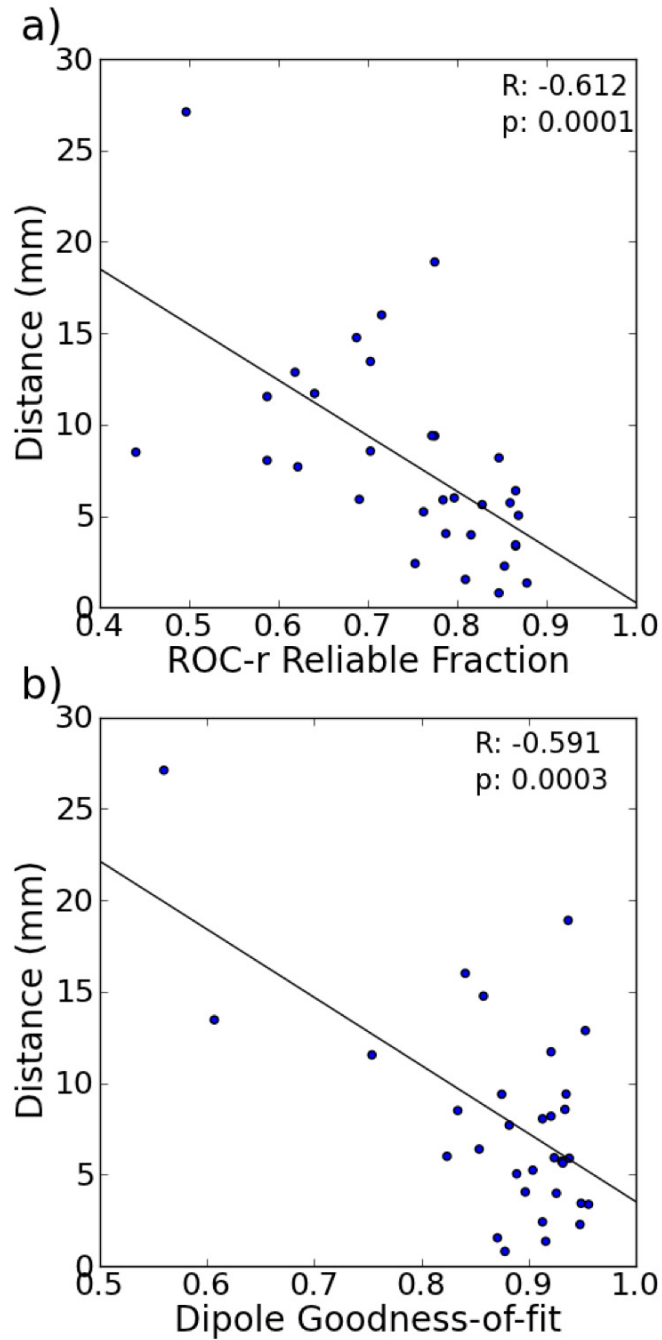


Figure 4.6: Relationship of a) ROC-r reliable-fraction and b) ECD goodness-of-fit to the distance between the ECD and beamformer peak locations. Co-localization accuracy increases with increasing GoF or F_R , suggesting that data with high beamformer reliability and strong dipolar field patterns co-localize closely. F_R was a slightly stronger predictor ($R = -0.612$) of accuracy than GoF ($R = -0.591$).

We also observed SEF peaks at later latencies (60-120 ms) than those typically described in MEG MNS studies (20-60 ms), but agreeing with Huttunen *et al.* [133], who described a late negative deflection in the SEF (\sim 60-120 ms). Indeed, a recent pre-surgical mapping study using MNS found the largest SEF peak occurred as late as 162 ms in some subjects, and that this component also localized to the post-central gyrus [136].

4.6.2 ROC-reliability for Quality Assurance

The lack of established quality assurance metrics has been an issue for clinical implementation of beamformer imaging, as unreliable source images are potentially deleterious. We validated the ROC-r F_R as a quantitative metric suitable for quality assurance of single-subject MEG beamformer maps. The development of an analogue to ECD GoF for beamformer imaging is a major step forward for applying volumetric source maps in the clinical theatre.

While correlation between F_R and GoF was generally high, there were exceptions. For example, the F_R values and variability were lower than the GoF during the baseline period. We consider this an advantage for ROC-r, as we expect no evoked activity during the pre-stimulus period, and thus the reliability of source localization during this time should be low. Additionally, low variability during baseline/inactive intervals makes it easier to discern later latencies with robust evoked responses. We also observed that low dipole GoF does not rule out the potential for a reliable beamformer solution, which will be advantageous in the case of mapping brain activity with complex field patterns. For MNS mapping, the later latency evoked responses have been shown to be consistent with bilateral sources [144], and we may therefore expect to see a divergence of the dipole GoF and ROC-r F_R in this case. That we did not observe this mismatch between the GoF and F_R at later latencies (> 50 ms) is possibly due to the relatively low number of trials rendering the ipsilateral response indiscernible from the background noise.

It is thus likely that ROC-r quality assurance will provide the most improvement over GoF for multiple or distributed cortical sources, such as pre-surgical mapping of language [145, 146]. In these cases, the evoked field patterns may not be dipolar in form, but still reflect true neural activity. While a multiple dipole model could be

employed, this would require *a priori* specification of the number of dipoles, requiring expert user intervention and introducing inter-rater variability. ROC-r could be used in these cases to quantitatively determine the latencies of reliable sources.

4.6.3 ROC-r Thresholding to Localize MEG Sources

While some beamformer thresholding approaches have been described previously [82, 147, 148], threshold selection is still often adjusted manually on an *ad hoc* basis, to isolate desired source peaks. For example Alikhanian *et al.* manually specified different thresholds for each frequency band in their data to avoid bias towards higher signal power at lower frequencies [149]. However, we have shown that data-driven methods can provide the flexible threshold levels needed to reliably localize MEG sources, while also eliminating inter-rater variability.

It is important to acknowledge that the spatial extent of beamformer clusters is not an accurate representation of the spatial extent of the underlying sources. Nonetheless, ROC-r is able to determine appropriate threshold levels for separating the reliable and unreliable clusters, with the assumption that this correspondingly separates neural sources from noise. Therefore, for beamformer maps only the peaks of the reliable clusters should strictly be used for localization. However, other MEG localization techniques that are sensitive to spatial extent like dynamic statistical parametric mapping (dSPM [76]) or maximum entropy on the mean (MEM [150]) could potentially bypass these issues, but are outside the scope of this manuscript.

The ROC-r beamformer cluster peaks co-localized closely to the ECD locations. The most comparable beamformer/ECD co-localization study in the literature was reported by Cheyne *et al.* [140]. They found the N20m localized by an event-related beamformer and ECD were on average 6.3 ± 2.3 mm apart for right MNS and 5.5 ± 2.0 mm for left MNS. Our study produced similar co-localization accuracy with entirely automated methods, albeit using a different beamformer implementation and SEF component.

ROC-r produced multiple clusters for approximately 20% of datasets. This demonstrates the potential advantage of whole-brain source reconstruction methods over ECD fitting, as these clusters were recovered without *a priori* specification of their

number or configuration. Examples of ECD dipoles located between multiple beamformer peaks (e.g. Figure 4.4a) suggest that co-localization accuracy can be poor due to mislocalization of the ECD dipoles in the presence of multiple sources. This hypothesis could be tested through simulations.

4.6.4 Data Quality Influences Co-localization Accuracy

We showed that both GoF and F_R were significant predictors of co-localization accuracy. Of course localization by either method is suspect when the respective quality assurance metric is low. However, we unexpectedly observed 2/36 datasets with strong ECD fits, for which there was no reliable beamformer activity. The beamformer calculation relies primarily on accurate data and noise covariance calculations, so it is possible that changing the covariance windows could produce a reliable beamformer in these cases.

4.7 Conclusion

The addition of ROC-r analysis to beamformer imaging offers crucial benefits in the clinical environment, integrating push-button mapping with built-in quality assurance. We showed that ROC-r reliable-fraction is a suitable quality assurance metric for volumetric MEG source maps, with high correlation to the GoF used routinely for ECD modelling. Furthermore, the ability of ROC-r analysis to determine data-driven thresholds was demonstrated with MEG data for the first time, and validated by co-localization with the standard ECD model. While we demonstrated ROC-r analysis for beamformer imaging of MNS, we expect these methods to generalize to other stimulation paradigms and volumetric imaging techniques. The greatest benefit of this method will likely be for paradigms that elicit concurrent cortical sources, due to the ability to detect multiple source clusters without *a priori* specification of the number of sources or threshold levels. The introduction of a quality assurance metric for volumetric MEG source maps provides a much-needed tool for the clinical environment.

Chapter 5

Manuscript 3: Improving fMRI Reliability in Pre-surgical Mapping for Brain Tumors

Authors: Tynan Stevens, David B. Clarke, Gerhard Stroink, Steven Beyea, Ryan D’Arcy.

Status: Published (online)

Journal: Journal of Neurology Neurosurgery and Psychiatry

Contribution: Conceptualization, Data Collection, Data Analysis, Primary Author

Copyright: Open access, no permission required.

5.1 Motivation

The following manuscript applies the ROC-r method in a group of patients undergoing surgical treatment for brain tumors. This paper focusses on the ability of ROC-r to classify datasets as reliable or unreliable, and to determining pre-processing steps that can be used to increase the quality of the pre-surgical maps. The ability to identify unreliable datasets is crucial in the clinical environment, as poor quality images will provide misleading information on localization of brain function. By showing that datasets that have high ROC-r F_R scores are also better at predicting the location of critical eloquent cortical regions, we demonstrate that the ROC-r metrics provide clinically meaningful quality assurance of pre-surgical maps. Furthermore, by automatically identifying the best pre-processing options, including activation thresholds, reliable activation maps can be produced without user-intervention. This eliminates the influence of inter-rater variability on the result of the functional mapping process, and thus provides a standardized and yet flexible approach to pre-surgical mapping.

In this manuscript, the locations of cortical activation identified by fMRI will be compared to cortical stimulation in order to provide an external reference standard for eloquent cortex. Cortical stimulation (CS) is frequently used as the gold standard for critical functional cortex [57], as the elicitation or disruption of brain function

using CS is predictive of post-operative morbidity associated with surgical resection of a section of cortex. While the use of CS as a gold standard is ubiquitous in the literature, in several ways it is not ideal as a reference standard for fMRI. Firstly, CS is a point-stimulation technique, and can only be used to map the relatively small surgically exposed portion of the cortex. Furthermore, while the electric current used for stimulation propagates a few millimetres into the cortex [52], deep sites are generally inaccessible by CS. Thus there are many regions which may be identified by pre-surgical mapping as responding to a task that can not be evaluated intraoperatively. In addition, while it is typically assumed that cortical stimulation effects are localized to the patch of cortex under the stimulating probe, evoked potentials in distant cortical regions have been reported [13], and these distant effects are difficult to predict and rarely monitored.

In this paper, the fMRI activation maps produced through ROC-r optimization are assessed in terms of their ability to predict the location of critical eloquent cortex, as measured by CS. Two metrics are used for this purpose: the fMRI to CS distance, and the sensitivity/specificity of the fMRI results. The fMRI to CS distance is the simplest outcome measure for the presurgical maps, and is calculated from the CS point to the centre of the nearest active voxel on the fMRI map. When the fMRI to CS distance is low, eloquent cortex is likely to be located near or within the borders of the fMRI activations, and thus the utility of the presurgical maps for guiding the CS process is high.

In order to calculate sensitivity and specificity, studies typically establish small search volumes around each eloquent location to define the ‘true’ critical functional regions. The presence or absence of fMRI activity within these true critical regions then defines the sensitivity of the pre-surgical paradigm. Likewise, the remaining areas of exposed cortex are defined as non-eloquent cortex, and are used to measure the specificity of the pre-surgical protocol. This analysis allows one to distinguish a technique with high sensitivity due to over-estimation of activation (i.e. low specificity) from one with high sensitivity and a low false positive rate (i.e. high specificity). Larger search ranges around each CS location inherently produce higher sensitivity and lower specificity, and while there is no consensus on the best search range to use, typical values range from 0 mm (direct matching only) to 15 mm. Higher search

ranges may be more appropriate for an augmentative pre-surgical protocol, whereas lower search ranges are suitable for assessing a technique as a potential replacement for CS.

The two CS based metrics thus provide a clinically relevant context for evaluating the success of a pre-surgical mapping protocol. Low fMRI to CS distance is required for fMRI to be suitable in guiding cortical stimulation investigations, while sensitivity/specificity analysis allows one to distinguish between co-localization achieved by chance (i.e. with low specificity) from a truly predictive technique. Furthermore, the search range used to achieve a certain level of sensitivity can help to distinguish a pre-surgical protocol suitable for replacing CS (i.e. high sensitivity even for very small search ranges) from one that is best suited to augmentative use (larger search ranges needed for high sensitivity).

5.2 Abstract

Purpose: Functional MRI is becoming increasingly integrated into clinical practice for pre-surgical mapping. Current efforts are focused on validating data quality, with reliability being a major factor. In this paper, we demonstrate the utility of a recently developed approach that uses Receiver Operating Characteristic-reliability (ROC-r) to: 1) identify reliable vs. unreliable datasets; 2) automatically select pre-processing options to enhance data quality; and 3) automatically select individualized thresholds for activation maps.

Methods: Pre-surgical fMRI was conducted in 16 patients undergoing surgical treatment for brain tumors. Within-session test-retest fMRI was conducted, and ROC-reliability of the patient group was compared to a previous healthy control cohort. Individually optimized pre-processing pipelines were determined to improve reliability. Spatial correspondence was assessed by comparing the fMRI results to intraoperative cortical stimulation mapping, in terms of the distance to the nearest active fMRI voxel.

Results: The average ROC-reliability for the patients was 0.58 ± 0.03 , as compared to 0.72 ± 0.02 in healthy controls. For the patient group, this increased significantly to 0.65 ± 0.02 by adopting optimized pre-processing pipelines. Co-localization of the fMRI maps with cortical stimulation was significantly better for more reliable versus

less reliable datasets (8.3 ± 0.9 mm versus 29 ± 3 mm, respectively).

Conclusion: We demonstrated ROC-r analysis for identifying reliable fMRI datasets, choosing optimal pre-processing pipelines, and selecting patient-specific thresholds. Datasets with higher reliability also showed closer spatial correspondence to cortical stimulation. ROC-r can thus identify poor fMRI data at time of scanning, and allow for repeat scans when necessary. ROC-r analysis provides optimized and automated fMRI processing for improved pre-surgical mapping.

5.3 Introduction

5.3.1 Pre-surgical Mapping Validity and Reliability

Functional magnetic resonance imaging (fMRI) is increasingly being used to map eloquent cortex prior to surgical treatment for brain tumors [57, 151]. The goal of pre-surgical mapping is to identify functional brain regions near the tumor, to plan surgical approach, identify risks, and potentially render intra-operative electrocortical stimulation (CS) unnecessary. Functional MRI is attractive for this purpose due to non-invasiveness, repeatability, high spatial resolution, and broad availability [16, 152].

Validated pre-surgical fMRI protocols were demonstrated first for sensory-motor function [36], followed by language localization [37, 47], and more recently memory mapping [153]. These validation studies compare fMRI localization with a gold standard measure such as CS. The concordance of fMRI and CS is influenced by the matching criteria used [49], field strength [57], pre-surgical tasks employed [51], and by the threshold used during fMRI analysis [154]. A recent review asserts that this heterogeneity has led to widely varying estimates of the accuracy of fMRI compared with CS [57].

Functional MRI results have a high degree of variability [92, 98, 155], and although inter-subject variability is higher than intra-subject variability, a single scan fMRI experiment includes a substantial amount of false positives and false negatives. Repeating scans is thus useful in order to produce more reliable activation maps for an individual patient. For example, Beisteiner *et al.* [39] restricted fMRI activity to only those voxels that survived high correlation thresholds in all repetitions of a motor

task. This resulted in fewer active voxels, with improved reliability and closer spatial correspondence to CS results.

Variability in fMRI can also be mitigated by using individualized data-driven pre-processing strategies. Gonzalez-Ortiz *et al.* [156] showed that built-in scanner analysis software was often sufficient for pre-surgical mapping, but 3rd party packages offered superior flexibility, reduced noise, and were preferred by radiologists. However, they were unable to provide quantitative guidelines for determining the best pipeline for a given fMRI dataset. Quality assessment tools are clearly needed in order to objectively determine the optimal pre-processing settings on a case-by-case basis.

In this context, tools such as NPAIRS (Non-parametric Prediction, Activation, Influence and Reproducibility reSampling), [61, 157, 158] and empirical ROC analysis (Receiver Operating Characteristic) [88, 132, 141] are used to determine optimized, subject-specific pre-processing pipelines. These techniques are especially important in patient populations, as clinical disorders generally decrease fMRI reliability [92, 110, 159].

5.3.2 Thresholds for Pre-surgical Mapping

In fMRI analysis, statistical thresholds are used to estimate the extent of activation, impacting reliability and accuracy of the resulting maps [67]. It has been argued that fixed statistical thresholds do not account for individual variability, differences in scanning hardware or software strategies, functional tasks or modalities, or habituation to testing conditions [51, 57, 154, 160]. Our group also showed that fixed error rate thresholds do not provide optimal reliability for individual subjects [141], and validation studies of concordance with CS have demonstrated that optimal thresholds vary between individuals and functional tasks [51, 154].

In practice, manual adjustment of threshold levels is often used, with implicit risks of inter-rater differences. Data-driven thresholds address this problem by using quantitative and reproducible methods [80, 88, 141]. These methods are sensitive to variations in fMRI activation levels, and have demonstrated reliable fMRI results across a variety of experimental conditions. Crucially, these approaches can be applied at the individual patient level.

5.3.3 The ROC-reliability (ROC-r) Framework

We recently introduced a ROC-reliability analysis framework (ROC-r) [141], which summarizes test-retest reliability through plots of the area under the ROC curve (AUC) versus analysis threshold (e.g. Figure 5.4c). We demonstrated that ROC-r is useful for assessing fMRI reliability, selecting pre-processing pipelines, and determining optimal analysis thresholds [141]. The ROC-r method is uniquely capable of automating the production of activation maps, thereby producing reliable push-button results.

In this study, we will demonstrate the application of ROC-r fMRI analysis to a group of patients who also received intraoperative CS mapping. The study was designed to address the following three hypotheses: 1) ROC-reliability will be lower for patients compared to healthy controls [92]; 2) reliability of single-subject maps will be improved by optimizing analysis pipelines; and 3) comparing the ROC-r optimized fMRI activations with CS mapping results, we expect higher spatial correspondence in data sets with higher reliability. We expect ROC-r to be beneficial for pre-surgical mapping by combining clinically relevant quality assurance with push-button activation map production in a single framework.

5.4 Methods

5.4.1 Participants

Sixteen patients (39 ± 13 years of age; 9 female, 7 male; 13 right-, 2 left-, 1 mixed-handed) receiving surgical intervention for brain tumors volunteered for the fMRI study. All volunteers underwent pre-surgical fMRI, and most received cortical stimulation during surgery ($n = 13$). This study was done in compliance with the local research ethics board (Capital District Health Authority REB, Halifax, NS), and subjects provided informed consent prior to enrollment. Tumor types and locations were heterogeneous. For a complete list of age, sex, handedness, tumor location, and type refer to table 5.1. A control group ($n = 8$) for this study was previously described, and performed both the finger tapping and sentence reading tasks (see below) [141].

Table 5.1: Characteristics for the sixteen patient volunteers included in this study. Lt = left; rt = right; mx = mixed; ant = anterior; post = posterior; inf = inferior; sup = superior; fr = frontal; temp = temporal; par = parietal; CS = cortical stimulation; FT = finger tapping; ON = object naming; SC = sentence reading; F = female; M = male

Pt	Sge	Sex	Hand	Tumor Type	Tumor Location	CS	FT	ON	SC
1	35	F	Rt.	Anaplastic oligoastrocytoma (Gr. 3)	Lt. inf. fr.	X	X	X	
2	46	F	Rt.	Glioblastoma multiformae (Gr. 4)	Lt. ant. temp.	X			X
3	24	F	Mx.	Glioblastoma multiformae (Gr. 4)	L.t ant. temp.	X		X	X
4	62	M	Lt.	Oligodendroglioma (Gr. 2)	Lt. inf. fr. / ant. par.	X	X	X	
5	20	M	Rt.	Cavernous angioma	Lt. inf. par.	X	X		X
6	26	F	Rt.	Mixed oligoastrocytoma (Gr. 2)	Rt. inf. fr.	X		X	
7	51	F	Rt.	Meningioma	Rt. fr. / central		X		
8	47	F	Lt.	Ruptured cyst	Rt. sup./post. temp.		X	X	X
9	48	F	Rt.	Glioblastoma multiformae (Gr. 4)	Lt. inf. fr.	X		X	X
10	45	F	Rt.	Glioblastoma multiformae (Gr. 4)	Lt. inf. fr.	X	X	X	X
11	22	M	Rt.	Diffuse astrocytoma (Gr. 2)	Lt. fr. / temp.		X	X	X
12	32	M	Rt.	Glioblastoma multiformae (Gr. 4)	Lt. ant. temp.	X		X	X
13	44	M	Rt.	Oligoastrocytoma (Gr. 2)	Lt. ant. temp.	X	X	X	X
14	23	M	Rt.	Dysembryoplastic neuroepithelial	Lt. inf. temp.	X	X	X	X
15	59	F	Rt.	Glioblastoma multiformae (Gr. 4)	Rt. inf. fr.	X	X	X	X
16	41	M	Rt.	Pleomorphic xanthoastrocytoma (Gr. 2)	Lt. middle temp.	X	X	X	X

5.4.2 MRI Acquisition Details

All 16 volunteers were scanned using a 4 T scanner (Varian INOVA, Palo Alto, California). Structural images were collected with an MP-FLASH sequence: TI = 500 ms, TR = 10 ms, TE = 5 ms, $\alpha = 11^\circ$, 256 x 256 matrix, 190 slices, and 0.94 x 0.94 x 1 mm voxels (FOV = 24 x 24 x 19 cm). Functional images were collected with a two-shot spiral out sequence, using TR = 2 s, TE = 15 ms, $\alpha = 90^\circ$, 64 x 64 matrix, 22-25 slices, and 3.75 x 3.75 x 4.0 mm voxels, with a 0.5 mm gap (FOV = 24 x 24 x 10-11 cm). Test-retest imaging was performed within-session. A variety of tasks were included in this study, depending on the brain tumor location and planned CS investigations for each patient (Table 5.2). The finger tapping task was used for patients with tumors near the primary motor cortex (i.e. central sulcus region) or secondary motor cortex (i.e. pre-central sulcus). The object naming task was used preferentially for patients with tumors in the inferior frontal lobe (Broca’s area), or the inferior central sulcus region, and occasionally included for temporal lobe lesions. The sentence reading task was used for patients with tumors in either the temporal lobe or inferior frontal lobe.

5.4.3 Functional MRI Analysis

Functional MRI analysis was performed using the AFNI software package [119], in combination with tools written in the Python programming language. Initial pre-processing steps were applied universally, including rigid body motion correction. Segmentation isolated the brain from both the functional and anatomical images. Down-sampled anatomical images were registered to the functional image using a 12 parameter affine transformation.

The remaining pre-processing options were optimized individually, including: 1) spatial smoothing (3, 6, and 9 mm FWHM), 2) motion parameter regression (MPR: on/off), and 3) auto-correlation correction (ACC: on/off). All combinations ($n = 12$) of these options were analyzed using the ROC-r methodology described below. The default pipeline (6 mm smoothing, no MPR, and no ACC) was used unless significant reliability improvements were observed with an alternative combination. Statistical analysis was carried out using 3dDeconvolve/3dREMLfit in AFNI. Low frequency signal fluctuations were removed by 2nd order polynomial regression.

Table 5.2: Summary of the functional tasks used in this study. A variety of tasks were included in this study, including both language and motor tasks, with various block and scan lengths, using both active and passive control conditions. M = motor; L = language. *<http://wiki.cnbc.cmu.edu/Objects> **http://wiki.cnbc.cmu.edu/Novel_Objects.

Task	Type	Active Condition	Blocks	Control Condition	Blocks	Fixation Condition	Blocks	Block Length	Total Duration
Finger tapping	M	Four-finger ascending/descending paced (2Hz) tapping	4	N/A	0	Fixation cross	5	20s	180s
Object naming	L	Overt object naming of 3D color images, 8/block*	6	3D non-sense images**	6	Fixation cross	7	16s	304s
Sentence Reading	L	Correct/incorrect written sentences (e.g. 'She swept the floor with a sand'), 4/block	6	Correct/incorrect math statements (e.g. '2+2=5' vs. '2+2=4')	6	Fixation cross	7	18s	342s

5.4.4 ROC-reliability Analysis

ROC-r analysis measures test-retest reliability in terms of the overlap of active/inactive regions in the activation maps as a function of image thresholds. Briefly, one of the images is designated as the template image, acting as a measure of the true activation pattern. At a fixed threshold on the template image, the retest image is assessed against the template for true and false positive detections, and the resulting true-positive and false-positive rates are calculated as a function of retest image threshold. This creates an ROC-reliability curve for the retest image, and this is repeated for each template image threshold (in increments of 0.1). From this, the retest area under the curve (AUC) is plotted as a function of template threshold, and the procedure is repeated with the roles as template and retest image reversed. Currently, the ROC-r calculation takes only a few seconds on typical fMRI images.

The ROC-r metric ‘reliable fraction’ (F_R) was used to measure overall dataset reliability. The F_R is the proportion of the image t-value range for which the AUC is more than the mid-range (i.e. $AUC > [AUC_{max} + AUC_{min}]/2$). F_R was measured for each pre-processing pipeline, and the best pipeline was identified for each dataset based on this reliable fraction. Changes in reliability with pipeline optimization were assessed with paired t-tests at the group level, whereas comparisons between controls and patients used independent samples t-tests. Images were divided into ‘reliable’ and ‘unreliable’ categories based on whether the reliable fraction was above or below the (patient) group mean respectively.

ROC-r was also used for automated threshold selection. The threshold was set where the AUC curve satisfied two conditions: 1) above average AUC (i.e. $AUC > \alpha[AUC_{max} + AUC_{min}]/2$), and 2) below average AUC derivative (i.e. $dAUC/dt < \beta[AUC_{max} - AUC_{min}]/[t_{max} - t_{min}]$). The tuning parameters α and β can be used to increase or decrease the ROC-r thresholds (higher α values tend to increase the threshold levels, whereas higher β values tend to decrease threshold levels). Herein they were set to 1 and 1.5 respectively, which provided similar average threshold levels to the previous control group. [141]

5.4.5 Cortical Stimulation

CS mapping was performed using an Ojemann OCS-1 cortical stimulator with a bipolar probe (5 mm spacing) using 0.2-0.5 ms duration pulses. Current levels were increased incrementally from 4 mA (peak-to-peak) in steps of 2-6 mA to a maximum of 20 mA or until a response was elicited. Sensorimotor mapping used 5 Hz pulse-rate, whereas language investigation used 60 Hz, in accordance with standard clinical practice.

For sensorimotor investigations, involuntary movements and/or reported sensations were recorded. Language mapping used counting, reciting days of the week, reciting months of the year, and object naming. Locations that consistently produced a response were recorded either as sensorimotor or language CS-positive (CS+) result. Areas that produced no effect were recorded as CS-negative (CS-) locations.

5.4.6 Spatial Correspondence Measurements

To facilitate quantitative spatial comparisons between the pipeline-optimized fMRI and CS, each stimulation location was digitized in MRI coordinates using a neuro-navigation system. A digitization of the cortical surface was obtained using the neuro-navigation system at approximately 0.5 cm spacing across the exposed patch of cortex. Brain shift was corrected for using iterative closest-point registration, in order to minimize the sum-of-squares distance between the digitized cortical surface and the brain surface extracted from the anatomical MRI [161]. This approach is used routinely for co-registering 3D surfaces [162].

Correspondence was measured by the distance from each CS+/CS- site to the centre of the nearest active fMRI voxel (using the relevant language or sensorimotor maps). This was calculated as a function of fixed thresholds, and maps with above and below average F_R were compared. Only CS points at least 1 cm apart were used to avoid oversampling the CS data, which is typically assumed to deposit current in approximately a 5-10 mm radius [50].

ROC curves were calculated from the CS-fMRI distances at the ROC-r optimized thresholds. Sensitivity and specificity were defined in terms of whether or not there was fMRI activity within a spherical ROI around each CS+/CS- location (see table 5.3). The ROC curves were then calculated by varying the ROI search range criteria

Table 5.3: Sensitivity ($TP/[TP+FN]$) and specificity ($1-FP/[FP+TN]$) were calculated from the CS-fMRI separation distances. TP = True positive, FP = false-positive; TN = true-negative; FN = False-negative.

	CS+	CS-
fMRI within search range	TP	FP
No fMRI in search range	FN	TN

from 0-40 mm, which was more than sufficient to capture the 0-20 mm search ranges reported in similar studies [57].

5.5 Results

5.5.1 Reliability

The mean F_R for the patient group (0.59 ± 0.03) was significantly smaller ($p = 1 \times 10^{-4}$) than our previous control group (0.72 ± 0.02). Figure 5.1a shows a normalized histogram of the reliable fraction for each group, revealing a higher proportion of datasets with reliable fractions below 0.4 for the patient group (20% vs. 3%). This included three images for which no reliable activation was detected. Likewise, there were fewer datasets in the highest F_R range for patients (15% vs 33%), although the maximum F_R was similar for both groups (0.91 vs. 0.89). There was also a significant reliability difference between finger tapping and the language tasks, as shown in Figure 5.1b.

5.5.2 Pipeline Optimization

The mean reliability increased to 0.65 ± 0.02 after pipeline optimization (figure 5.2a). This was a significant improvement over the default pipeline ($p = 7 \times 10^{-7}$), although still significantly lower than the control group ($p = 8 \times 10^{-3}$). The smallest gains were made for the finger tapping task (figure 5.2b), although this difference was statistically significant ($p = 0.043$). The sentence reading and object naming tasks had more significant reliability improvements ($p = 4 \times 10^{-5}$ and $p = 8 \times 10^{-4}$, respectively).

The default pipeline was optimal most frequently ($n = 16$), followed by 9 mm smoothing ($n = 12$), and 9 mm smoothing with MPR ($n = 10$). The remaining frequencies are shown in table 5.4. Overall the three smoothing kernels (3 mm, 6

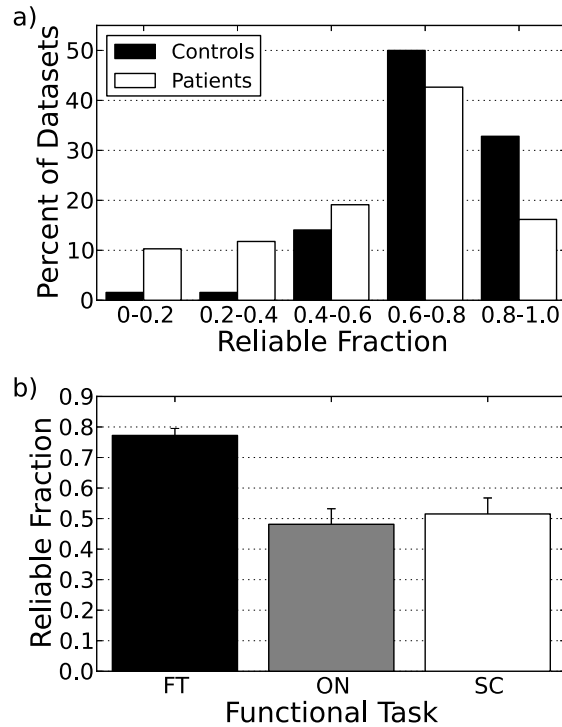


Figure 5.1: Reliability of pre-surgical fMRI measured with the ROC-r reliable fraction: a) Reliable fraction histograms of patients and controls. b) The F_R by task. FT = finger tapping; ON = object naming; SC = sentence reading.

mm, 9 mm) were chosen 16, 28, and 24 times respectively. MPR was used for 24 of 68 datasets, and ACC were applied to 10 the 68 images.

5.5.3 Spatial Correspondence with CS

CS data were obtained from 11 of 13 patients. In one patient CS had no effect, and for one other the available CS data were not relevant to the available fMRI datasets. These 11 patients provided 28 CS+ tags (9 motor, 19 language), and 53 CS- tags. There were 38 fMRI images that provided relevant comparisons with the CS data (6 motor, 32 language).

The fMRI to CS+ distance increases monotonically with threshold, reaching 10 mm on average at $t = 3.4$ (figure 5.3). The reliable and unreliable images (i.e. above and below the group-mean F_R) datasets had significantly different spatial correspondence with CS for thresholds between $t = 2.5$ and $t = 16$. Co-localization was better than 10 mm for $t < 6.1$ for reliable images, as opposed to $t < 2.9$ for unreliable ones.

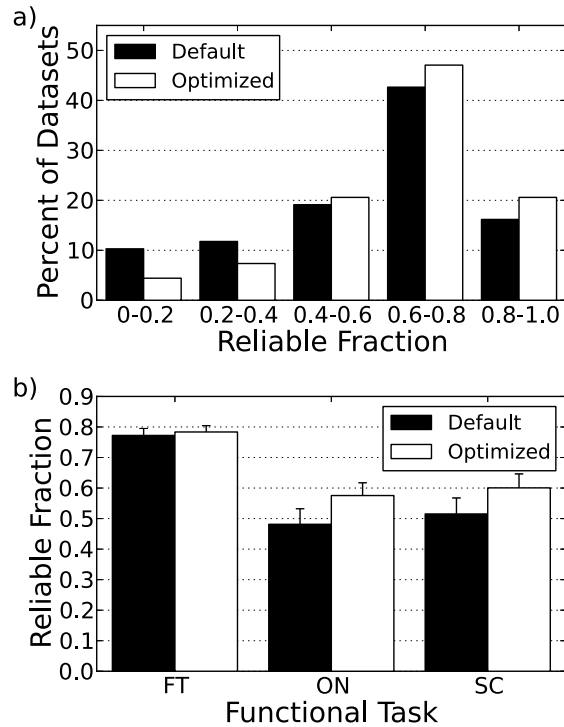


Figure 5.2: Effects of pipeline optimization in the patient reliability: a) the histogram shows a shift towards higher reliability following pipeline optimization. b) The majority of the improvement came from the initially less reliable sentence reading (SC), and object naming (ON) tasks.

For a fixed analysis threshold of $t = 6.0$, the mean fMRI-CS+ distance was 9.9 ± 0.9 mm for reliable maps, and 41 ± 5 mm for unreliable datasets.

5.5.4 Automatic Thresholding

The average ROC-r automated thresholds were 6.1 ± 0.1 . The average ROC-r thresholds were higher for the unreliable datasets (6.3 ± 0.2) than the reliable datasets (5.7 ± 0.2). Representative thresholded fMRI/CS datasets for typical patients are shown in figure 5.4, for both a reliable motor and language image. The language data shown are from the object naming task, which was the least reliable of the pre-surgical tasks. Nonetheless the example shown was above average when compared to the group mean.

Figure 5.5 shows the sensitivity and specificity of the automated thresholds for detecting eloquent cortex for search ranges from 0 to 40 mm. For a search range of 10 mm, overall sensitivity/specificity was higher for the ROC-r thresholds (50%/87%)

Table 5.4: Optimized pre-processing pipelines. A wide range of pipelines were used based on their ROC-r F_R scores. MPR = motion parameter regression; ACC = autocorrelation correction.

Smoothing	MPR	ACC	Freq.
3 mm	On	On	0
3 mm	Off	On	2
3 mm	On	Off	6
3 mm	Off	Off	8
6 mm	On	On	2
6 mm	Off	On	4
6 mm	On	Off	6
6 mm	Off	Off	16
9 mm	On	On	0
9 mm	Off	On	2
9 mm	On	Off	10
9 mm	Off	Off	12

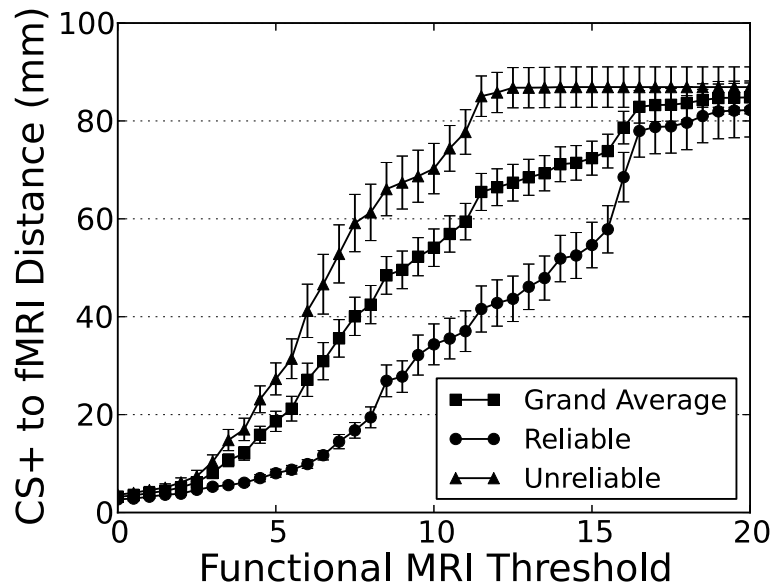


Figure 5.3: Average CS+ to fMRI distance as a function of analysis threshold. The separation between the CS+ and nearest fMRI activation increases with threshold. At very high thresholds, there is little-to-no activation remaining, resulting in very high CS-to-fMRI distances. The spatial correspondence is better for the more reliable datasets for most of the threshold range.

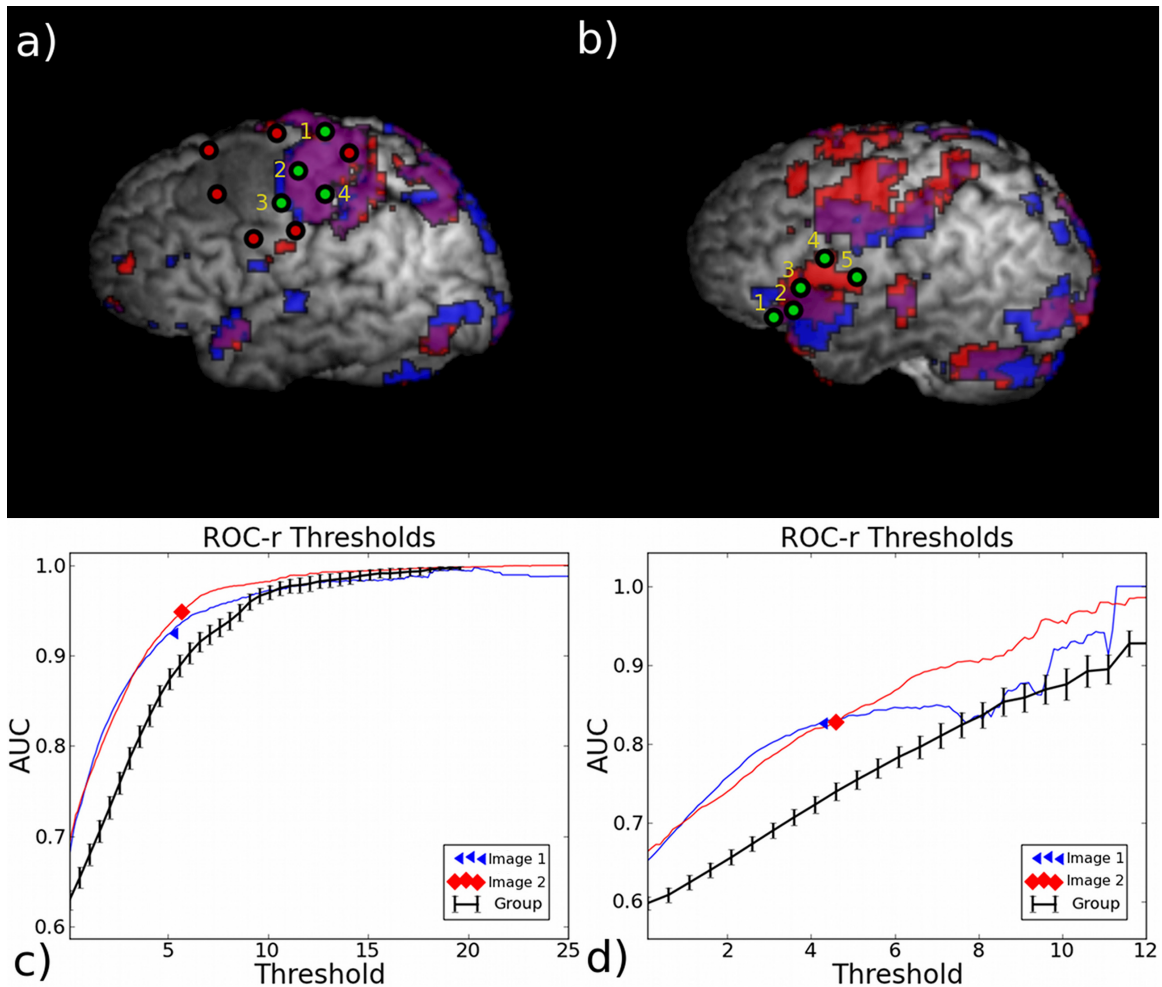


Figure 5.4: Example reliable thresholded activation maps for a) finger tapping and b) the object naming tasks. Corresponding ROC-r curves and thresholds are indicated in c) and d) respectively. Activation maps are shown for the test (blue) and retest (red) with overlap in purple. The CS+ (green circles) and CS- (red circles) locations are also shown. In a) the CS+ locations produced: 1,2) right hand twitch; 3,4) right wrist flexion. In b) the CS+ locations produced: 1-3) babbled speech; 4) speech interruption; 5) tingling sensation in lips. The ROC-r plots also show the mean ROC-r curves for each task from the patient group (black). For the object naming data shown, substantial motion was present (~ 1 mm), as is typical for this task. In this case, motion regression did not improve the reliability of the activation mapping.

than fixed thresholds ($t = 6.0$; 42%/84%). Increasing the search range to 15 mm produced 64%/76% sensitivity/specificity, whereas decreasing it to 5 mm produced 29% sensitivity and 94% specificity.

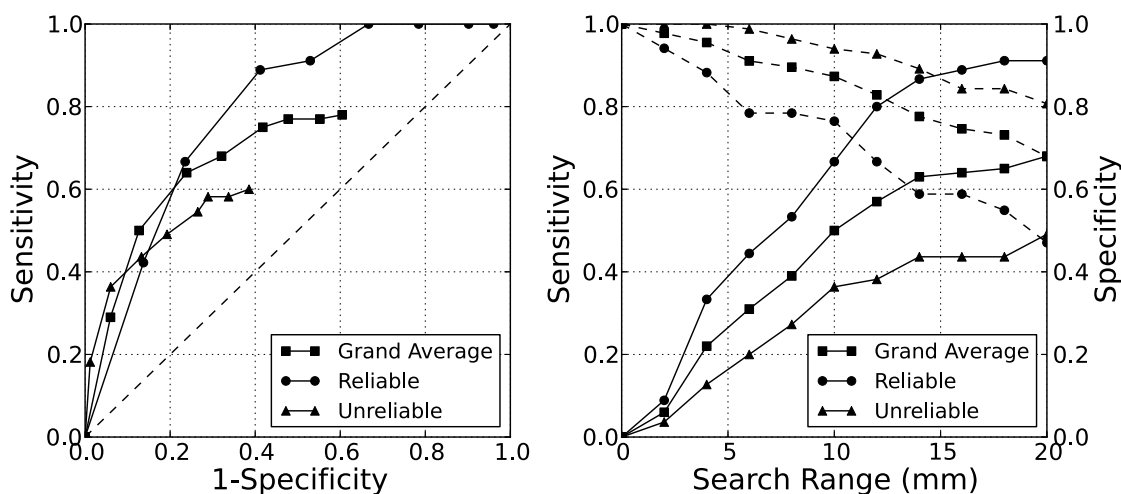


Figure 5.5: a) ROC curves and b) sensitivity (solid lines)/specificity (dashed lines) versus search range for localization of eloquent cortex (i.e. CS sites) using ROC-r thresholded maps. As the search range around each CS location is increased from 0 to 40 mm, the sensitivity increases and specificity decreases. The reliable datasets have higher sensitivity than the unreliable datasets for a given search range. Conversely the same sensitivity and specificity can be obtained using a smaller search range for the reliable datasets than the unreliable ones.

Reliable datasets were more sensitive but less specific than unreliable ones. For a 15 mm search range the sensitivity/specificity was 89%/59% and 44%/87% for reliable and unreliable images respectively. The reliable datasets were somewhat more sensitive and significantly more specific ($p < 0.05$, two-proportion z-test) when thresholded using the ROC-r algorithm (89%/59%) than fixed thresholds (82%/47%), whereas there was little difference in the two approaches for unreliable datasets (47%/85% vs. 42%/89%).

5.6 Discussion

5.6.1 Reliability of Pre-surgical fMRI

We found that the reliability of pre-surgical fMRI in brain tumor patients was lower than that of healthy controls (Hypothesis 1). In the case of brain tumor patients, this may be related to issues including difficulty with task performance due to functional deficits, and increased propensity for motion during scanning. However, this result is likely not specific to brain tumors. Lower reliability has previously been shown using intraclass correlation (ICC) in schizophrenia [163], although later no significant difference was seen using test-retest overlap [164]. Decreased patient reliability was also observed for multiple sclerosis [110], and mild cognitive impairment [159]. While the situation is not as clear for stroke patients, Kimberley *et al.* [99] and Eaton *et al.* [165] found increased between-subject variability falsely inflated the individual ICCs. Reliability measures using only within-subjects factors may therefore be more appropriate for comparing patient populations.

We observed higher reliability for finger-tapping compared to language tasks. This agrees with the review of Bennet and Miller [92], which showed that sensory/motor tasks are more reliable than higher cognitive tasks. The higher rate of false positive/negative voxels for cognitive tasks likely relates to the smaller fMRI signal changes typically evoked by these tasks, resulting in noisier time-course data.

5.6.2 ROC-r Pre-processing Optimization

We demonstrated optimization of individualized pre-processing pipelines using ROC-r analysis (Hypothesis 2). There was a high degree of heterogeneity between subjects, which agrees with previous reports on pipeline optimization [58, 158]. Only spatial smoothing and rigid motion correction have been found to be widely beneficial across subjects [58, 61, 158], which agrees with our results. The least reproducible pipelines were those that included both MPR and ACC, suggesting that over-fitting the data is detrimental to reproducibility of the activation maps. In the context of pre-surgical mapping, these results make it clear that advanced analysis strategies should only be adopted on an as-needed basis, and only in the presence of empirical evidence supporting their use.

The cognitive tasks benefitted the most from pipeline optimization. Partly, this represents a ceiling effect for the finger-tapping task, which was highly reliable with the default pre-processing pipeline. Motion parameter regression was used more frequently for the object naming task (12/26) than the finger tapping task (4/22), likely because of task-induced motion. A bias towards low smoothing (3 mm FWHM) for the sentence reading task (10/20) compared with the other tasks (6/48) was observed, which is consistent with smaller activation foci. With sufficient sample size, similar differences could be observed for other task comparisons, and reflect the lack of a ‘one size fits all’ approach to analysis of neuroimaging data. ROC-r analysis improves clinical fMRI methodology by selecting the most appropriate pipeline on a case-by-case basis, with the additional benefit of reduced reliance on expert intervention in the production of fMRI maps.

5.6.3 Clinical Utility of ROC-reliability Analysis

Datasets with higher reliable fractions were shown to have a better spatial correspondence to CS results (Hypothesis 3). This extends the earlier findings of Beisteiner *et al.* [39], which showed that reliably activated voxels co-localized with CS+ results. By identifying images unlikely to produce useful results as soon as the scan is completed, ROC-r analysis can guide decisions on data rejection and scan repetition. Conversely, datasets with high ROC-r reliable fractions can be used for pre-surgical mapping with enhanced confidence. This has clear clinical utility, as the risk of false-negative findings due to poor quality scans is reduced.

The sensitivity/specificity to CS depended on the search range used for matching CS results, as has been shown previously [54]. For a conventional 10 mm search radius, our overall sensitivity (50%) and specificity (87%) were similar to those found by Roux *et al.* [51] in 2003 (45-54% and 95% respectively). Overall, the sensitivity of the fMRI results suggests that the use of intra-operative mapping is still vital to guide surgical resection, in agreement with outcome based studies such as Spina *et al.* [166]. Nonetheless, ROC-r optimization improves the predictive power of the fMRI results, and therefore increases the utility of the pre-surgical mapping. The addition of ROC-r analysis to an fMRI protocol helps to ensure that the best results are produced from the available data.

Other studies have found higher sensitivity than specificity for pre-surgical fMRI [47, 51, 154], but frequently employ multiple tasks to increase the likelihood of a positive prediction. For instance, Rutten *et al.* [154] found 22-70% sensitivity and 73-93% specificity depending on the language task used, but increased sensitivity to 92% and decreased specificity to 61% by combining five tasks. Roux *et al.* [51] also used multiple tasks to increase sensitivity from approximately 50% to 66%, at the cost of decreased specificity (from 95% to 91%). In our study we only compared single tasks to CS. While we could achieve higher sensitivity by combining tasks, the clinical fMRI time constraints often limit the number of tasks and repetitions possible. These results show that task repetition is an alternative approach to enhance both sensitivity and specificity of fMRI pre-surgical mapping.

Another methodological consideration is the threshold levels used in previous studies, which are often lower than those determined by the ROC-r method. Rutten *et al.* [154] showed a decrease in sensitivity from 99% to 47% when the thresholds were increased from $t = 2.5$ to $t = 4.5$. They observed a concomitant increase in specificity from 23% to 80%. Higher sensitivity is desirable for pre-surgical fMRI to avoid false negatives, so future investigation could focus on optimizing the ROC-r α and β parameters to lower the threshold levels. This will provide the benefits of individualized thresholds with increased sensitivity.

There are several variables affecting fMRI-CS correspondence that we were unable to explore due to sample size and heterogeneity. For example, Pouratian *et al.* [49] found 33-70% specificity depending on the region of the brain being mapped (frontal/temporal). Bizzi *et al.* [54] showed that both sensitivity and specificity were higher for motor tasks (88% and 87% respectively) than language tasks (80% and 78%). This study also showed that sensitivity was higher for WHO grades II and III gliomas (93%) than grade IV (67%), whereas specificity showed the opposite dependence (76-79% versus 93% respectively). We had a high number of grade IV gliomas in our study, which likely contributed to the overall sensitivity. Larger sub-samples would be required to confirm this hypothesis.

Importantly, no previous study has demonstrated metrics available at the time of scanning that correlate with co-localization of fMRI and CS. We found higher sensitivity for datasets identified by ROC-r as reliable (66% for a 10 mm search range)

than unreliable (36%). This difference was even more dramatic using larger search ranges (e.g. 89% vs. 44% at 15 mm). While specificity was higher for unreliable images, this was accompanied by unacceptable false-negative rates ($> 50\%$), likely because there was little to no activation above threshold in these images. Furthermore, for any fixed sensitivity level above 50%, the specificity of the reliable datasets was actually higher than the unreliable images, as a smaller search range can be used (Figure 5.5). The ability of ROC-r to predict useful fMRI images provides a critically needed quantitative tool for assessing fMRI image quality in a clinically meaningful way.

5.7 Conclusion

We demonstrated that ROC-r is sensitive to differences in reliability between patient and control groups. The F_R quantifies the effects of pre-processing pipelines, enabling subject-specific strategies, and is especially beneficial for difficult applications like cognitive tasks and subject motion. ROC-r metrics were shown to predict co-localization, and can potentially be used to guide decisions regarding data rejection and scan repetition at the time of the scan. Finally, ROC-r can determine automated threshold levels, with higher sensitivity and specificity for eloquent cortex than a fixed threshold approach. In combination, these capabilities allow for fully automated and individualized fMRI processing. By facilitating push-button, yet individualized analysis, ROC-r reduces the need for expert intervention in data processing, increasing usability in the clinic, and furthering the impact of pre-surgical fMRI.

Chapter 6

Manuscript 4: A Unified Framework to Optimize fMRI and MEG Processing for Push-button Pre-surgical Mapping

Authors: Tynan Stevens, Ryan D'Arcy, David B. Clarke, Daniel McNeely, Tim Bardouille, Gerhard Stroink, Steven Beyea.

Status: Prepared for Submission

Journal: NeuroImage

Contribution: Conceptualization, Data Collection, Data Analysis, Primary Author

6.1 Motivation

The final manuscript of this thesis ties together the previous works. So far, ROC-r has been demonstrated to provide quantitative quality assurance for MEG and fMRI, to be useful for determining optimal pre-processing pipelines, and to produce robust individualized thresholding for single-subject imaging. In this paper, we directly evaluate ROC-r as a unified framework for reliable single-subject MEG and fMRI mapping. This work shows that by using optimized single-subject pipelines, similarly robust fMRI and MEG maps can be obtained automatically. This is an important result, as the use of fixed analysis pipelines could bias the comparison of fMRI and MEG reliability, and we have demonstrated that there is no universally best set of processing choices. In this paper, we include a patient case showing verification of the automated MEG and fMRI maps by co-localization with cortical stimulation. This manuscript thus shows that the ROC-r analysis framework leads to a unified approach to robust, push-button, and individualized processing of single-subject fMRI/MEG mapping.

6.2 Abstract

Purpose: Both functional MRI (fMRI) and Magnetoencephalography (MEG) have demonstrated potential as methods for pre-surgical mapping of brain function, and present unique technological and clinical benefits and drawbacks. Objective comparison of these technologies is hampered by the difficulty in comparing data processing pipelines and analysis choices at the single-subject level. We have evaluated a receiver operating characteristic reliability (ROC-r) based approach that solves this problem through an automated and data-driven approach. ROC-r quantitatively optimizes pre-processing pipelines and determines data-driven thresholds for both fMRI and MEG, using a unified approach across scanning modalities.

Methods: We demonstrated ROC-r for optimizing both functional MRI (fMRI) and magnetoencephalography (MEG) mapping of the primary motor cortex in 20 healthy controls. For fMRI, we tested two general linear models, with/without auto-correlation corrections, and with/without motion parameter regression. For MEG, we tested two trigger sources, with/without independent component analysis for artifact removal, and with/without low-pass filtering. Automated thresholds were determined for each subject using the optimally pre-processed data. We demonstrated our approach in a patient case, by comparing the pre-surgical mapping locations to intraoperative measurements.

Results: A wide variety of optimal pipelines were identified across subjects. MEG reliability depended more strongly on the pre-processing pipeline than fMRI, but the reliability of the optimal pipelines were similar for fMRI (0.69 ± 0.02) and MEG (0.71 ± 0.03). ROC-r optimized thresholds identified activation near the central sulcus for all fMRI datasets and 28/32 MEG datasets. The peak overlap of the individual level maps occurred in the primary sensorimotor cortices, reaching 88% overlap for fMRI and 80% overlap for MEG. The patient case demonstrated that the ROC-r automated mapping co-localized with the primary motor cortex as identified intra-operatively.

Conclusion: ROC-r optimization of fMRI and MEG pre-processing pipelines provided robust pre-surgical mapping, including automated data-driven thresholding, as demonstrated by co-localization with intra-operative measures. ROC-r allows for push-button analysis, streamlining the clinical implementation of functional mapping, and removing the need for manual intervention and selection of pre-processing

pipelines. Crucially, ROC-r permits a more fair comparison of functional mapping data quality in fMRI and MEG by removing the variability due to subjective data analysis decisions.

6.3 Introduction

Functional magnetic resonance imaging (fMRI) and magnetoencephalography (MEG) are safe and non-invasive means of localizing brain function, and thus attractive options for pre-surgical mapping [23, 29, 167, 168]. MEG is considered the more direct technique, measuring the magnetic fields produced by synchronous post-synaptic potentials [70], whereas fMRI measures brain activity indirectly through hemodynamic coupling [69]. This fundamental difference leads to the unique strengths and weaknesses of each technology. For example, spatial resolution is considered superior for fMRI, whereas the temporal resolution of MEG is advantageous when the dynamics of neural activity are of interest [169]. The two modalities are complementary, and getting the most out of their combined use is crucial for applications like pre-surgical mapping [169–182].

There are a vast number of methods available for analyzing fMRI and MEG data [183]. This is both an advantage, as it offers flexibility in extracting information from neuroimaging data, but also a burden, as the quality of the resulting maps will depend on the analysis methods chosen. The wide range of analysis strategies provides a particular challenge in single-subject studies encountered in clinical applications, as both fMRI and MEG are accompanied by a significant amount of inter-subject variability [155, 158, 184–188]. Individually tailored analysis strategies are required to overcome differences like subject motion during scanning, physiological noise from heart or breathing rhythms, and modulation of the cortical response by attention or arousal during the scan [60]. For example, motion regression can eliminate motion correlated signals, but in some cases this may result in unacceptable reduction of sensitivity. Manual evaluation of all pre-processing options is overwhelmingly time consuming, and the selection of appropriate analysis strategies on a single-subject level is therefore a formidable task [158, 186].

To address the difficulty of creating individualized data processing strategies in

fMRI and MEG, we recently developed a method of automatically selecting subject-specific processing pipelines using test-retest receiver operating characteristic reliability (ROC-r) [141]. This method can be applied to any volumetric source mapping pipeline, and optimization can be performed by selecting the pipeline with the highest within-subject reliability. ROC-r evaluates pre-processing pipelines solely in terms of the final activation maps, which forms the common link between fMRI and MEG source imaging. Therefore, unlike previous methods of fMRI pre-processing pipeline optimization like NPAIRS (nonparametric prediction, activation, influence and reproducibility resampling) [58, 61, 157, 158], ROC-r works without modification for MEG mapping. Additionally, this analysis produces threshold-dependent reliability estimates, which in turn can be used to determine data-driven thresholds, allowing for fully automated production of activation maps. ROC-r is highly advantageous in clinical settings as it eliminates the influence of the experimenter on the final activation maps, and provides a unified framework for optimizing fMRI and MEG processing choices.

In this study, we evaluate our unified approach to automated pipeline selection and activation thresholding for fMRI and MEG using ROC-r analysis. We applied this method to pre-surgical mapping of primary sensorimotor cortex by using identical stimulation paradigms in MEG and fMRI, including both a group of healthy controls and a demonstrative patient case. For the patient volunteer, we demonstrated the non-invasive mapping results by comparison with electrophysiological measurements performed during surgery. Importantly, by using data-driven analysis pipelines, we reduce the potential for missing important activation due to sub-optimal pre-processing strategies. Furthermore, by working within an automated analysis environment, we eliminate the need for expert intervention in the process. By introducing a common framework for optimization of fMRI and MEG pre-processing pipelines, we ensure that comparisons of the fMRI and MEG results are not biased due to poor choices in the data analysis chain.

6.4 Methods

6.4.1 Processing Pipeline Optimization

ROC-r analysis was used for pre-processing pipeline optimization and adaptive thresholding of both fMRI and MEG maps. ROC-r measures reliability by calculating the amount of overlap in the active/inactive regions of test-retest maps as a function of analysis threshold. This is summarized by plotting the ROC area-under-the-curve (AUC) as a function of image threshold (Figure 6.1). To permit ROC-r analysis, three runs of the functional task were performed within both the fMRI and MEG sessions, and all six pairings (i.e. all combinations of each of the three images as template for the other two) of the three runs were submitted to a ROC-r analysis. This produced six AUC plots for each pre-processing pipeline (see below) applied to the data. While more repetitions of the functional task could have been used to further average the ROC-r estimates, three repetitions provided adequate balance between convergence and scanning time. The ROC-r methodology is described in detail in Stevens *et al.* [141].

The reliable-fraction (F_R) metric was used to measure overall test-retest reliability from the AUC versus threshold plots. This is calculated as the fraction of the threshold range for which the AUC is above its mid-range (i.e. $0.5[AUC_{max}+AUC_{min}]$, see Figure 6.1). Reliable fraction is bounded by 0 and 1, with high values indicating that reliability increases quickly with image threshold. The reliable fraction was calculated for the six test-retest pairings, and an average for each pipeline was determined. The pipeline with the highest reliable fraction was selected on a subject specific basis. At the group level, differences between the pipelines were assessed using ANOVA ($p < 0.01$).

After pipeline optimization, ROC-r adaptive thresholds were determined for each MEG and fMRI map. The thresholds were selected from the AUC plots as the lowest threshold with an AUC above the mid-range, and a rate of AUC increase below the ‘linear rate’ (i.e. $[AUC_{max}-AUC_{min}]/[t_{max}-t_{min}]$). This provides a balance between the high test-retest reliability and high sensitivity, by avoiding the diminishing returns in reliability at high thresholds (Figure 6.1). The ROC-r thresholds were determined for each of the six test-retest pairings, and the average threshold was applied to

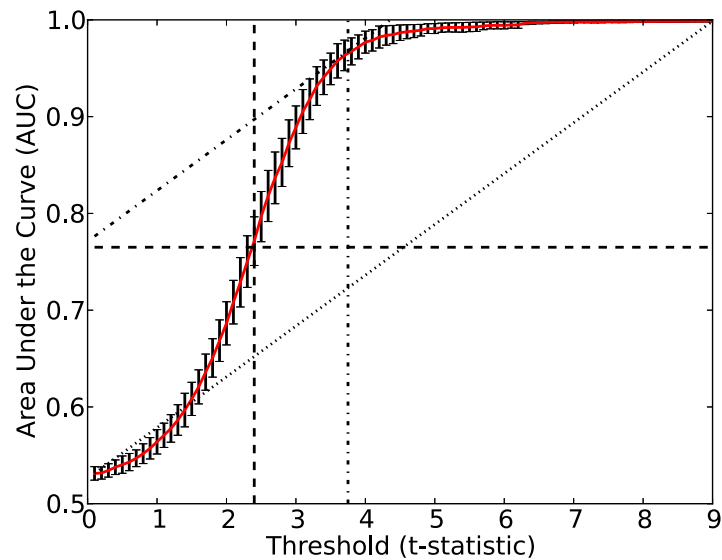


Figure 6.1: Schematic of the ROC-r output parameters. The mean \pm standard deviation of the AUC versus threshold for the six image pairings is shown (solid line with error bars), along with the mid-range value (dashed lines) and the ‘linear-rate’ (dotted line). The ROC-r optimized threshold is identified as the lowest threshold for which the AUC is above the mid-range, and the rate of AUC increase drops below the linear-rate (dash-dotted lines).

the average of the three maps to produce a final activation map. To demonstrate robustness, the thresholded maps were transformed into standard space, and the number of single-subject datasets that identified activity in each voxel was summed. Areas with high values in this group overlap map were thus consistently detected across subjects.

6.4.2 Subjects

Twenty healthy controls (33 ± 13 years of age; 12 females; 17 right handed) volunteered for this study. All participants provided informed consent, and the study was performed in compliance with the local research ethics board (Capital District Health Authority REB, Halifax, NS). A patient case with planned intraoperative electrical stimulation mapping was also studied to demonstrate the application of these methods to pre-surgical mapping directly. All participants performed within-session test-retest fMRI and MEG imaging, and the order of the two modalities was counterbalanced

across subjects.

6.4.3 Stimulation Paradigm

Both MEG and fMRI mapping were performed using an identical stimulation paradigm for localization of the primary sensorimotor cortex. The task consisted of word pairs presented in serial order, which were either semantically related (50%) or unrelated (50%) to one another. The subjects were asked to respond by squeezing their left or right hand for related and unrelated word-pairs respectively, using a grip-force response device. The task was presented in a series of six task (40 s) and seven rest (20 s) blocks, for a total time of 6 minutes 20 seconds. The task blocks were made longer than the rest blocks in order to increase the number of stimuli per run, which increases the SNR of the MEG evoked responses (see below). Within each task block, 15 word-pairs were presented, with each word appearing for 600-800 ms, and a 900-1800 ms inter-stimulus interval (ISI) between word pairs. The duration of the stimuli, the ISIs, and the order of the related/unrelated pairs were randomized to avoid anticipatory effects. The rest blocks consisted of simple fixation on a central target. The task was repeated three times within each session to facilitate ROC-r analysis. No words were repeated across the task repetitions.

6.4.4 MRI Acquisition

Participants were scanned using a 4 Tesla MRI system (Varian INOVA). Anatomical scans were acquired using a T1-weighted MP-FLASH sequence (TE = 5 ms; TR = 11 ms; 256 x 256 x 128 grid at 1 x 1 x 2 mm resolution). Functional scans used a spiral pulse sequence (TE = 15 ms; TR = 2 s; $\alpha = 60^\circ$; 64 x 64 x 31 grid at 4 x 4 x 3.5 mm resolution; 0.5 mm slice gap). The grip-force device was recorded from continuously to monitor participants' responses. Deviations from baseline greater than 10% of the device's dynamic range were marked as response events.

6.4.5 MRI Processing

The anatomical MRI was segmented using Freesurfer [189]. The resulting brain-only image was used for registration with the fMRI data, and the outer head surface was subsequently used to setup the MEG forward solution. Functional MRI registration

used within-run rigid body motion correction, followed by between-run rigid body alignment, and finally affine transformation to register to individual anatomical space.

Functional MRI maps were produced using the general linear model (GLM) approach with FSL software [190]. Eight fMRI pre-processing pipelines were investigated, including: 1) using the stimulus (related vs. unrelated pairs) or response (left vs. right hand squeeze) timing for GLM analysis, 2) with or without motion parameter regression in the GLM, and 3) with or without auto-correlation correction (ACC). Both GLM contrast choices were designed to produce a single image in which the left and right hand appeared as positive and negative task correlation respectively, in order to produce maps with high specificity to the primary sensorimotor cortices. The related versus unrelated word stimuli contrast is only expected to work well when subjects' response accuracy is high. All pre-processing pipelines used a 6 mm FWHM smoothing kernel and a 100 s high-pass filter. Each pre-processing pipeline was analyzed with ROC-r, and the pipeline with the highest reliability was chosen.

6.4.6 MEG Recording

Head position was monitored during MEG scanning using head position indicator (HPI) coils placed on the left/right temples and mastoids. The head surface, HPI coil locations, left/right pre-auricular points, and the nasion were digitized using an Isotrak system (Polhemus Inc., Colchester, USA). Surface electrodes pairs were placed above and below the left eye to record eye blinks, and on the left and right flexor carpi radialis to record the EMG at movement onset. MEG data were collected at 1000 Hz sampling frequency, using a Neuromag (Elekta AB, Stockholm, SE) 306 channel whole-head system. The grip-force device was recorded from continuously, as in the fMRI experiment. HPI coils were recorded continuously to monitor head movement during the MEG scans.

6.4.7 MEG Processing

MEG data were band-pass filtered (1-60 Hz), and down-sampled to 500 Hz. The following pre-processing pipeline choices were analyzed using ROC-r analysis: 1) with or without independent component analysis (ICA) for removal of artifacts, 2) epoch extraction relative to either force onset or EMG onset, and 3) with or without

an additional low-pass filter (20 Hz). Force onsets were detected by thresholding the grip-force signal at 10% maximum, and EMG onset detection additionally employed a band-pass filter (2-4 Hz) after rectification, in order to isolate the envelope of the EMG signal. For ICA denoising, components were removed if they satisfied any of the following conditions: a) correlation greater than 0.4 with the vertical eye electrode signal, b) frequency matching the heart rate range, or c) amplitude outside of the physiological range (i.e. greater than 7.5×10^{-11} Tesla/cm for planar gradiometers or 2×10^{-12} Tesla for the magnetometers).

Source mapping was performed using a dynamic (i.e. 3D+time) beamformer. Epochs were extracted for the left and right hand separately from -1000 ms to +500 ms relative to the EMG/force onset triggers. Unlike the fMRI analysis, this procedure produces independent images of the left and right hand, as specificity of the MEG maps can be achieved by exploiting the temporal resolution. Epochs were baseline corrected for -1000 to -500 ms, and the baseline covariance was calculated from the same time range. Sensor covariances for the active period were taken from the -100 to +100 ms window for the force-triggered epochs and +100 to +300 ms for the EMG trigger, as the largest evoked field was observed near the center of these latency ranges. The forward solution was calculated according to the boundary element method (openMEEG software), using the external head surface boundary produced during Freesurfer segmentation. The MEG and anatomical data were registered semi-manually (manual alignment to Isotrak anatomical landmarks, followed by iterative closest point registration of the head shape). Within this head-shaped boundary, a 4 mm grid was constructed, and the beamformer solution was calculated for each location on this grid, matching the spatial resolution used in the fMRI acquisition. The latency with the largest source amplitude in the pre- or post-central gyri was extracted as the final source map.

6.4.8 Intraoperative Mapping

For the patient case, intra-operative mapping was also performed to validate the non-invasive techniques. A linear strip of six subdural electrodes was used both for detecting phase reversal of sensory evoked potentials in response to electrical stimulation of the contralateral ulnar nerve, and to elicit EMG activity in the abductor digiti

minimi or adductor hallucis brevis by stimulating between pairs of electrodes (2-10 mA, 60 Hz, 0.5 ms pulses). Results of the intraoperative mapping were recorded onto the patient’s pre-surgical MRI image using a StealthStation (Medtronic, Minneapolis, USA) neuro-navigation system.

6.5 Results

We successfully mapped the primary motor cortex by both fMRI and MEG in the majority of subjects. Four subjects were excluded, due either to compliance issues during scanning ($N = 3$) or incidental findings on the MRI in the vicinity of the motor cortex ($N = 1$). Reliability of the fMRI and MEG maps was generally high, although more strongly dependent on the pre-processing pipeline for MEG. After pipeline optimization, the reliability of fMRI ($F_R = 0.69 \pm 0.02$) and MEG maps were similar ($F_R = 0.71 \pm 0.03$). ROC-r automated thresholding produced robust localization of the primary motor cortex for both fMRI and MEG in the majority of healthy controls, and this localization was confirmed in a patient case using intra-operative electrocortical mapping methods.

6.5.1 Pre-processing Optimization

On average, there was no significant difference in reliability between the fMRI pipelines (Figure 6.2a). However, the pipeline using the response-based GLM, with ACC but without MPR, had the highest reliability more than twice as often as any other pipeline (Figure 6.2b). Seven of the eight fMRI pre-processing pipelines were optimal for at least one of the 16 healthy control datasets. There was a clear tendency for the response-based GLM model to provide more reliable maps than the stimulus-based model (13/16), as the stimulus based model assumes response accuracy, and is less time-locked to the responses. While accuracy was in general high (95 ± 5 percent), the response based model was still superior in general. The use of ACC (10/16) or MPR (6/16) produced more equivocal results, suggesting that despite their common use in fMRI analysis pipelines, neither are universally beneficial to the production of robust fMRI maps.

For MEG, 7/8 pipelines tested were optimal for at least one dataset. Maps using the force-onset trigger were significantly more reliable ($F_R = 0.57 \pm 0.02$) than those

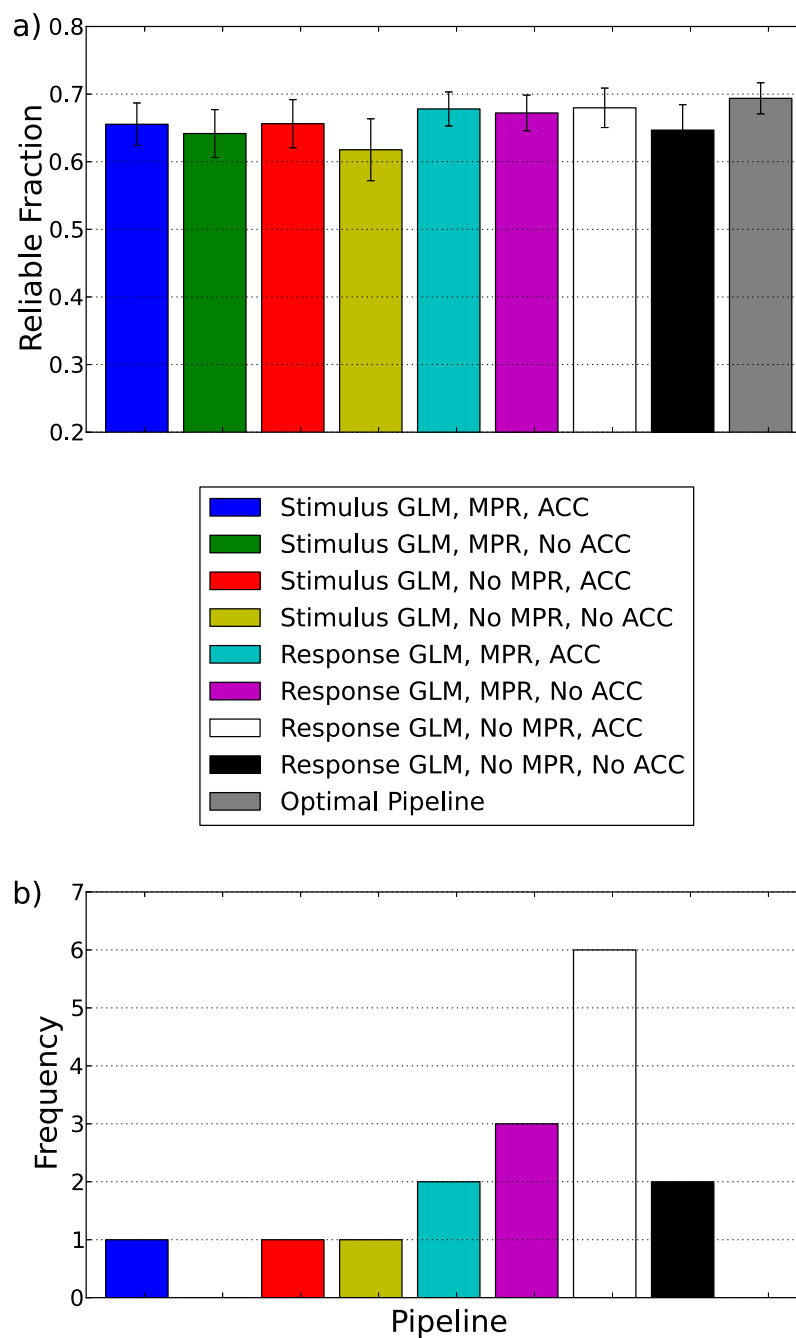


Figure 6.2: a) Average reliability of the fMRI maps by pre-processing pipeline. There was no significant difference between the pre-processing pipelines at the group level for fMRI. b) The number of individual fMRI datasets for which each pipeline had the highest ROC-r F_R . At the individual level the best pre-processing choices were highly subject dependent, and all but one pipeline was optimal at least once. The response-based GLM was best in the majority (13/16) of datasets, whereas other pre-processing options produced more variable results.

produced using the EMG-onset trigger ($F_R = 0.39 \pm 0.02$). However, pipelines using the EMG-onset trigger were optimal for 7/32 datasets (Figure 6.3). Pipelines with ICA artifact removal produced significantly lower reliability (0.45 ± 0.02) than those without ICA (0.51 ± 0.02), and ICA was rarely selected by individual-level pipeline optimization (5/32). Pipeline optimization improved the reliability significantly compared to any of the fixed analysis pipelines ($p < 0.05$). The most common optimal pipelines for the MEG data thus used the force-onset trigger, without ICA artifact removal, with (8/32) or without (13/32) low-pass filtering.

6.5.2 Automated Thresholding

A representative automated thresholding result is shown in Figure 6.4. ROC-r thresholds maps identified activity around the central sulcus for all 16 fMRI maps, 13/16 left hand MEG maps, and 15/16 right hand MEG maps. The datasets which failed to identify activity had significantly lower reliability (0.48 ± 0.05 vs. 0.78 ± 0.03). In one case, this was associated with a moderate amount of subject motion (~ 1 -2 mm), but in other cases we could determine no obvious explanation. Threshold levels were much higher for fMRI (4.0 ± 0.3) than MEG (0.22 ± 0.06), as the two modalities used different statistical measures (z-statistic versus pseudo-z), with different magnitude scales. For MEG, localization was consistent with the primary motor cortex in the pre-central gyrus, whereas the fMRI activity tended to localize just posterior to the hand knob, in the primary sensory cortex of the post-central gyrus (Figure 6.5). MEG locations were somewhat more variable than fMRI, resulting in lower between-subject overlap for MEG (80%) than fMRI (88%).

6.5.3 Patient Case

A right handed female patient (56 years of age) with a tumor in the left supplementary cortex performed the same fMRI and MEG protocol, to demonstrate the validity of the automated ROC-r processing approach in the context of intra-operative stimulation mapping. The patient presented with seizures involving repetitive speech and expressive aphasia. Complete resection of the tumor was achieved during surgery, after which the patient experienced transient aphasia and right hemiparesis. The patient was discharged two weeks after surgery, and underwent six weeks of rehabilitative

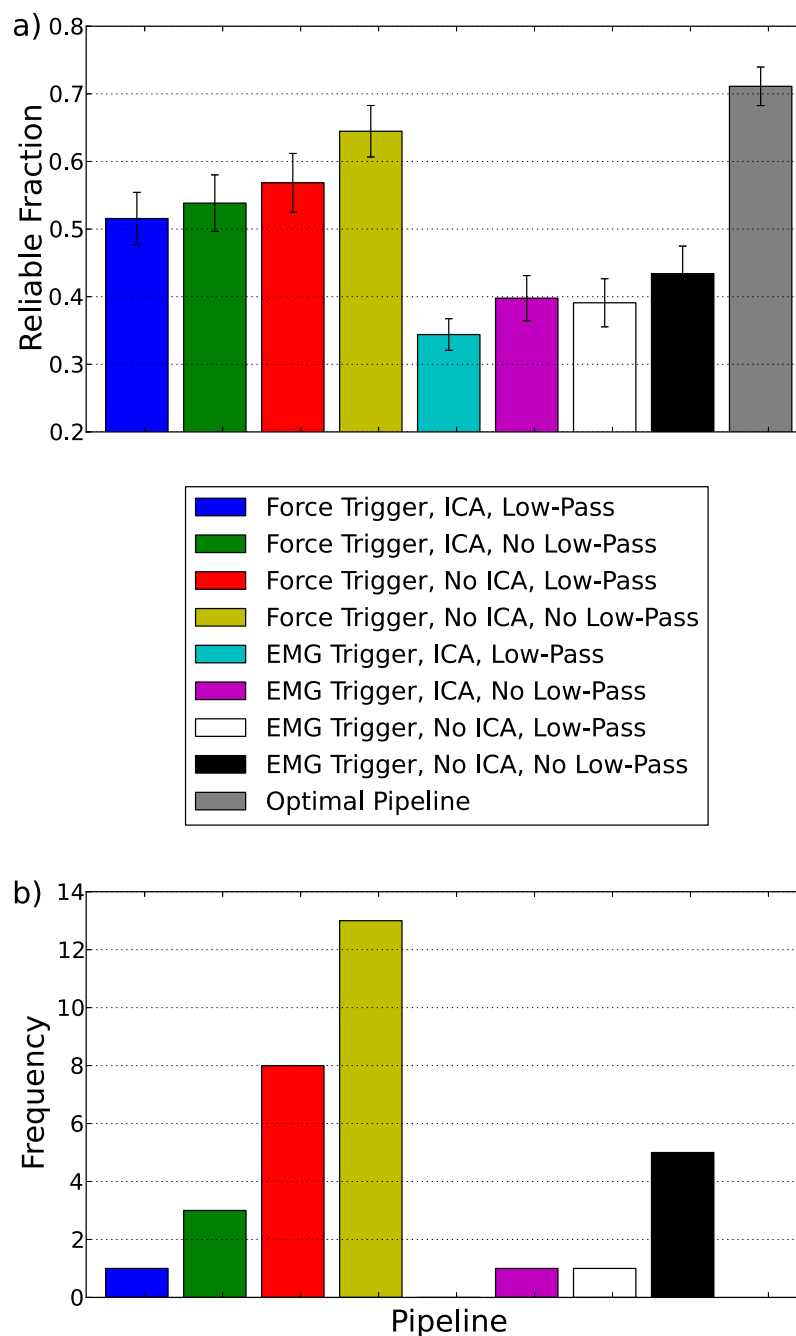


Figure 6.3: a) Average reliability of the MEG maps by pre-processing pipeline. Force-onset triggering produced more reliable results than EMG-onset triggering, and ICA artifact removal was associated with a decrease in reliability of MEG maps. Pipeline optimization provided a significant improvement in reliability across the group. b) The number of individual MEG datasets for which each pipeline had the highest ROC-r F_R . The force-onset triggered pipelines were best in the majority (25/32) of datasets, and ICA denoising was recommended rarely (5/32 datasets), in agreement with the overall reliability trends.

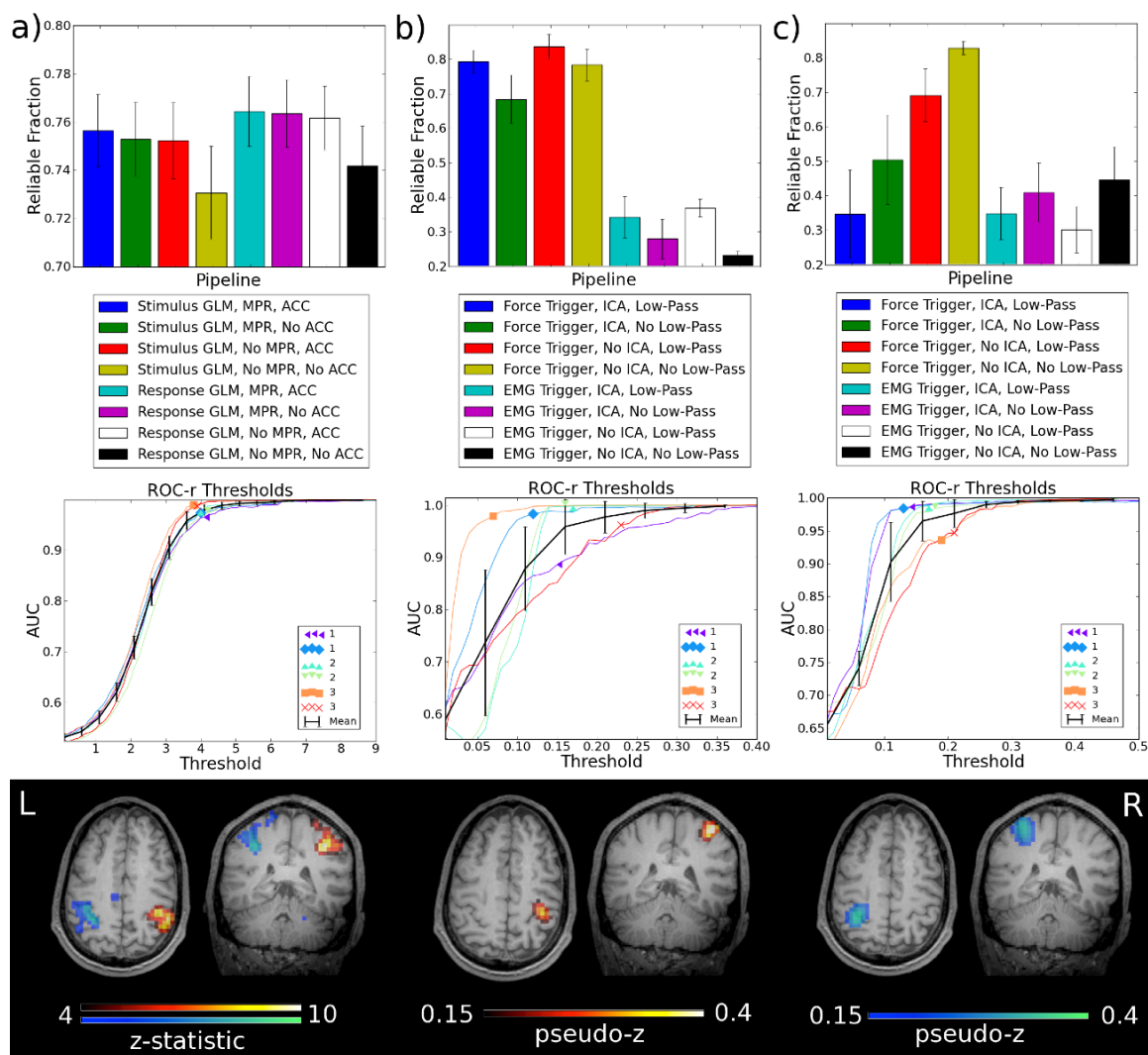


Figure 6.4: Single-subject ROC-r reliable fraction averaged across image pairings (top), automated threshold selection (middle), and the resulting activation maps (bottom). The fMRI contrast used (left vs right hand) produced a single map with activity in both hemispheres (a), whereas for MEG the left (b) and right (c) hand epochs were mapped separately. For fMRI, the best pipeline in this case used the response-based GLM, with MPR and ACC corrections. For MEG, the best pipeline was different for the left hand (force trigger, without ICA but with low-pass filtering) and right hand (force trigger, with neither ICA nor low-pass filtering). Both the fMRI and MEG activation in this subject straddled the central sulcus, at the level of the hand-knob.

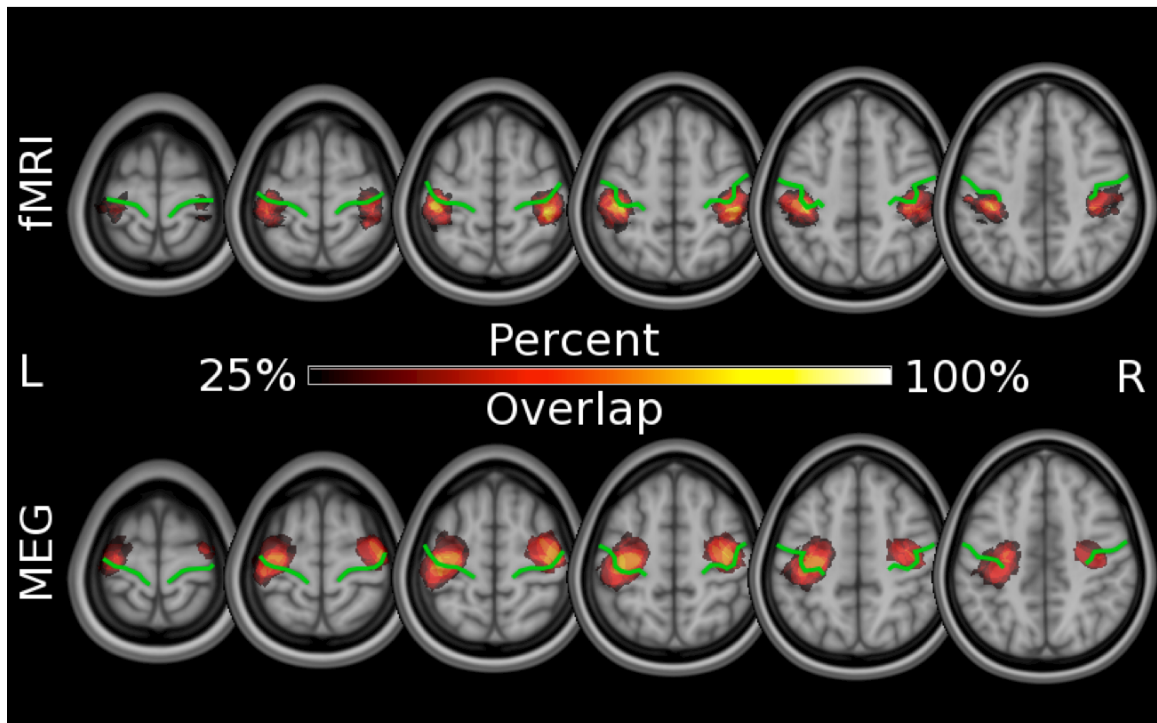


Figure 6.5: Group overlap of individual-level maps for both the left and right hands. The peak overlap was higher for fMRI maps (88%) than MEG maps (80%). While both peaks occurred near the ‘hand knob’ area of the central sulcus, the fMRI peak occurred in the post-central gyrus, whereas the MEG peak occurred in the pre-central gyrus. The central sulcus is highlighted in green.

work, after which the post-operative deficits were essentially resolved. Histopathology identified the tumor as a WHO grade II oligoastrocytoma.

Intra-operative mapping with electrocortical stimulation produced right abductor digiti minimi and adductor hallucis brevis activity when the most posterior pair of sub-dural electrodes were stimulated at 8.5 mA (Figure 6.6). In recording mode, phase reversal was observed between the same pair of electrodes upon ulnar nerve stimulation, confirming the location of the right hand on the central sulcus. The ROC-r optimized fMRI and MEG maps both produced focal activation straddling the central sulcus and directly underlying the intra-operative locations, demonstrating a high degree of concordance between the non-invasive and invasive mappings.

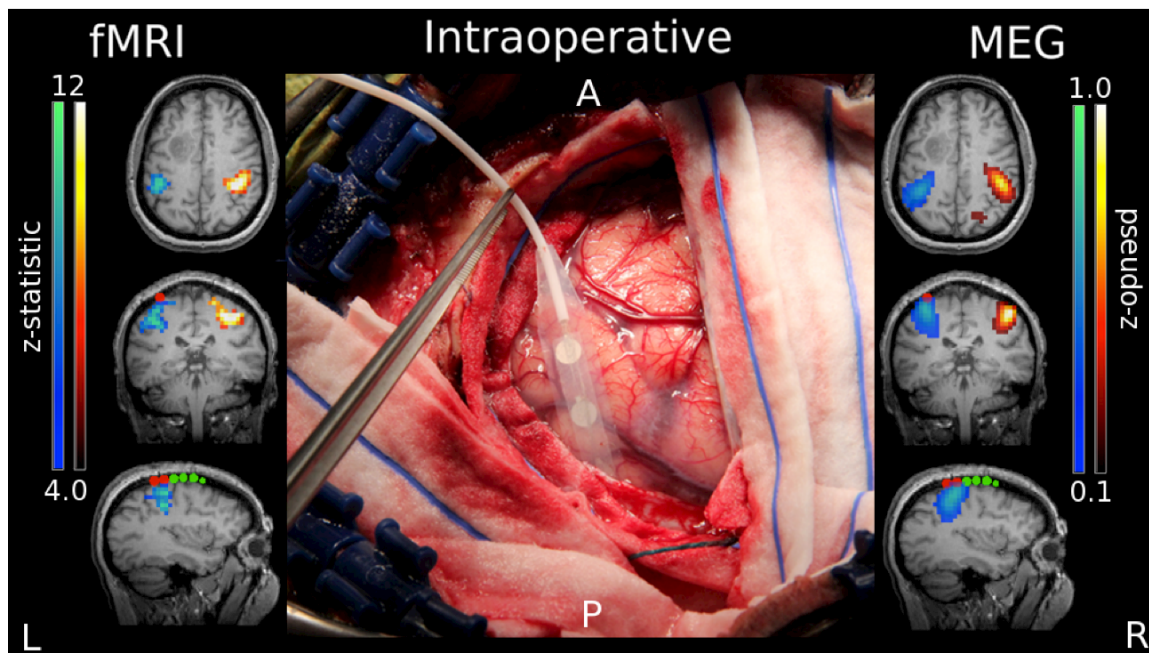


Figure 6.6: Patient case demonstrating correspondence of the non-invasive mapping results with gold-standard intraoperative measurements. The ROC-r optimized fMRI (left) and MEG (right) mapping of both the left (yellow-red) and right (blue-green) hand are shown. A strip of 6 subdural electrodes (red and green circles) was used to map the primary sensorimotor cortex intraoperatively. Electrical stimulation between the two red circles produced EMG activity in the right abductor digiti minimi and adductor hallucis brevis, and ulnar nerve stimulation produced phase reversal between the same electrode pair, thus localizing the central sulcus. The MEG and fMRI maps were highly co-localized, and both provided accurate prediction of the location of the hand representation in the primary sensorimotor cortex.

6.6 Discussion

We successfully demonstrated ROC-r analysis as a unified framework for automated optimization of subject-specific fMRI and MEG pre-processing pipelines. On average, MEG reliability was more dependent on the pre-processing pipeline than fMRI. However, pipeline optimization was still beneficial for fMRI analysis, as demonstrated by the wide variety of optimal pipelines at the single-subject level. It is known that there is an interaction between the functional task paradigm employed and the effect of pre-processing options [157,183]. Therefore, even though the use of MPR was often not recommended in our study, this likely depends on the amount of subject motion, and the degree of correlation between head motion and the task timing. Additionally,

while ICA is commonly used to remove eye-blink artifacts from MEG data, we did not observe obvious eye blink artifacts in the evoked responses in our study, and ICA was not usually recommended. Using ROC-r for pipeline optimization, ambiguity in the best approach for a particular dataset can be resolved directly in terms of reliability of the resulting maps. The adoption of data-driven pre-processing pipelines facilitates comparisons between fMRI and MEG results, as the best results of each modality are put forward.

Using explicit evaluation of pre-processing pipelines, we found that some commonly employed analysis strategies were not recommended for our data. For example, averaging to force-onset was generally preferable to averaging to EMG-onset for the MEG source mapping. This is contrary to the methodology typically employed in mapping primary motor cortex in MEG studies [32,191], which usually employ EMG triggering. Partly, this discrepancy may be related to small oscillations on the EMG signal that were observable approximately 100-200 ms prior to the force onset, likely caused by anticipatory pre-movement muscle activity. Furthermore, some subjects had difficulties relaxing their muscles completely between stimuli, resulting in some tonic activity on the EMG sensors. These undesired oscillations made the detection of EMG onset more dependent on the specific frequency filter and threshold used to define the trigger, and introduced variability in the trigger latencies. The fidelity of the grip-force signal was higher, making it more robust for detecting the latency of force-onset. This further illustrates the importance of quantitative evaluation of pre-processing choices, as the best results are highly dependent on the details of the task paradigm, data acquisition, and subject performance.

The pipelines investigated here only represent a small fraction of the potential pre-processing choices that are made routinely during analysis of fMRI and MEG images. Inevitably there are other fMRI pre-processing choices that will have a more significant impact on reliability, and these need to be assessed on a case-by-case basis. Ultimately, the more pipelines included in a ROC-r analysis, the greater the potential benefit in terms of activation reliability.

ROC-r analysis not only determines optimal subject-specific pre-processing pipelines,

but also produces data-driven thresholds for automated localization of activated regions. In many cases, the thresholded fMRI and MEG maps overlapped in the ‘hand-knob’ of the primary motor cortex, however the MEG maps tended to reach maximum in the pre-central gyrus (the primary motor cortex), whereas the fMRI maps tended to peak in the post-central gyrus (the primary somatosensory cortex). This discrepancy is likely due to sensory feedback from the hand-squeeze combined with the low temporal resolution of fMRI compared to MEG. The slow hemodynamic response of fMRI essentially acts as a low-pass temporal filter, taking up to six seconds to peak. As the motor cortex activation and subsequent sensory feedback are likely to occur in very close succession, these signals cannot be distinguished from one another by fMRI. The forceful hand-squeeze movement used in this study is particularly likely to evoke a strong sensory response. In contrast, the millisecond temporal resolution of MEG produces motor and sensory signals that are easily separated in the evoked response. Additionally, with the evoked responses being time-locked to the EMG or grip-force signal, the later sensory response is less likely to produce a strong average due to latency variability.

Both fMRI and MEG were generally successful at identifying the primary sensorimotor cortex, as demonstrated explicitly with the patient case presented. In this case, we were able to identify with high specificity the hand representation in the primary sensorimotor areas. This case showed that, although at the group level there were slight differences in the fMRI and MEG localization, in individual subjects this was not necessarily true. The recommendation of one scanning modality or the other would likely be decided by patient-specific details rather than the differences in localization (e.g. in the case of a high grade glioma, fMRI contrast may be affected [56, 192, 193], rendering MEG preferable). This may not generalize to other task paradigms, as fundamental differences in fMRI and MEG sensitivity may come into play (e.g. lack of sensitivity to radial sources in MEG or difficulty imaging near air-tissue interfaces in fMRI). ROC-r provides an objective means of determining which areas are reliably detected, which provides guidance for recommending scanning modalities for pre-surgical mapping.

The automated thresholding algorithm provided robust localization at the single-subject level. The few MEG datasets in which localization was not possible had

very low reliability even for the best available pre-processing pipelines. This is likely a reflection on the data quality for these datasets, as the evoked responses were weak in these cases, possibly because of the relatively low number of stimuli used in this study. Ongoing work by many research groups improving task paradigms, acquisition strategies, and analysis procedures will ultimately improve the quality of activation maps, making ROC-r an even more valuable tool for pipeline optimization and automated localization.

By providing the best data analysis chain for a given dataset, and automatically thresholding to include only reliably detected brain areas, ROC-r allows for comparison of fMRI and MEG localization on equal footing. This is beneficial both for comparing experimental techniques in healthy controls, and for optimizing results in the clinical setting, where producing the highest quality results is most important.

6.7 Conclusion

ROC-r analysis uses quantitative reliability measures to achieve fully automated activation mapping, including pipeline optimization and image thresholding, on a single subject basis. ROC-r provides a critical tool for non-invasive pre-surgical mapping, as it allows for subject-specific processing strategies without the need for manual intervention. This reduces the risk of missing important functional activity due to sub-optimal analysis strategies, eliminates the influence of subjective decision making in the production of activation maps, and streamlines the process for integration into a clinical setting. We demonstrated ROC-r as a unified framework for push-button fMRI and MEG studies, thus dramatically improving our ability to study relative differences in pre-surgical functional neuroimaging technologies, and ensuring the best possible pre-surgical maps are produced.

Chapter 7

Conclusions

7.1 Summary

The purpose of this thesis was to evaluate the benefit of ROC-r analysis for improving the production of single-subject activation maps. First, it was shown in manuscript one (ch. 3) that the reliability of single-subject maps is highly dependent on the threshold used and on the pre-processing steps employed. This is of course a large part of the motivation for performing individualized analysis for single-subject mapping. Nonetheless, it is important to demonstrate that the tool we plan to use to address the issues of individual variability is sensitive to differences between subjects, task repetitions, and pre-processing pipelines. ROC-r thresholding was shown to be responsive to different levels of activation between subjects or within subjects between runs, and the first use of ROC-r to select subject-specific pre-processing strategies was demonstrated to improve activation reliability. The high degree of variability at the single-subject level is inherent given the noisy nature of fMRI and MEG signals, and cannot be ignored without jeopardizing the quality of the activation maps.

One of the greatest strengths of the ROC-r method is the minimal assumptions placed on the underlying data distributions. The basic assumptions are simply: 1) the image signal is higher in amplitude than the noise, and 2) that the signal is consistently located in space whereas the noise is not. Additionally, the ROC-r calculation only requires functional maps as input, and because the functional map forms the common link between fMRI and MEG imaging, ROC-r is by nature cross-modal. It is worth noting that it is crucial in this context that the MEG source images are noise-normalized, as the sensor noise projects non-uniformly in space, with higher noise projecting in areas of high sensor sensitivity (e.g. near the sensors). This would invalidate the second assumption of the ROC-r method, and thus in this work, only noise-normalized MEG source maps were used.

In manuscript two (ch. 4), we demonstrated the ROC-r method for MEG volumetric source imaging with a noise-normalized beamformer. We showed that the ROC-r reliable fraction provided analogous quality assurance to the equivalent current dipole goodness-of-fit used for dipole source models. Furthermore, we verified the automated thresholding and localization of MEG signals by ROC-r by co-localization of the beamformer peaks with the dipole locations.

The primary application of ROC-r analysis we have identified is pre-surgical mapping, where single-subject imaging is clearly necessary. While there are other instances where single-subject imaging is important - such as the assessment of brain injury - we used the pre-surgical mapping scenario in manuscript three (ch. 5) to demonstrate the tangible benefits of using the ROC-r methodology. This section of the thesis showed that reliability of patient images is generally lower than that of healthy controls, either due to direct influence of pathology on the functional imaging signal, or due to factors affecting patient performance of the tasks. ROC-r pre-processing pipeline optimization was able to improve reliability of the patient data, even using the limited number of pre-processing pipelines investigated.

Crucially, this paper showed that the ROC-r reliable fraction was correlated with better prediction of critical eloquent cortex, and that ROC-r automated thresholding was better at localizing these critical brain regions than fixed-significance levels. While the more reliable datasets on average produced activation closer to the critical cortical areas, it was still necessary to use moderate search ranges (10-15 mm) around each CS location to achieve high sensitivity. This suggests that the fMRI protocols demonstrated in this thesis are better suited to an augmentative pre-surgical mapping role than as a direct replacement to CS. It is likely that the motor maps would achieve higher sensitivity at lower search ranges than the language maps, but there was not sufficient data available to test this hypothesis quantitatively. While there is still substantial room for improvement of the predictive power of fMRI for presurgical mapping of language in particular, the ROC-r method helps to get the most out of the available data.

The final manuscript (ch. 6) included in this thesis showcased the capabilities of ROC-r analysis as a unified framework for improving the reliability of single-subject fMRI and MEG mapping. This paper brings together the facets introduced by each

of the preceding papers by including quality assurance, pre-processing optimization, and automated threshold selection for functional mapping by both modalities. As this paper shows, the use of fixed pre-processing pipelines could misleadingly conclude that one scanner produces more reliable results than the other, whereas in reality these data could produce reliable activation maps with the use of alternative processing strategies. While it was true for that experiment that the fMRI results were on average less sensitive to the pre-processing pipeline chosen, this result depends on the task employed and participant population being investigated (e.g. patients vs controls). ROC-r thus facilitates the comparison of fMRI and MEG results by ensuring that the best available methods are selected for processing each dataset individually.

7.2 Future Work

Further improvements of the ROC-r algorithm will initially focus on the generation of single-run analyses. Single-run ROC-r was demonstrated in manuscript two for MEG datasets by generating split-half maps from half of the available epochs and iterating over different randomized split-halves. A similar technique for single-run ROC-r using fMRI data is being developed and will offer the enhanced pre-surgical mapping capabilities of the ROC-r analysis, without the additional data collection requirements of retest imaging. An additional benefit of the single-run version is the ability to perform reliability analyses in real-time, with the potential to inform the acquisition system when a robust activation map had been obtained. This would allow individually tailored scan durations, thereby reducing scanning times. Ultimately, ROC-r is intended as a clinical utility, and thus would ideally be either directly integrated into the acquisition console, or implemented on the post-processing station, in order to automate the processing of activation maps into a format ready for review (e.g. by the radiologist, neuropsychologist, neurosurgeon, etc.).

For MEG, an important avenue for future research will be to compare the results of ROC-r for beamformer mapping to imaging approaches like dSPM, sLORETA and MNE. There are interesting questions to address in this context in terms of the relationship between mapping reliability and localization accuracy. In particular, the MNE solution is generally accepted as being quite robust, however it tends to have a

localization bias towards superficial locations, due to the MEG sensor sensitivity profile [78]. When cortical stimulation (which is generally restricted to surface mapping) is used as the ‘gold standard’ for localization, this may result in better co-localization for MNE solutions, even when the true sources are located deeper within the cortical sulci. Additionally, there are many inverse solution constraints that were not employed in this work, such as restriction of sources to the cortical grey matter, and constraints on source orientation to be normal to the cortical surface. The effect of these additional *a-priori* localization constraints on the reliability and accuracy of MEG mapping should be explored in the future.

Another area of future investigation will be the use of ROC-r for functional connectivity analyses and resting state functional mapping. For example, components of interest in a decomposition-based resting state analysis (e.g. ICA) could be identified using ROC-r by comparing them with a number of pre-defined activation templates (e.g. derived by a group analyses of task-based mapping). The most similar ICA component to a given functional network could be determined as the one with the highest ROC-r F_R .

Modelling of the ROC-r output also deserves further attention, as the method of cubic spline fitting, while robust, does not produce meaningful fitting parameters. One option would be to use a Gompertz function ($g(x)$):

$$g(x) = a + be^{-ce^{-dx}} \quad (7.1)$$

which is widely used for fitting data that has a general sigmoidal shape. The parameters of this function allow for varying the initial (a) and final (b) values, along with the point at which the AUC begins to increase (c), and the rate of increase (d). Alternatively, a functional form could be derived by modelling the underlying statistical distributions, and computing a theoretical form for the true and false positive rates. In this case, the parameters governing the final result will be the mean activation/deactivation/noise magnitudes and variances. This would have the added advantage of being able to use the intensity distributions in the images (i.e. the image histograms) to inform the curve fitting process. Either of these choices would confer the advantage of producing curve fitting parameters that are meaningful in terms of understanding the underlying data, or determining the image reliability and

informing the choice of activation thresholds.

Finally, while several reference standards were used in this thesis to evaluate the efficacy of the ROC-r approach to activation mapping (e.g. dipole fitting for MEG, cortical stimulation as 'ground truth', etc), it would be important moving forward to assess patient outcomes. Patient outcomes are likely the best gold standard for determining whether pre-surgical mapping successfully identified the key areas to respect during surgery, as the ultimate test of whether these functions were spared or not.

7.3 Conclusion

Overall, this thesis has demonstrated the utility of ROC-r analysis for reliable single-subject functional mapping. The ROC-r method addresses the issue of individual variability by producing a flexible solution to the selection of both individualized pre-processing pipelines and activation thresholds. ROC-r also eliminates inter-rated variability, as the production of activation maps is a fully automated process. The production of robust, push-button single-subject mapping is a vital step forward for fMRI and MEG, especially in the context of pre-surgical mapping.

References

- [1] Perry Black. Management of malignant glioma: role of surgery in relation to multimodality therapy. *Journal of NeuroVirology*, 4:227–236, 1998.
- [2] Ashok R. Asthagiri, Nader Pouratian, Jonathan Sherman, Galal Ahmed, and Mark E. Shaffrey. Advances in brain tumor surgery. *Neurologic Clinics*, 25(4):975–1003, 2007-11.
- [3] Nader Sanai and Mitchel S. Berger. Recent surgical management of gliomas. In *Glioma*, pages 12–25. Springer, 2012.
- [4] Ilker Y. Eypoglu, Michael Buchfelder, and Nic E. Savaskan. Surgical resection of malignant gliomas role in optimizing patient outcome. *Nature Reviews Neurology*, 9(3):141–151, 2013-01-29.
- [5] Ashok R. Asthagiri, Gregory A. Helm, and Jason P. Sheehan. Current concepts in management of meningiomas and schwannomas. *Neurologic Clinics*, 25(4):1209–1230, 2007-11.
- [6] Hugues Duffau and Laurent Capelle. Preferential brain locations of low-grade gliomas: Comparison with glioblastomas and review of hypothesis. *Cancer*, 100(12):2622–2626, 2004-06-15.
- [7] Wilder Penfield and Edwin Boldrey. Somatic motor and sensory representation in the cerebral cortex of man as studied by electrical stimulation. *Original Articles and Clinical Cases*, pages 389–444, 1937.
- [8] Wilder Penfield. Some observations on the functional organization of the human brain. *Proceedings of the American Philosophical Society*, pages 293–297, 1954.
- [9] Wilder Penfield and Phanor Perot. The brains record of auditory and visual experience a final summary and discussion. *Brain*, 86(4):595–696, 1963.
- [10] R. Andrew Danks, Linda S. Aglio, Lavern D. Gugino, and Peter McL Black. Craniotomy under local anesthesia and monitored conscious sedation for the resection of tumors involving eloquent cortex. *Journal of neuro-oncology*, 49:131–139, 2000.
- [11] Nader Sanai, Zaman Mirzadeh, and Mitchel S. Berger. Functional outcome after language mapping for glioma resection. *New England Journal of Medicine*, 358(1):18–27, 2008.
- [12] H. Duffau. Contribution of cortical and subcortical electrostimulation in brain glioma surgery: Methodological and functional considerations. *Neurophysiologie Clinique/Clinical Neurophysiology*, 37(6):373–382, 2007-12.

- [13] Svenja Borchers, Marc Himmelbach, Nikos Logothetis, and Hans-Otto Karnath. Direct electrical stimulation of human cortex: the gold standard for mapping brain functions? *Nature Reviews Neuroscience*, 13(1):63–70, 2011.
- [14] Alfredo Quiones-Hinojosa, Steven G. Ojemann, Nader Sanai, William P. Dillon, and Mitchel S. Berger. Preoperative correlation of intraoperative cortical mapping with magnetic resonance imaging landmarks to predict localization of the broca area. *Journal of neurosurgery*, 99(2):311–318, 2003.
- [15] S. Ogawa, R. S. Menon, D. W. Tank, S. G. Kim, H. Merkle, J. M. Ellermann, and K. Ugurbil. Functional brain mapping by blood oxygenation level-dependent contrast magnetic resonance imaging. a comparison of signal characteristics with a biophysical model. *Biophysical journal*, 64(3):803–812, 1993.
- [16] Suzanne Tharin and Alexandra Golby. Functional brain mapping and its applications to neurosurgery. *Neurosurgery*, 60(4):185–202, 2007.
- [17] A I Ahonen, M S Hmlinen, M J Kajola, J E T Knuutila, P P Laine, O V Lounasmaa, L T Parkkonen, J T Simola, and C D Tesche. 122-channel squid instrument for investigating the magnetic signals from the human brain. *Physica Scripta*, 1993(T49A):198, 1993.
- [18] W. W. Sutherling, P. H. Crandall, T. M. Darcey, D. P. Becker, M. F. Levesque, and D. S. Barth. The magnetic and electric fields agree with intracranial localizations of somatosensory cortex. *Neurology*, 38(11):1705–1705, 1988.
- [19] T.P.L. Roberts, E. Zusman, M. McDermott, N. Barbaro, and H.A. Rowley. Correlation of functional magnetic source imaging with intraoperative cortical stimulation in neurosurgical patients. *Journal of Image Guided Surgery*, 1(6):339–347, 1995.
- [20] Christopher C. Gallen, David Sobel, Thomas Waltz, Maung Aung, Brian Copeland, Barry Schwartz, Eugene Hirschkoff, and Floyd Bloom. Noninvasive presurgical neuromagnetic mapping of somatosensory cortex. *Neurosurgery*, 33(2):260–268, 1993.
- [21] Oliver Ganslandt, Ralf Steinmeier, Helmut Kober, Jurgen Vieth, Jan Kassubek, Johann Romstock, Christian Straus, and Rudolph Fahlbusch. Magnetic source imaging combined with image-guided frameless stereotaxy: A new method in surgery around the motor strip. *Neurosurgery*, 41(3):621–628, 1995.
- [22] Christopher C. Gallen, Barry J. Schwartz, Richard D. Bucholz, Ghaus Malik, Gregory L. Barkley, Joseph Smith, Howard Tung, Brian Copeland, Leonard Bruno, Sam Assam, and others. Presurgical localization of functional cortex using magnetic source imaging. *Journal of neurosurgery*, 82(6):988–994, 1995.

- [23] Takashi Inoue, Hiroaki Shimizu, Nobukazu Nakasato, Toshihiro Kumabe, and Takashi Yoshimoto. Accuracy and limitation of functional magnetic resonance imaging for identification of the central sulcus: comparison with magnetoencephalography in patients with brain tumors. *Neuroimage*, 10(6):738–748, 1999.
- [24] Oliver Ganslandt, Rudolf Fahlbusch, Christopher Nimsky, Helmut Kober, Martin Mller, Ralf Steinmeier, Johann Romstck, and Jrgen Vieth. Functional neuronavigation with magnetoencephalography: outcome in 50 patients with lesions around the motor cortex. *Journal of neurosurgery*, 91(1):73–79, 1999.
- [25] Timothy PL Roberts, Paul Ferrari, David Perry, Howard A. Rowley, and Mitchel S. Berger. Presurgical mapping with magnetic source imaging: comparisons with intraoperative findings. *Brain tumor pathology*, 17(2):57–64, 2000.
- [26] R. Firsching, I. Bondar, H.-J. Heinze, H. Hinrichs, T. Hagner, J. Heinrich, and A. Belau. Practicability of magnetoencephalography-guided neuronavigation. *Neurosurgical Review*, 25(1):73–78, 2002-03.
- [27] Hagen Schiffbauer, Mitchel S. Berger, Paul Ferrari, Dirk Freudenstein, Howard A. Rowley, and Timothy PL Roberts. Preoperative magnetic source imaging for brain tumor surgery: a quantitative comparison with intraoperative sensory and motor mapping. *Journal of neurosurgery*, 97(6):1333–1342, 2002.
- [28] Eduardo M Castillo, Panagiotis G Simos, James W Wheless, James E Baumgartner, Joshua I Breier, Rebecca L Billingsley, Shirin Sarkari, Michele E Fitzgerald, and Andrew C Papanicolaou. Integrating sensory and motor mapping in a comprehensive MEG protocol: Clinical validity and replicability. *NeuroImage*, 21(3):973–983, 2004-03.
- [29] Antti Korvenoja, Erika Kirveskari, Hannu J. Aronen, Sari Avikainen, Antti Brander, Juha Huttunen, Risto J. Ilmoniemi, Juha E. Jaaskelainen, Tero Kovala, Jyrki P. Makela, and others. Sensorimotor cortex localization: Comparison of magnetoencephalography, functional MR imaging, and intraoperative cortical mapping 1. *Radiology*, 241(1):213–222, 2006.
- [30] Elizabeth W. Pang, James M. Drake, Hiroshi Otsubo, Allison Martineau, Samuel Strantzas, Douglas Cheyne, and William Gaetz. Intraoperative confirmation of hand motor area identified preoperatively by magnetoencephalography. *Pediatric Neurosurgery*, 44(4):313–317, 2008.
- [31] Srikantan Nagarajan, Heidi Kirsch, Peter Lin, Anne Findlay, Susanne Honma, and Mitchel S. Berger. Preoperative localization of hand motor cortex by adaptive spatial filtering of magnetoencephalography data. 2008.

- [32] William Gaetz, Douglas Cheyne, James T. Rutka, James Drake, Mony Benifla, Samuel Strantzas, Elysa Widjaja, Stephanie Holowka, Zulma Tovar-Spinoza, Hiroshi Otsubo, and Elizabeth W. Pang. Presurgical localization of primary motor cortex in pediatric patients with brain lesions by the use of spatially filtered magnetoencephalography. *Neurosurgery*, 64:ons177–ons186, 2009-03.
- [33] Phiroz E. Tarapore, Matthew C. Tate, Anne M. Findlay, Susanne M. Honma, Danielle Mizuiri, Mitchel S. Berger, and Srikantan S. Nagarajan. Preoperative multimodal motor mapping: a comparison of magnetoencephalography imaging, navigated transcranial magnetic stimulation, and direct cortical stimulation: Clinical article. *Journal of neurosurgery*, 117(2):354–362, 2012.
- [34] Panagiotis G Simos, Joshua I Breier, William W. Maggio, William B. Gormley, George Zouridakis, L. James Willmore, James W Wheless, Jules EC Constantinou, and Andrew C Papanicolaou. Atypical temporal lobe language representation: MEG and intraoperative stimulation mapping correlation. *NeuroReport*, 10:139–142, 1999.
- [35] Eduardo M Castillo, Panagiotis G Simos, Vijay Venkataraman, Joshua I Breier, James W Wheless, and Andrew C Papanicolaou. Mapping of expressive language cortex using magnetic source imaging. *Neurocase*, 7:419–422, 2001.
- [36] Clifford R. Jack Jr, Richard M. Thompson, R. Kim Butts, Frank W. Sharbrough, Patrick J. Kelly, Dennis P. Hanson, Stephen J. Riederer, Richard L. Ehman, Nicholas J. Hangiandreou, and Gregory D. Cascino. Sensory motor cortex: correlation of presurgical mapping with functional MR imaging and invasive cortical mapping. *Radiology*, 190(1):85–92, 1994.
- [37] F. Zerrin Yetkin, Wade M. Mueller, George L. Morris, Timothy L. McAuliffe, John L. Ulmer, Robert W. Cox, David L. Daniels, and Victor M. Haughton. Functional MR activation correlated with intraoperative cortical mapping. *American Journal of Neuroradiology*, 18(7):1311–1315, 1997.
- [38] Javier Fandino, Spyros S. Kollias, Heinz G. Wieser, Anton Valavanis, and Yasuhiro Yonekawa. Intraoperative validation of functional magnetic resonance imaging and cortical reorganization patterns in patients with brain tumors involving the primary motor cortex. *Journal of neurosurgery*, 91(2):238–250, 1999.
- [39] R. Beisteiner, R. Lanzenberger, K. Novak, V. Edward, C. Windischberger, M. Erdler, R. Cunnington, A. Gartus, B. Streibl, E. Moser, and others. Improvement of presurgical patient evaluation by generation of functional magnetic resonance risk maps. *Neuroscience letters*, 290(1):13–16, 2000.

- [40] Stéphane Lehticy, Hugues Duffau, Philippe Cornu, Laurent Capelle, Bernard Pidoux, Alexandre Carpentier, Stéphanie Auliac, Stéphane Clemenceau, Jean-Pierre Sichez, Ahmed Bitar, and others. Correspondence between functional magnetic resonance imaging somatotopy and individual brain anatomy of the central region: comparison with intraoperative stimulation in patients with brain tumors. *Journal of neurosurgery*, 92(4):589–598, 2000.
- [41] F. E. Roux, K. Boulanouar, D. Ibarrola, M. Tremoulet, F. Chollet, and I. Berry. Functional MRI and intraoperative brain mapping to evaluate brain plasticity in patients with brain tumours and hemiparesis. *Journal of Neurology, Neurosurgery & Psychiatry*, 69(4):453–463, 2000.
- [42] Reinhard J. Tomczak, Arthur P. Wunderlich, Yang Wang, Veit Braun, Gregor Antoniadis, Johannes Grich, Hans-Peter Richter, and Hans-Jürgen Brambs. fMRI for preoperative neurosurgical mapping of motor cortex and language in a clinical setting. *Journal of computer assisted tomography*, 24(6):927–934, 2000.
- [43] Franck-Emmanuel Roux, Danielle Ibarrola, Michel Tremoulet, Yves Lazorthes, Patrice Henry, Jean-Christophe Sol, and Isabelle Berry. Methodological and technical issues for integrating functional magnetic resonance imaging data in a neuronavigational system. *Neurosurgery*, 49(5):1145–1157, 2001.
- [44] Chikashi Fukaya, Yoichi Katayama, Yoshihiro Murata, Kazutaka Kobayashi, Masahiko Kasai, Takamitsu Yamamoto, and Kaoru Sakatani. Localization of eloquent area utilize to functional MRI in patients with brain tumor. In *International Congress Series*, volume 1232, pages 763–767. Elsevier, 2002.
- [45] Robert Barto, R. Jech, J. Vymazal, P. Petrovicky, P. Vachata, A. Hejcl, A. Zolal, and M. Sames. Validity of primary motor area localization with fMRI versus electric cortical stimulation: A comparative study. *Acta Neurochirurgica*, 151:1071–1080, 2009.
- [46] Martina Wengenroth, M. Blatow, J. Guenther, M. Akbar, V.M. Tronnier, and C. Stippich. Diagnostic benefits of presurgical fMRI in patients with brain tumours in the primary sensorimotor cortex. *European radiology*, 21:1517–1525, 2011.
- [47] David B. FitzGerald, G. Rees Cosgrove, Steven Ronner, Hong Jiang, Brad R. Buchbinder, John W. Belliveau, Bruce R. Rosen, and Randall R. Benson. Location of language in the cortex: a comparison between functional MR imaging and electrocortical stimulation. *American Journal of Neuroradiology*, 18(8):1529–1539, 1997.
- [48] Joseph Lurito, Mark Lowe, Carl Sartorius, and Mathews Vincent. Comparison of fmri and intraoperative direct cortical stimulation in localization of receptive language areas. *Journal of Computer Assisted Tomography*, 24(1):99–105, 2000.

- [49] Nader Pouratian, Susan Y. Bookheimer, David E. Rex, Neil A. Martin, and Arthur W. Toga. Utility of preoperative functional magnetic resonance imaging for identifying language cortices in patients with vascular malformations. *Journal of neurosurgery*, 97(1):21–32, 2002.
- [50] G. J. M. Rutten, N. F. Ramsey, P. C. Van Rijen, H. J. Noordmans, and C. W. M. Van Veelen. Development of a functional magnetic resonance imaging protocol for intraoperative localization of critical temporoparietal language areas. *Annals of neurology*, 51(3):350–360, 2002.
- [51] Franck-Emmanuel Roux, Kader Boulanouar, Jean-Albert Lotterie, Mehdi Mejdoubi, James P. LeSage, and Isabelle Berry. Language functional magnetic resonance imaging in preoperative assessment of language areas: correlation with direct cortical stimulation. *Neurosurgery*, 52(6):1335–1347, 2003.
- [52] S. Larsen, R. Kikinis, I.-F. Talos, D. Weinstein, W. Wells, and A. Golby. Quantitative comparison of functional MRI and direct electrocortical stimulation for functional mapping. *The international journal of medical robotics and computer assisted surgery*, 3(3):262–270, 2007.
- [53] Nicole M. Petrovich Brennan, Stephen Whalen, Daniel de Morales Branco, James P. O’Shea, Isaiah H. Norton, and Alexandra J. Golby. Object naming is a more sensitive measure of speech localization than number counting: converging evidence from direct cortical stimulation and fMRI. *Neuroimage*, 37:S100–S108, 2007.
- [54] Alberto Bizzi, Valeria Blasi, Andrea Falini, Paolo Ferroli, Marcello Cadioli, Ugo Danesi, Domenico Aquino, Carlo Marras, Dario Caldiroli, and Giovanni Broggi. Presurgical functional MR imaging of language and motor functions: Validation with intraoperative electrocortical mapping 1. *Radiology*, 248(2):579–589, 2008.
- [55] Warren Boling, Michael Parsons, Michal Kraszpulski, Carrie Cantrell, and Aina Puce. Whole-hand sensorimotor area: cortical stimulation localization and correlation with functional magnetic resonance imaging. *Journal of Neurosurgery*, 2008.
- [56] Bob L. Hou, Michelle Bradbury, Kyung K. Peck, Nicole M. Petrovich, Philip H. Gutin, and Andrei I. Holodny. Effect of brain tumor neovasculature defined by rCBV on BOLD fMRI activation volume in the primary motor cortex. *NeuroImage*, 32(2):489–497, 2006-08.
- [57] Carlo Giussani, Frank-Emmanuel Roux, Jeffrey Ojemann, Erik Pietro Sganzerla, David Pirillo, and Costanza Papagno. Is preoperative functional magnetic resonance imaging reliable for language areas mapping in brain tumor surgery? review of language functional magnetic resonance imaging and direct cortical stimulation correlation studies. *Neurosurgery*, 66(1):113–120, 2010.

- [58] Nathan W. Churchill, Anita Oder, Herv Abdi, Fred Tam, Wayne Lee, Christopher Thomas, Jon E. Ween, Simon J. Graham, and Stephen C. Strother. Optimizing preprocessing and analysis pipelines for single-subject fMRI. i. standard temporal motion and physiological noise correction methods. *Human Brain Mapping*, 33(3):609–627, 2012-03.
- [59] Nathan W. Churchill, Grigori Yourganov, Anita Oder, Fred Tam, Simon J. Graham, and Stephen C. Strother. Optimizing preprocessing and analysis pipelines for single-subject fMRI: 2. interactions with ICA, PCA, task contrast and inter-subject heterogeneity. *PLoS ONE*, 7(2):e31147, 2012-02-27.
- [60] J.W. Evans, R.M. Todd, M.J. Taylor, and S.C. Strother. Group specific optimisation of fMRI processing steps for child and adult data. *NeuroImage*, 50(2):479–490, 2010-04.
- [61] Jing Zhang, Jon R. Anderson, Lichen Liang, Sujit K. Pulapura, Lael Gatewood, David A. Rottenberg, and Stephen C. Strother. Evaluation and optimization of fMRI single-subject processing pipelines with NPAIRS and second-level CVA. *Magnetic resonance imaging*, 27(2):264–278, 2009.
- [62] Giulia Barbati, Camillo Porcaro, Filippo Zappasodi, Paolo Maria Rossini, and Franca Tecchio. Optimization of an independent component analysis approach for artifact identification and removal in magnetoencephalographic signals. *Clinical Neurophysiology*, 115(5):1220–1232, 2004-05.
- [63] D. Mantini, R. Franciotti, G.L. Romani, and V. Pizzella. Improving MEG source localizations: An automated method for complete artifact removal based on independent component analysis. *NeuroImage*, 40(1):160–173, 2008-03-01.
- [64] Karl J. Friston, Andrew Holmes, Jean-Baptiste Poline, Cathy J. Price, and Christopher D. Frith. Detecting activations in PET and fMRI: levels of inference and power. *Neuroimage*, 4(3):223–235, 1996.
- [65] Christopher R. Genovese, Nicole A. Lazar, and Thomas Nichols. Thresholding of statistical maps in functional neuroimaging using the false discovery rate. *NeuroImage*, 15(4):870–878, 2002-04.
- [66] Thomas Nichols and Satoru Hayasaka. Controlling the familywise error rate in functional neuroimaging: a comparative review. *Statistical Methods in Medical Research*, 12(5):419–446, 2003-10-01.
- [67] Brent R. Logan and Daniel B. Rowe. An evaluation of thresholding techniques in fMRI analysis. *NeuroImage*, 22(1):95–108, 2004-05.
- [68] David G. Norris. Principles of magnetic resonance assessment of brain function. *Journal of Magnetic Resonance Imaging*, 23(6):794–807, 2006-06.

- [69] Nikos K. Logothetis. The underpinnings of the BOLD functional magnetic resonance imaging signal. *The Journal of Neuroscience*, 23(10):3963–3971, 2003.
- [70] M. Hamalainen, R. Hari, R. Ilmoniemi, J. Knuutila, and O. Lounasmaa. Magnetoencephalography - theory, instrumentation, and applications to noninvasive studies of the working human brain. *Review of Modern Physics*, 65(2):413–505, 1993.
- [71] R.N. Henson, J. Mattout, C. Phillips, and K.J. Friston. Selecting forward models for MEG source-reconstruction using model-evidence. 46(1):168–176.
- [72] Olaf Steinstrter, Stephanie Sillekens, Markus Junghoefer, Martin Burger, and Carsten H. Wolters. Sensitivity of beamformer source analysis to deficiencies in forward modeling. 31(12):1907–1927.
- [73] Barry D. Van Veen, Wim Van Drongelen, Moshe Yuchtman, and Akifumi Suzuki. Localization of brain electrical activity via linearly constrained minimum variance spatial filtering. *Biomedical Engineering, IEEE Transactions on*, 44(9):867–880, 1997.
- [74] Olaf Hauk. Keep it simple: a case for using classical minimum norm estimation in the analysis of EEG and MEG data. 21(4):1612–1621.
- [75] K. Uutela, M. Hamalainen, and E. Somersalo. Visualization of magnetoencephalographic data using minimum current estimates. 10:173–180.
- [76] Anders M. Dale, Arthur K. Liu, Bruce R. Fischl, Randy L. Buckner, John W. Belliveau, Jeffrey D. Lewine, and Eric Halgren. Dynamic statistical parametric mapping: combining fMRI and MEG for high-resolution imaging of cortical activity. 26(1):55–67.
- [77] Sarang S. Dalal, Johanna M. Zumer, Adrian G. Guggisberg, Michael Trumpis, Daniel D. E. Wong, Kensuke Sekihara, and Srikantan S. Nagarajan. MEG/EEG source reconstruction, statistical evaluation, and visualization with NUTMEG. 2011:1–17.
- [78] Fa-Hsuan Lin, Thomas Witzel, Seppo P. Ahlfors, Steven M. Stufflebeam, John W. Belliveau, and Matti S. Hmlinen. Assessing and improving the spatial accuracy in MEG source localization by depth-weighted minimum-norm estimates. 31(1):160–171.
- [79] Yoav Benjamini and Yosef Hochberg. On the adaptive control of the false discovery rate in multiple testing with independent statistics. 25(1):60.
- [80] Krzysztof J. Gorgolewski, Amos J. Storkey, Mark E. Bastin, and Cyril R. Pernet. Adaptive thresholding for reliable topological inference in single subject fMRI analysis. *Frontiers in Human Neuroscience*, 6, 2012.

- [81] Dimitrios Pantazis, Thomas E. Nichols, Sylvain Baillet, and Richard M. Leahy. Spatiotemporal localization of significant activation in MEG using permutation tests. In *Information Processing in Medical Imaging*, pages 512–523. Springer, 2003.
- [82] Garreth Prendergast, Sam R. Johnson, Mark Hymers, Will Woods, and Gary G.R. Green. Non-parametric statistical thresholding of baseline free MEG beamformer images. *NeuroImage*, 54(2):906–918, 2011-01.
- [83] Douglas C. Noll, Christopher R. Genovese, Leigh E. Nystrom, Alberto L. Vazquez, Steven D. Forman, William F. Eddy, and Jonathan D. Cohen. Estimating test-retest reliability in functional MR imaging II: Application to motor and cognitive activation studies. *Magnetic Resonance in Medicine*, 38(3):508–517, 1997.
- [84] Pawel Skudlarski, R. Todd Constable, and John C. Gore. ROC analysis of statistical methods used in functional MRI: individual subjects. *Neuroimage*, 9(3):311–329, 1999.
- [85] T.H. Le and X. Hu. Methods for assessing accuracy and reliability in functional MRI. *NMR in Biomedicine*, 10(160), 1997.
- [86] Karl J. Friston, Andrew P. Holmes, Keith J. Worsley, J.-P. Poline, Chris D. Frith, and Richard SJ Frackowiak. Statistical parametric maps in functional imaging: a general linear approach. *Human brain mapping*, 2(4):189–210, 1994.
- [87] S. Suresh Anand and Vitali Zagorodnov. Retrospective cluster size thresholding for MRF-based detection of activated regions in fMRI. In *Biomedical and Pharmaceutical Engineering, 2006. ICBPE 2006. International Conference on*, pages 44–47. IEEE, 2006.
- [88] Christopher R. Genovese, Douglas C. Noll, and William F. Eddy. Estimating test-retest reliability in functional MR imaging i: Statistical methodology. *Magnetic Resonance in Medicine*, 38(3):497–507, 1997.
- [89] Serge ARB Rombouts, Frederik Barkhof, Frank GC Hoogenraad, Michiel Sprenger, and Philip Scheltens. Within-subject reproducibility of visual activation patterns with functional magnetic resonance imaging using multislice echo planar imaging. *Magnetic resonance imaging*, 16(2):105–113, 1998.
- [90] Keith J. Duncan, Chotiga Pattamadilok, Iris Knierim, and Joseph T. Devlin. Consistency and variability in functional localisers. *Neuroimage*, 46(4):1018–1026, 2009.
- [91] Michelle Liou, Hong-Ren Su, Alexander N. Savostyanov, Juin-Der Lee, John AD Aston, Cheng-Hung Chuang, and Philip E. Cheng. Beyond p-values: Averaged and reproducible evidence in fMRI experiments. *Psychophysiology*, 46(2):367–378, 2009.

- [92] Craig M. Bennett and Michael B. Miller. Issue: The year in cognitive neuroscience. *The Year in Cognitive Neuroscience*, 1124:133, 2010.
- [93] Gordon E. Sarty and Ron Borowsky. Functional MRI activation maps from empirically defined curve fitting. *Concepts in Magnetic Resonance Part B: Magnetic Resonance Engineering*, 24B(1):46–55, 2005-02.
- [94] Stephen C. Strother, N. Lange, J. R. Anderson, K. A. Schaper, K. Rehm, Lars Kai Hansen, and D. A. Rottenberg. Activation pattern reproducibility: Measuring the effects of group size and data analysis models. *Human brain mapping*, 5(4):312–316, 1997.
- [95] Carola Tegeler, Stephen C. Strother, Jon R. Anderson, and Seong-Gi Kim. Reproducibility of BOLD-based functional MRI obtained at 4 t. *Human Brain Mapping*, 7(4):267–283, 1999.
- [96] G. Fernandez, K. Specht, S. Weis, I. Tendolkar, M. Reuber, J. Fell, P. Klaver, J. Ruhlmann, J. Reul, and C. E. Elger. Intrasubject reproducibility of presurgical language lateralization and mapping using fMRI. *Neurology*, 60(6):969–975, 2003.
- [97] Karsten Specht, Klaus Willmes, N. Jon Shah, and Lutz Jucke. Assessment of reliability in functional imaging studies. *Journal of Magnetic Resonance Imaging*, 17(4):463–471, 2003.
- [98] M. Raemaekers, M. Vink, B. Zandbelt, R. J. A. Van Wezel, R. S. Kahn, and N. F. Ramsey. Test-retest reliability of fMRI activation during prosaccades and antisaccades. *Neuroimage*, 36(3):532–542, 2007.
- [99] Teresa Jacobson Kimberley, Gauri Khandekar, and Michael Borich. fMRI reliability in subjects with stroke. *Experimental brain research*, 186(1):183–190, 2008.
- [100] Teresa Jacobson Kimberley, Dana D. Birkholz, Renee A. Hancock, Sarah M. VonBank, and Teresa N. Werth. Reliability of fMRI during a continuous motor task: assessment of analysis techniques. *Journal of Neuroimaging*, 18(1):18–27, 2008.
- [101] Alejandro Caceres, Deanna L. Hall, Fernando O. Zelaya, Steven CR Williams, and Mitul A. Mehta. Measuring fMRI reliability with the intra-class correlation coefficient. *Neuroimage*, 45(3):758–768, 2009.
- [102] Michael M. Plichta, Adam J. Schwarz, Oliver Grimm, Katrin Morgen, Daniela Mier, Leila Haddad, Antje Gerdes, Carina Sauer, Heike Tost, Christine Esslinger, and others. Test-retest reliability of evoked BOLD signals from a cognitive-emotive fMRI test battery. *Neuroimage*, 60(3):1746–1758, 2012.

- [103] S. A. Rombouts, Frederik Barkhof, F. G. Hoogenraad, Michiel Sprenger, Jaap Valk, and Philip Scheltens. Test-retest analysis with functional MR of the activated area in the human visual cortex. *American journal of neuroradiology*, 18(7):1317–1322, 1997.
- [104] E. Elinor Chen and Steven L. Small. Testretest reliability in fMRI of language: group and task effects. *Brain and language*, 102(2):176–185, 2007.
- [105] Joseph A. Maldjian, Paul J. Laurienti, Lance Driskill, and Jonathan H. Burdette. Multiple reproducibility indices for evaluation of cognitive functional MR imaging paradigms. *American journal of neuroradiology*, 23(6):1030–1037, 2002.
- [106] Greg S. Harrington, Sarah Tomaszewski Farias, Michael H. Buonocore, and Andrew P. Yonelinas. The intersubject and intrasubject reproducibility of fMRI activation during three encoding tasks: implications for clinical applications. *Neuroradiology*, 48(7):495–505, 2006.
- [107] Peter Mannfolk, Markus Nilsson, Henrik Hansson, Freddy Stahlberg, Peter Fransson, Andreas Weibull, Jonas Svensson, Ronnie Wirestam, and Johan Olsson. Can resting-state functional MRI serve as a complement to task-based mapping of sensorimotor function? a test-retest reliability study in healthy volunteers. *Journal of Magnetic Resonance Imaging*, 34:511–517, 2011.
- [108] Ranjan Maitra, Steven R. Roys, and Rao P. Gullapalli. Test-retest reliability estimation of functional MRI data. *Magnetic Resonance in Medicine*, 48(1):62–70, 2002.
- [109] John H. Brannen, Behnam Badie, Chad H. Moritz, Michelle Quigley, M. Elizabeth Meyerand, and Victor M. Houghton. Reliability of functional MR imaging with word-generation tasks for mapping broca’s area. *American Journal of Neuroradiology*, 22(9):1711–1718, 2001.
- [110] Rose Bosnell, C. Wegner, Z. T. Kincses, T. Korteweg, F. Agosta, Olga Ciccarelli, Nicola De Stefano, A. Gass, J. Hirsch, Heidi Johansen-Berg, and others. Reproducibility of fMRI in the clinical setting: implications for trial designs. *Neuroimage*, 42(2):603–610, 2008.
- [111] G. Fesl, B. Braun, S. Rau, M. Wiesmann, M. Ruge, P. Bruhns, J. Linn, T. Stephan, J. Ilmberger, J.-C. Tonn, and others. Is the center of mass (COM) a reliable parameter for the localization of brain function in fMRI? *European radiology*, 18(5):1031–1037, 2008.

- [112] Viktoria-Eleni Gountouna, Dominic E. Job, Andrew M. McIntosh, T. William J. Moorhead, G. Katherine L. Lymer, Heather C. Whalley, Jeremy Hall, Gordon D. Waiter, David Brennan, David J. McGonigle, and others. Functional magnetic resonance imaging (fMRI) reproducibility and variance components across visits and scanning sites with a finger tapping task. *Neuroimage*, 49(1):552–560, 2010.
- [113] Ranjan Maitra. A re-defined and generalized percent-overlap-of-activation measure for studies of fMRI reproducibility and its use in identifying outlier activation maps. *NeuroImage*, 50:124–135, 2010.
- [114] Javier Gonzalez-Castillo and Thomas M. Talavage. Reproducibility of fMRI activations associated with auditory sentence comprehension. *Neuroimage*, 54(3):2138–2155, 2011.
- [115] Rao P. Gullapalli, Ranjan Maitra, Steve Roys, Gerald Smith, Gad Alon, and Joel Greenspan. Reliability estimation of grouped functional imaging data using penalized maximum likelihood. *Magnetic resonance in medicine*, 53(5):1126–1134, 2005.
- [116] P Jaccard. Etude comparative de la distribution florale dans une portion des alpes et des jura. *Bulletin de la Socit Vaudoise des Sciences Naturelles*, 37:547–579, 1901.
- [117] Ranjan Maitra. Assessing certainty of activation or inactivation in test-retest fMRI studies. *Neuroimage*, 47(1):88–97, 2009.
- [118] R.C. Oldfield. The assessment and analysis of handedness: The edinburgh inventory. *Neuropsychologia*, 9:97–113, 1971.
- [119] Robert W. Cox. AFNI: software for analysis and visualization of functional magnetic resonance neuroimages. *Computers and Biomedical research*, 29(3):162–173, 1996.
- [120] Bertrand Thirion, Philippe Pinel, Sbastien Mriaux, Alexis Roche, Stanislas Dehaene, and Jean-Baptiste Poline. Analysis of a large fMRI cohort: Statistical and methodological issues for group analyses. *Neuroimage*, 35(1):105–120, 2007.
- [121] Mohamed L. Seghier, Francois Lazeyras, Alan J. Pegna, Jean-Marie Annoni, Ivan Zimine, Eugne Mayer, Christoph M. Michel, and Asaid Khateb. Variability of fMRI activation during a phonological and semantic language task in healthy subjects. *Human Brain Mapping*, 23(3):140–155, 2004-11.
- [122] Ryan CN D’arcy, Timothy Bardouille, Aaron J. Newman, Sean R. McWhinney, Drew DeBay, R. Mark Sadler, David B. Clarke, and Michael J. Esser. Spatial MEG laterality maps for language: Clinical applications in epilepsy. *Human brain mapping*, 34(8):1749–1760, 2013.

- [123] I.M. Ruff, N.M. Petrovich Brennan, K.K. Peck, B.L. Hou, V. Tabar, C.W. Brennan, and A.I. Holodny. Assessment of the language laterality index in patients with brain tumor using functional MR imaging: Effects of thresholding, task selection, and prior surgery. *American Journal of Neuroradiology*, 29(3):528–535, 2008-03-01.
- [124] David F. Abbott, Anthony B. Waites, Leasha M. Lillywhite, and Graeme D. Jackson. fMRI assessment of language lateralization: An objective approach. *NeuroImage*, 50(4):1446–1455, 2010-05.
- [125] Kayako Matsuo, Shen-Hsing Annabel Chen, and Wen-Yih Isaac Tseng. AveLI: A robust lateralization index in functional magnetic resonance imaging using unbiased threshold-free computation. *Journal of Neuroscience Methods*, 205(1):119–129, 2012-03.
- [126] Maria Strandberg, Christina Elfgren, Peter Mannfolk, Johan Olsrud, Lars Strandberg, Danielle van Westen, Elna-Marie Larsson, Ia Rorsman, and Kristina Klln. fMRI memory assessment in healthy subjects: a new approach to view lateralization data at an individual level. *Brain Imaging and Behavior*, 5(1):1–11, 2011-03.
- [127] Babak Afshin-Pour, Gholam-Ali Hossein-Zadeh, Stephen C. Strother, and Hamid Soltanian-Zadeh. Enhancing reproducibility of fMRI statistical maps using generalized canonical correlation analysis in NPAIRS framework. *NeuroImage*, 60(4):1970–1981, 2012-05.
- [128] Isabelle Loubinoux, Christophe Carel, Flamine Alary, Kader Boulanouar, Grard Viillard, Claude Manelfe, Olivier Rascol, Pierre Celsis, and Francois Chollet. Within-session and between-session reproducibility of cerebral sensorimotor activation: A test-retest effect evidenced with functional magnetic resonance imaging. *Journal of Cerebral Blood Flow & Metabolism*, 21:592–607, 2001.
- [129] Steven E. Petersen, Hanneke Van Mier, Julie A. Fiez, and Marcus E. Raichle. The effects of practice on the functional anatomy of task performance. *Proceedings of the National Academy of Sciences*, 95(3):853–860, 1998.
- [130] Hubertus Lohmann, Michael Deppe, Andreas Jansen, Wolfram Schwindt, and Stefan Knecht. Task repetition can affect functional magnetic resonance imaging-based measures of language lateralization and lead to pseudoincreases in bilaterality. *Journal of Cerebral Blood Flow & Metabolism*, 24(2):179–187, 2004.
- [131] Michelle Liou, Hong-Ren Su, Juin-Der Lee, Philip E. Cheng, Chien-Chih Huang, and Chih-Hsin Tsai. Bridging functional MR images and scientific inference: reproducibility maps. *Journal of Cognitive Neuroscience*, 15(7):935–945, 2003.

- [132] Michelle Liou, Hong-Ren Su, Juin-Der Lee, John AD Aston, Arthur C. Tsai, and Philip E. Cheng. A method for generating reproducible evidence in fMRI studies. *NeuroImage*, 29(2):383–395, 2006.
- [133] Juha Huttunen, Soile Komssi, and Leena Lauronen. Spatial dynamics of population activities at s1 after median and ulnar nerve stimulation revisited: An MEG study. *NeuroImage*, 32(3):1024–1031, 2006-09.
- [134] M. Oishi, M. Fukuda, S. Kameyama, T. Kawaguchi, H. Masuda, and R. Tanaka. Magnetoencephalographic representation of the sensorimotor hand area in cases of intracerebral tumour. *Journal of Neurology, Neurosurgery & Psychiatry*, 74(12):1649–1654, 2003.
- [135] Yung-Yang Lin, Wei-Ta Chen, Kwong-Kum Liao, Tzu-Chen Yeh, Zin-An Wu, Low-Tone Ho, and Liang-Shong Lee. Differential generators for n20m and p35m responses to median nerve stimulation. *NeuroImage*, 25(4):1090–1099, 2005-05.
- [136] Ajay Niranjana, Erika J.C. Laing, Fahad J. Laghari, R. Mark Richardson, and L. Dade Lunsford. Preoperative magnetoencephalographic sensory cortex mapping. *Stereotactic and Functional Neurosurgery*, 91(5):314–322, 2013.
- [137] J Gross, L Timmermann, J Kujala, R Salmelin, and A Schnitzler. Properties of MEG tomographic maps obtained with spatial filtering. 19(4):1329–1336.
- [138] T. Bardouille and B. Ross. MEG imaging of sensorimotor areas using inter-trial coherence in vibrotactile steady-state responses. *NeuroImage*, 42(1):323–331, 2008-08.
- [139] A. Kanno, N. Nakasato, Y. Nagamine, and T. Tominaga. Non-transcallosal ipsilateral area 3b responses to median nerve stimulus. *Journal of Clinical Neuroscience*, 11(8):868–871, 2004-11.
- [140] Douglas Cheyne, Andreea C. Bostan, William Gaetz, and Elizabeth W. Pang. Event-related beamforming: A robust method for presurgical functional mapping using MEG. *Clinical Neurophysiology*, 118(8):1691–1704, 2007-08.
- [141] M. Tynan R. Stevens, Ryan CN D’Arcy, Gerhard Stroink, David B. Clarke, and Steven D. Beyea. Thresholds in fMRI studies: Reliable for single subjects? *Journal of neuroscience methods*, 219(2):312–323, 2013.
- [142] S Taulu and J Simola. Spatiotemporal signal space separation method for rejecting nearby interference in MEG measurements. *Physics in Medicine and Biology*, 51(7):1759–1768, 2006-04-07.

- [143] Gnther Grabner, AndrewL. Janke, MarcM. Budge, David Smith, Jens Pruessner, and D.Louis Collins. Symmetric atlasng and model based segmentation: An application to the hippocampus in older adults. In Rasmus Larsen, Mads Nielsen, and Jon Sporring, editors, *Medical Image Computing and Computer-Assisted Intervention MICCAI 2006*, volume 4191 of *Lecture Notes in Computer Science*, pages 58–66. Springer Berlin Heidelberg, 2006.
- [144] Matthew T. Sutherland and Akaysha C. Tang. Reliable detection of bilateral activation in human primary somatosensory cortex by unilateral median nerve stimulation. 33(4):1042–1054.
- [145] Susan M. Bowyer, Toya Fleming, Margaret L. Greenwald, John E. Moran, Karen M. Mason, Barbara J. Weiland, Brien J. Smith, Gregory L. Barkley, and Norman Tepley. Magnetoencephalographic localization of the basal temporal language area. *Epilepsy & Behavior*, 6(2):229–234, 2005-03.
- [146] N. Tanaka, H. Liu, C. Reinsberger, J. R. Madsen, B. F. Bourgeois, B. A. Dworetzky, M. S. Hamalainen, and S. M. Stufflebeam. Language lateralization represented by spatiotemporal mapping of magnetoencephalography. *American Journal of Neuroradiology*, 34(3):558–563, 2013-03-01.
- [147] Kensuke Sekihara, Maneesh Sahani, and Srikantan S. Nagarajan. Localization bias and spatial resolution of adaptive and non-adaptive spatial filters for MEG source reconstruction. *NeuroImage*, 25(4):1056–1067, 2005-05.
- [148] Massimo Fornasier and Francesca Pitolli. Adaptive iterative thresholding algorithms for magnetoencephalography (MEG). *Journal of Computational and Applied Mathematics*, 221(2):386–395, 2008-11.
- [149] Hooman Alikhanian, J. Douglas Crawford, Joseph F. X. DeSouza, Douglas O. Cheyne, and Gunnar Blohm. Adaptive cluster analysis approach for functional localization using magnetoencephalography. *Frontiers in Neuroscience*, 7, 2013.
- [150] C. Amblard, E. Lapalme, and J.-M. Lina. Biomagnetic source detection by maximum entropy and graphical models. 51(3):427–442.
- [151] J. J. Pillai. The evolution of clinical functional imaging during the past 2 decades and its current impact on neurosurgical planning. *American Journal of Neuroradiology*, 31(2):219–225, 2010.
- [152] Christoph Stippich, Maria Blatow, and Karsten Krakow. Presurgical functional MRI in patients with brain tumors. In Christoph Stippich, editor, *Clinical functional MRI: Presurgical functional neuroimaging*, pages 88–126. Springer-Verlag, 2007.

- [153] Kuan H. Kho, Geert-Jan M. Rutten, Frans SS Leijten, Arjen van der Schaaf, Peter C. van Rijen, and Nick F. Ramsey. Working memory deficits after resection of the dorsolateral prefrontal cortex predicted by functional magnetic resonance imaging and electrocortical stimulation mapping: Case report. *Journal of Neurosurgery: Pediatrics*, 106(6):501–505, 2007.
- [154] G.J.M. Rutten, Nick F. Ramsey, P.C. van Rijen, and C.W.M. van Veelen. Reproducibility of fMRI-determined language lateralization in individual subjects. *Brain and language*, 80:421–437, 2002.
- [155] David J. McGonigle. Test-retest reliability in fMRI: or how i learned to stop worrying and love the variability. *NeuroImage*, 62(2):1116–1120, 2012.
- [156] S. Gonzalez-Ortiz, L. Oleaga, T. Pujol, S. Medrano, J. Rumia, L. Caral, T. Boget, J. Capellades, and N. Bargallo. Simple fMRI postprocessing suffices for normal clinical practice. *American Journal of Neuroradiology*, 34(6):1188–1193, 2013-06-01.
- [157] Stephen C. Strother, Jon Anderson, Lars Kai Hansen, Ulrik Kjems, Rafal Kustra, John Sidtis, Sally Frutiger, Suraj Muley, Stephen LaConte, and David Rottenberg. The quantitative evaluation of functional neuroimaging experiments: the NPAIRS data analysis framework. *NeuroImage*, 15(4):747–771, 2002.
- [158] Stephen La Conte, Jon Anderson, Suraj Muley, James Ashe, Sally Frutiger, Kelly Rehm, Lars Kai Hansen, Essa Yacoub, Xiaoping Hu, David Rottenberg, and Stephen Strother. The evaluation of preprocessing choices in single-subject BOLD fMRI using NPAIRS performance metrics. *NeuroImage*, 18:10–27, 2003.
- [159] Janusch Blautzik, Daniel Keeser, Albert Berman, Marco Paolini, Valerie Kirsch, Sophia Mueller, Ute Coates, Maximilian Reiser, Stefan J. Teipel, and Thomas Meindl. Long-term test-retest reliability of resting-state networks in healthy elderly subjects and patients with amnesic mild cognitive impairment. *Journal of Alzheimer’s Disease*, 34(3):741–754, 2013.
- [160] James T. Voyvodic, Jeffrey R. Petrella, and Allan H. Friedman. fMRI activation mapping as a percentage of local excitation: Consistent presurgical motor maps without threshold adjustment. *Journal of Magnetic Resonance Imaging*, 29(4):751–759, 2009-04.
- [161] Tynan Stevens, Ryan D’Arcy, Steven Beyea, and David Clarke. Retrospective registration for improved localization of cortical stimulation on mr images. In *International Society for Magnetic Resonance in Medicine*, 2012.
- [162] PJ Besl and ND McKay. A method for registration of 3-d shapes. *IEEE Transactions on Pattern Analysis and Machine Intelligence*, 14(2):239–256, 1992.

- [163] Dara S. Manoach, Elkan F. Halpern, Todd S. Kramer, Yuchiao Chang, Donald C. Goff, Scott L. Rauch, David N. Kennedy, and Randy L. Gollub. Test-retest reliability of a functional MRI working memory paradigm in normal and schizophrenic subjects. *American Journal of Psychiatry*, 158(6):955–958, 2001.
- [164] Olivier Maza, Bernard Mazoyer, Pierre-Yves Herv, Annick Razafimandimby, Sonia Dollfus, and Nathalie Tzourio-Mazoyer. Reproducibility of fMRI activations during a story listening task in patients with schizophrenia. *Schizophrenia research*, 128(1):98–101, 2011.
- [165] Kenneth P. Eaton, Jerzy P. Szaflarski, Mekibib Altaye, Angel L. Ball, Brett M. Kissela, Christi Banks, and Scott K. Holland. Reliability of fMRI for studies of language in post-stroke aphasia subjects. *Neuroimage*, 41(2):311–322, 2008.
- [166] Giannantonio Spena, Antonella Nava, Fabrizio Cassini, Antonio Pepoli, Marcella Bruno, Federico DAgata, Franco Cauda, Katiuscia Sacco, Sergio Duca, Laura Barletta, and Pietro Versari. Preoperative and intraoperative brain mapping for the resection of eloquent-area tumors. a prospective analysis of methodology, correlation, and usefulness based on clinical outcomes. 152(11):1835–1846.
- [167] Peter Grummich, Christopher Nimsky, Elisabeth Pauli, Michael Buchfelder, and Oliver Ganslandt. Combining fMRI and MEG increases the reliability of presurgical language localization: A clinical study on the difference between and congruence of both modalities. *NeuroImage*, 32(4):1793–1803, 2006-10.
- [168] Helmut Kober, Christopher Nimsky, Martin Mller, Peter Hastreiter, Rudolf Fahlbusch, and Oliver Ganslandt. Correlation of sensorimotor activation with functional magnetic resonance imaging and magnetoencephalography in presurgical functional imaging: A spatial analysis. *NeuroImage*, 14(5):1214–1228, 2001-11.
- [169] K Singh. Task-related changes in cortical synchronization are spatially coincident with the hemodynamic response. *NeuroImage*, 16(1):103–114, 2002-05.
- [170] John Sanders, Jeffrey D. Lewine, and William Orrison. Comparison of primary motor cortex localization using functional magnetic resonance imaging and magnetoencephalography. *Human Brain Mapping*, 4:47–57, 1996.
- [171] Hiroaki Shimizu, Nobukazu Nakasato, Kazuo Mizoi, and Takashi Yoshimoto. Localizing the central sulcus by functional magnetic resonance imaging and magnetoencephalography. *Clinical Neurology and Neurosurgery*, 99:235–238, 1997.
- [172] Christoph Stippich, Peter Freitag, Jan Kassubek, Helmut Kober, Klaus Scheffler, Rudiger Hopfengartner, Deniz Bilecen, Ernst Radu, and Jurgen Vieth. Motor, somatosensory and auditory cortex localization by fMRI and MEG. *NeuroReport*, 9:1953–1957, 1998.

- [173] Timothy PL Roberts, Elizabeth A. Disbrow, Heidi C. Roberts, and Howard A. Rowley. Quantification and reproducibility of tracking cortical extent of activation by use of functional MR imaging and magnetoencephalography. *American journal of neuroradiology*, 21(8):1377–1387, 2000.
- [174] F. Moradi, L.C. Liu, K. Cheng, R.A. Waggoner, K. Tanaka, and A.A. Ioannides. Consistent and precise localization of brain activity in human primary visual cortex by MEG and fMRI. *NeuroImage*, 18(3):595–609, 2003-03.
- [175] Pasi I Tuunanen, Martin Kavec, Veikko Jousmki, Jussi-Pekka Usenius, Riitta Hari, Riitta Salmelin, and Risto A Kauppinen. Comparison of BOLD fMRI and MEG characteristics to vibrotactile stimulation. *NeuroImage*, 19(4):1778–1786, 2003-08.
- [176] M. Brunetti, P. Belardinelli, M. Caulo, C. Del Gratta, S. Della Penna, A. Ferretti, G. Lucci, A. Moretti, V. Pizzella, A. Tartaro, K. Torquati, M. Olivetti Belardinelli, and G.L. Romani. Human brain activation during passive listening to sounds from different locations: An fMRI and MEG study. *Human Brain Mapping*, 26(4):251–261, 2005-12.
- [177] Rebecca L. Billingsley-Marshall, Trustin Clear, W. Einar Mencl, Panagiotis G. Simos, Paul R. Swank, Disheng Men, Shirin Sarkari, Eduardo M. Castillo, and Andrew C. Papanicolaou. A comparison of functional MRI and magnetoencephalography for receptive language mapping. *Journal of Neuroscience Methods*, 161(2):306–313, 2007-04.
- [178] Kyoussuke Kamada, Yutaka Sawamura, Fumiya Takeuchi, Shinya Kuriki, Kensuke Kawai, Akio Morita, and Tomoki Todo. Expressive and receptive language areas determined by a non-invasive reliable method using functional magnetic resonance imaging and magnetoencephalography. *Neurosurgery*, 60(2):296–306, 2007-02.
- [179] Mia Liljestrm, Annika Hultn, Lauri Parkkonen, and Riitta Salmelin. Comparing MEG and fMRI views to naming actions and objects. *Human Brain Mapping*, 30(6):1845–1856, 2009-06.
- [180] Elizabeth W. Pang, Frank Wang, Marion Malone, Darren S. Kadis, and Elizabeth J. Donner. Localization of broca’s area using verb generation tasks in the MEG: Validation against fMRI. *Neuroscience Letters*, 490(3):215–219, 2011-03.
- [181] Yingying Wang, Scott K. Holland, and Jennifer Vannest. Concordance of MEG and fMRI patterns in adolescents during verb generation. *Brain Research*, 1447:79–90, 2012-04.
- [182] Silke Klamer, Adham Elshahabi, Holger Lerche, Christoph Braun, Michael Erb, Klaus Scheffler, and Niels K. Focke. Differences between MEG and high-density EEG source localizations using a distributed source model in comparison to fMRI. *Brain Topography*, 28(1):87–94, 2015-01.

- [183] Stephen C. Strother. Evaluating fMRI preprocessing pipelines. *Engineering in Medicine and Biology Magazine, IEEE*, 25(2):27–41, 2006.
- [184] Joshua I. Breier, Panagiotis G. Simos, George Zouridakis, and Andrew C. Papanicolaou. Lateralization of activity associated with language function using magnetoencephalography: a reliability study. *Journal of Clinical Neurophysiology*, 17(5):503–510, 2000.
- [185] Krzysztof J. Gorgolewski, Amos J. Storkey, Mark E. Bastin, Ian Whittle, and Cyril Pernet. Single subject fMRI test-retest reliability metrics and confounding factors. *Neuroimage*, 69:231–243, 2013.
- [186] Dongwook Lee, Stephen M. Sawrie, Panagiotis G. Simos, Jeff Killen, and Robert C. Knowlton. Reliability of language mapping with magnetic source imaging in epilepsy surgery candidates. *Epilepsy & Behavior*, 8(4):742–749, 2006-06.
- [187] Panagiotis G. Simos, Shirin Sarkari, Eduardo M. Castillo, Rebecca L. Billingsley-Marshall, Ekaterina Pataraiia, Trustin Clear, and Andrew C. Papanicolaou. Reproducibility of measures of neurophysiological activity in wernicke’s area: A magnetic source imaging study. *Clinical Neurophysiology*, 116(10):2381–2391, 2005-10.
- [188] Rebecca L. Billingsley-Marshall, Panagiotis G. Simos, and Andrew C. Papanicolaou. Reliability and validity of functional neuroimaging techniques for identifying language-critical areas in children and adults. *Developmental neuropsychology*, 26(2):541–563, 2004.
- [189] Bruce Fischl, David H. Salat, Evelina Busa, Marilyn Albert, Megan Dieterich, Christian Haselgrove, Andre van der Kouwe, Ron Killiany, David Kennedy, Shuna Klaveness, Albert Montillo, Nikos Makris, Bruce Rosen, and Anders M. Dale. Whole brain segmentation: automated labeling of neuroanatomical structures in the human brain. *Neuron*, 33(3):341–355, 2002-01-31.
- [190] Mark Jenkinson, Christian F. Beckmann, Timothy E. J. Behrens, Mark W. Woolrich, and Stephen M. Smith. FSL. *NeuroImage*, 62(2):782–790, 2012-08-15.
- [191] Elizabeth W. Pang, William Gaetz, James M. Drake, Samuel Strantzas, Matthew J. MacDonald, Hiroshi Otsubo, and O. Carter Snead. Patient with postcentral gyrectomy demonstrates reliable localization of hand motor area using magnetoencephalography. *Pediatric Neurosurgery*, 45(4):311–316, 2009.
- [192] Andrei I. Holodny, Michael Schulder, Wen Ching Liu, Joseph A. Maldjian, and Andrew J. Kalnin. Decreased BOLD functional MR activation of the motor and sensory cortices adjacent to a glioblastoma multiforme: implications for image-guided neurosurgery. *American journal of neuroradiology*, 20(4):609–612, 1999.

- [193] Axel Schreiber, Ulrich Hubbe, Sargon Ziyeh, and Jrgen Hennig. The influence of gliomas and nonglial space-occupying lesions on blood-oxygen-leveldependent contrast enhancement. *American journal of neuroradiology*, 21(6):1055–1063, 2000.